NTNU – Trondheim
Norwegian University of
Science and Technology

Impact on Duplex Steel Pipes with Precipitated Sigma-phase

Modeling a Full-scale Impact Test on Pipe Fittings

Christian Bergstrøm Hillestad
Andreas Bratlie

Civil and Environmental Engineering (2 year)
Submission date: June 2012
Supervisor: Tore Børvik, KT
Co-supervisor: Odd Sture Hopperstad, KT

Norwegian University of Science and Technology
Department of Structural Engineering

Department of Structural Engineering
Faculty of Engineering Science and Technology
NTNU - Norwegian University of Science and Technology

ACCESSIBILITY:
OPEN

MASTER THESIS 2012

SUBJECT AREA:	DATE:	NO. OF PAGES:
STRUCTURAL IMPACT	11.06.12	153 + Cover

TITLE:

Impact on Duplex Steel Pipes with Precipitated Sigma-phase
Støt på duplex stålrør med utfelt sigmafase

BY:

Andreas Bratlie
Christian Bergstrøm Hillestad

SUMMARY:

Duplex stainless steel (DSS) is a common material in offshore pipe fittings. A manufacturing defect has altered the behavior of the components through an erroneous heat treatment, which has led to precipitation of σ-phase. A report showing a strong correlation between precipitated σ-phase and the reduction in impact toughness, initiated a great interest in the offshore industry for further studies of the effect of precipitated σ-phase in DSS pipe fittings.

In this thesis a numerical approach to simulate the behavior of duplex stainless steel with precipitated σ-phase has been performed. The simulations have been done using the Gurson material model, which is implemented in the user defined material model in the SIMLab Metal Model. In addition the material model has been combined with a brittle fracture criterion.

The results deviate from the observations done in the laboratory. The reasons for the deviations were found to be quite complex, but effects from mesh sensitivity and incorrect material optimization was found.

The influence of the Gurson model is limited for the specimens acting in a brittle manner. It is therefore considered unnecessary to apply this material model for these problems.

RESPONSIBLE TEACHER: Tore Børvik

SUPERVISORS: Tore Børvik and Odd Sture Hopperstad

CARRIED OUT AT: SIMLab, Department of Structural Engineering, Faculty of Engineering Science and Technology, Norwegian University of Science and Technology

Department of Structural Engineering

FACULTY OF ENGINEERING SCIENCE AND TECHNOLOGY
NTNU – Norwegian University of Science and Technology

Master Thesis 2012

for

Andreas Bratlie and Christian Hillestad

Impact on Duplex Steel Pipes with Precipitated Sigma-phase

Støt på duplex stålrør med utfelt sigmafase

As a result of a manufacturing defect altering the behavior of the components through an erroneous heat treatment, precipitation of σ-phase has occurred. The problem is that precipitated sigma-phase reduces the ductility and corrosion resistance in duplex steel, which is non favorable in accidental analysis offshore. On the basis of material tests, component tests and numerical simulations, this assignment will investigate in which degree sigma affects the impact toughness in pipe fittings. It is especially important to study whether or when fracture occurs, in fittings like these, and how this can be modeled.

The assignment may include the following activities:

1. Literature study: Metallurgy of stainless steel; impact on pipes, material and failure models.
2. Material test: It's already done a number of material tests on duplex steel with and without sigma. These material tests will be studied and on this basis, the relevant material- and fracture models are calibrated.
3. Component test: It is previously carried out both static- and dynamic impact tests on pipe fittings with and without sigma. The results from these tests will be summarized and discussed.
4. Numerical simulations: Both the material- and component tests will be modeled in LS-DYNA. Simulations should be performed and results shall be validated against experimental data. It is particularly important to assess the capacity in terms of fracture in pipe fittings.
5. Reporting.

The paper is organized in accordance with the current guidelines.

Supervisors: Tore Børvik og Odd Sture Hopperstad

The response shall be submitted to the Department of Structural Engineering by June 11. 2012.

NTNU, January 16. 2012

Tore Børvik
Responsible teacher

Preface

This thesis is written in corporation with the Structural Impact Laboratory (SIMLab) at the Department of Structural Engineering at Norwegian University of Science and Technology.

The essence of this thesis is to simulate the behavior of duplex stainless steel with precipitated σ-phase. The numerical simulations have been performed with a new implementation in the SIMLab Metal Model in the analysis program LS-DYNA. By doing so, we have been among the first to use this implementation, i.e. being alpha-testers of this software implementation. The material model has proven to be difficult to program, and several problems have occurred during the simulations. As a result, dr. Torodd Berstad has done many improvements to the software. Consequently simulations had to be rerun. This has been a great challenge but equally rewarding for us. We recommend that the reader keep this in mind.

Acknowledgements

We would first like to thank our supervisors Prof. Tore Børvik and Prof. Odd Sture Hopperstad at SIMLab for thorough follow-up, guidance and critique.

Secondly, great acknowledgement goes to the Dr. Torodd Berstad who has helped us with the many troubles we have encountered using the analysis program LS-DYNA. In general, we are thankful for all the help from the patient and friendly staff here at the Structural Engineering department.

To our friends and fellow students at our study room, we would like to thank you for creating a social atmosphere and for sharing knowledge and useful hints.

Lastly we would like to thank our girlfriends and our families for motivation and support.

Abstract

Duplex stainless steel (DSS) is a common material in offshore pipe fittings. A manufacturing defect has altered the behavior of the components through an erroneous heat treatment, which has led to precipitation of σ-phase. A report showing a strong correlation between precipitated σ-phase and the reduction in impact toughness, initiated a great interest in the offshore industry for further studies of the effect of precipitated σ-phase in DSS pipe fittings.

At SIMLab, numerous material tests and full-scale component tests of DSS pipe fittings containing precipitated σ-phase has been performed and reported. SIMLab is interested in a description of the numerical procedure to capture the behavior and especially the fracture seen in the laboratory tests. Even though previous numerical studies capture the behavior until cracking occurs and fracture initiates, the transition between the ductile- and brittle fracture, observed in the laboratory, has not been described in a satisfying manner in the full-scale component tests.

It is proposed that the effect of σ-phase must be incorporated in a material model. In addition a fracture criterion must be established to capture the combined effect of the ductile- and brittle fracture. To simulate this, the Gurson material model with an additional brittle fracture criterion has been applied. This approach has been applied to simulate a full-scale component test with DSS pipe fittings, with various amounts of σ-phase, exposed to dynamic impact loading.

Inverse modeling using the data from tensile tests in an optimization program, LS-OPT, performed the calibration of the material parameters in the Gurson material model. Further, the material model was intended verified in a complementary material test, the fracture toughness test. This test was additionally intended to calibrate the brittle fracture criterion. The material models were only verified to some extent, meaning that the tensile tests showed some good results compared to the laboratory test, but the fracture toughness tests did not give satisfying results.

The optimization of the material parameters was challenging, especially when the results were not directly transferable between plane solid (axisymmetric) - and brick element models used in the simulations. Therefore, multiple

optimizations had to be done in order to obtain material models with sufficient accuracy. The fracture toughness test was very hard to simulate due to a weakening in the material, not measured in the lab, caused by a cyclic loading prior to testing. Consequently, the simulations of the tests were not able to calibrate the brittle fracture criterion in a satisfying manner. The fracture criterion was therefore determined through a case study giving a plausible range of the critical values. In the full-scale impact tests no ductile fracture was present, but a highly sensitive brittle fracture was achieved in the simulations. The response of the pipe fittings compared to the laboratory results was not satisfying. The reasons for the deviations were found to be quite complex, but effects from mesh sensitivity and incorrect material optimization was found.

In this thesis it is seen that the Gurson material model is very complex, and without the proper knowledge it could be a source of error in itself. The influence of the Gurson model is limited for the specimens acting in a brittle manner. It is therefore considered unnecessary to apply this material model for these problems.

Sammendrag

Duplex rustfritt stål (DSS) er et vanlig materiale i offshore rørdeler. En fabrikasjonsfeil har endret oppførselen til komponentene gjennom en feilaktig varmebehandling, noe som har ført til utfelling av σ-fase. En rapport som viste sterk korrelasjon mellom utfelt σ-fase og reduksjon i stålets duktilitet og korrosjonsmotstand, innledet en stor interesse i offshoreindustrien for videre studier av effekten av utfelt σ-fase i DSS rørdeler.

Ved SIMLab er det gjennomført svært mange materialtester og fullskala komponenttester av DSS rørdeler som inneholder utfelt σ-fase og rapportert. SIMLab er interessert i en beskrivelse av numeriske prosedyrer for å fange oppførelsen, da spesielt brudd sett i laboratorietester. Selv om tidligere numeriske studier har klar å fange oppførelsen frem til sprekker oppstår og brudd initiereres, har overgangen mellom duktilt-og sprøtt brudd, slik som er observert i laboratoriet, ikke vært beskrevet på en tilfredsstillende måte i fullskala komponenttester.

Det ble foreslått at effekten av σ-fasen måtte innarbeides i en materialmodell. I tillegg måtte et ekstra bruddkriterium etableres for å fange opp den kombinerte effekten av duktilt-og sprøtt brudd. For å simulere dette har Gurson materialmodell blitt brukt med et ekstra sprøbruddskriterium. Denne fremgangsmåten har blitt brukt for å simulere en fullskala komponenttest med DSS rørdeler, med ulike mengder σ-fase, utsatt for dynamisk støtbelastning.

Ved hjelp av data fra strekktester har det blitt gjort inversmodeliring i optimaliseringsprogrammet LS-OPT for å bestemme materialparametrene i Gurson modellen. Videre var det tiltenkt at materialmodellen skulle bli verifisert gjennom en utfyllende materialtest. Denne testen var i tillegg ment til å kalibrere sprøbruddskriteriet. materialmodellen ble bare bekreftet til en viss grad. Det vil si, resultatene fra strekktesten viste til tider god overenstemmelse med oppførselen i laboaratoriet, men bruddtesten gav ikke tilfredstillende svar.

Optimalisering av materialparametere var utfordrende, spesielt med tanke på at resultatene ikke var direkte overførbar mellom aksesymmetriske- og volum elementmodellene som ble brukt i simuleringene. Derfor var flere optimaliseringer nødvendige for å oppnå materielle modeller med tilstrekkelig nøyaktighet. Bruddseighetstesten var svært vanskelig å simulere på grunn av

en svekkelse i materialet, som ikke var målt i laboratoriet, som var forårsaket av en syklisk belasting før testing. På grunn av dette var simuleringerene av testene ikke i stand til å kalibrere sprøbruddskriteriet på en tilfredsstillende måte. Bruddkriteriet ble derfor bestemt gjennom et case-studie som gav et plausibelt spekter av de kritiske verdiene. I fullskala testene med støt på rør, fant man ingen duktile brudd, men det ble i simuleringene oppnådd et svært følsomt sprøbrudd. Responsen av rørdelene var ikke tilfredsstillende med tanke på resultatene fra laboratoriet. Årsakene til avvikene viste seg å være ganske kompleks, men det ble funnet indisier på at elementnettet var svært følsomt og feil i de optimaliserte materialparametrene.

Det er i denne oppgaven erfart at Gurson modellen er meget kompleks. Uten tilstrekkelig kunnskap kan denne i seg selv lett bli en feilkilde. I og med at effekten av Gurson modellen er begrenset i prøvene som opptrer sprøtt, anses det derfor unødvendig å bruke denne materialmodellen for disse problemene.

List of Figures

Page

List of Tables

Contents

1. Introduction

This chapter will present the background and motivations that leads up to the problem statement. Furthermore, the conclusions from the articles this thesis is based on are presented and explained. Then the structure of the thesis with its scope and limitations is given.

1.1 Choice of Topic

Both authors are students in the Structural Engineering programme with in-depth study in calculations in structural mechanics. Subjects such as non-linear finite element method, mechanics of materials and structural dynamics are typical. During the fall of 2011 the choice of the subject for the master thesis was pretty clear, the Structural Impact Laboratory (SIMLab) provided a great deal of interesting subjects for the master thesis, where the subject "Impact on duplex steel pipes with precipitated sigma phase" was appealing. Both students are interested in learning more of the topics within these subjects. That is, non-linear finite element analysis, finite element modeling, numerical calculations and micro-structural problems in materials. Opportunities to acquire knowledge of these topics are provided when writing a thesis for SIMLab.

Duplex stainless steel (DSS) is a high strength steel, it is called duplex because of it's mixture of two-phase grain micro-structure of austenite and ferrite. During the heat treatment of the steel, from it's liquid to solid cool form, the mixture turns from pure ferrite structure to roughly 50/50 ferrite and austenite. Compared to other stainless steel, duplex stainless steel has very attractive material properties. It has higher strength, better toughness, ductility and stress corrosion cracking resistance than regular austenite or ferrite stainless steel grades (IMOA, 2012).

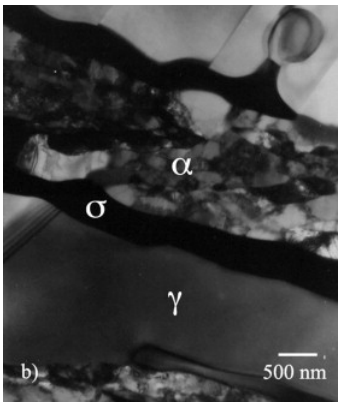

Figure 1.1: *Transmission electron microscopy photo, of a duplex steel heat treated at 875℃, showing sigma- phase (σ), Austenite (γ) and Ferrite (α),(Fargas et al., 2009)*

The duplex steel grade in question is the SAF 2205 (*S*andvik *A*ustenite-*F*errite), with 22 *wt.*% Chromium.

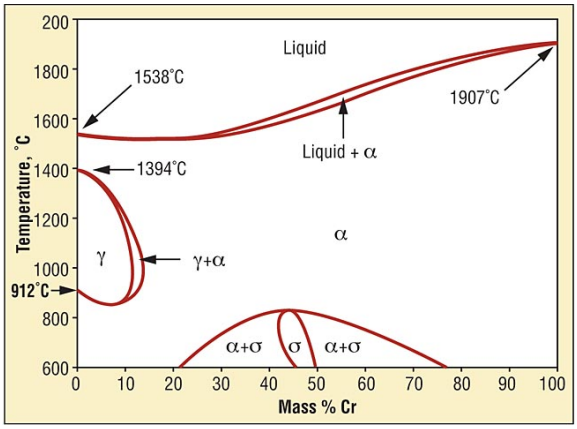

Figure 1.2: *Heat treatment of duplex stainless steel, showing when austenite(γ), ferrite(α) and sigma-phase (σ) are made, according to temperature and wt.% of Chromium (Cr). SAF 2205 has 22 wt.% Cr (Herring, 2012)*

During the heat treatment, the aim is to get a 50/50 mix of ferrite (α) and austenite(γ), but there are two major concerns with duplex steel. First the interaction between alloying elements, Chromium, Molybdenum, Nitrogen and Nickel, is a complex procedure. Second is the precipitation of

intermetallic phases (such as σ, ψ, π, R) and carbides (Stradomski and Dyja, 2005). It is particularly the precipitation of σ-phase that is interesting in this thesis. The precipitation of σ-phase occurs when temperatures are between 700-900℃, for steel containing Chromium between 20-80 wt.%, see figure 1.2. σ- phase consists of chromium and iron, which is hard, brittle and non-magnetic. In figure 1.1, the two-phase grain structure of austenite and ferrite is shown with the precipitated σ- phase on the grain boundary.

At only small amounts of σ-phase, a drastic reduction in ductility and corrosion resistance has been observed. It has been demonstrated in Kulbotten et al. (2009) and more thoroughly tested in Børvik et al. (2012). These tests, with their results and implications, will be explained in chapter 2. In the figures below, examples of the effect of σ-phase are shown. During dynamic impact loading, pipe fittings completely shatters when containing σ-phase, whereas the pipe fittings without σ-phase only deforms.

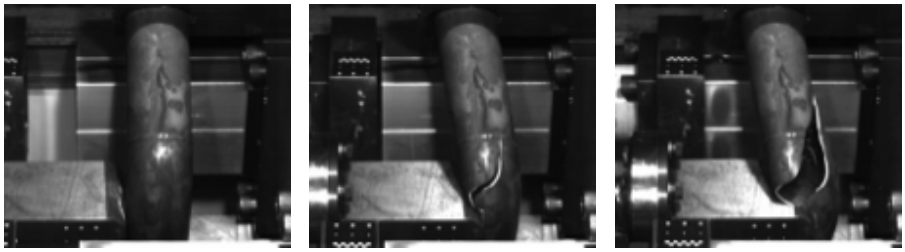

(a) 0 ms (b) 8 ms (c) 16 ms

Figure 1.3: *High speed pictures of steel pipe fittings, containing 15 vol.% precipitated sigma-phase content, subjected to impact, (Børvik et al., 2012)*

In the wake of Kulbotten's report, the oil and gas industry initiated a great interest for duplex stainless steel (DSS) with precipitated σ-phase used in pipe fittings offshore. To avoid extremely costly shut downs of pipelines, research on the effect of σ-phase was initiated. The results show a very brittle material behavior and reduction in the ductility of the steel and its corrosion resistance (Stradomski and Dyja, 2005). This is especially unfavourable in accidental analysis of impact forces in the offshore industry. Behavior of DDS pipe fittings with σ-phase has been studied thoroughly. In the report Børvik et al. (2009) numerous material tests were performed, further full scale component tests were reported in Børvik et al. (2010). Numerical studies are performed by simulating the tests with finite element analysis. Even though these studies capture the behavior until cracks and fractures

initiate (Austnes and Bjørklid, 2010), the ductile-brittle transition observed in the laboratory, is not yet described in a satisfying manner in the full-scale component.

1.2 Problem Statement

On the basis of previous experimental tests and numerical simulations, this thesis will investigate how to numerically describe the effect of σ-phase. To be able to do so, the effect of σ-phase must be incorporated in a material model. Further, fracture criteria must be established to capture the combined effect of ductile and brittle fracture.

For the simulations, the Gurson material model will be applied. This is a new implementation in the SIMLab Metal Model, for the finite element analysis program LS-DYNA. The Gurson material model, with an additional fracture criterion, is believed to be able to describe the ductile fracture and the transition to brittle fracture. The thesis will make an attempt to simulate a full-scale component DSS pipe fittings, containing various amounts of precipitated σ-phase, exposed to dynamic impact loading.

1.2.1 Scope

Since numerous laboratory tests are done by SIMLab, it is not necessary at this point to do any more testing. This thesis will only address the previous lab results and process the data for verification of corresponding simulations.

The effects of pre-charged hydrogen and temperature variation are disregarded.

To achieve the wanted results, it is required to have an extensive knowledge of the Gurson material model. This is acquired through literature studies and guidance from the academic supervisors at the institute of structural engineering. Further, this knowledge will be used when performing analysis in the finite element analysis programme LS-DYNA. Since the Gurson model is a new implementation in the SIMLab Metal Model, additional analytical approaches is necessary to verify the simulated results and will therefore be developed.

1.3 The Structure of the Thesis

The thesis is divided into these main chapters:

1. Introduction
2. Previous Work
3. Theory
4. Calibration of Material Model
5. Analytical Verification
6. Numerical Analysis of Component Test
7. Concluding Remarks

The first two chapters are an introduction to the thesis and previous work. At the end, a short summary with concluding remarks from the previous research papers is given. This is considered to be relevant and necessary for the completeness of the thesis. The next section contains the relevant theory to understand the Gurson material model. In calibration of the material model, inverse modeling of material parameters will be done, using the laboratory data from the tensile tests the and fracture toughness tests. Further an independent analytical procedure will be presented as a verification of the simulated results. These chapters lead to numerical analysis of the full-scale impact test. Finally, concluding remarks are reviewed and suggestions for further work end the thesis.

2. Previous Work

In this chapter previous work will be summarized and parts of the content are transcribed for completeness of the thesis. The material tests will be presented in a chronological order, starting with the initiating paper Kulbotten et al. (2009) and ending with the most recent work. All studies investigate the effect of precipitated σ-phase content in duplex stainless steel (DSS). The experimental program contains; Charpy impact test, quasi-static and dynamic tensile test, crack-tip opening displacement (CTOD) fracture toughness test and lastly; full-scale component test on real offshore pipe fittings exposed to quasi-static loading and dynamic impact loading. The conclusions from each report are summarized at the end of this chapter, to give a better understanding of status quo on this subject.

This thesis concentrates on duplex stainless steel (DSS) at room temperature (20℃). Tests concerning other issues, such as pre-charged hydrogen and temperature variations, will be excluded from this backtrack of previous work. The CTOD fracture test is only tested at a temperature -10 °, this is included despite the temperature deviation. The first material test is the Charpy impact test, which was the initiator for every material test done afterwards.

2.1 Charpy Tests

Statoil ASA carried out a Charpy impact toughness test and reported in Kulbotten et al. (2009). A total of 70 specimens were tested, which were sampled from 15 different, SAF 2205 DDS pipe fittings. The pipe fittings had different precipitated σ-phase content, the content of σ-phase were point counted after the tests. The impact tests were compared with the NORSOM M-630 requirements stating that; each test series have to absorb a minimum on average of 45 J and not a single specimen are allowed to absorb less than 35 J. The test was carried out using a Zwick/Roeell pendulum impact tester on Charpy V-notched specimens. The relevant results for this thesis is extracted and summarized in figure 2.1 and in table 2.1.

Table 2.1: *Results from impact toughness testing at +25℃ and subsequent σ-phase counting.*

Test temp. [℃]	Specimen ID	σ-phase content [%]	Size of test specimen [mm]	Impact toughness measured [J]	Corrected as per NORSOK [J]	Average [J]	Minimum [J]
+ 25 [℃]	Block 16	0.7	7.5	140	168	219	168
		0.0	7.5	258	310		
		0.1	5	120	180		
	Block 77	6.0	5	22	33	79	33
		3.9	5	28	42		
		0.3	5	107	161		
	Block 78	8.6	5	14	21	23	21
		9.8	5	17	26		

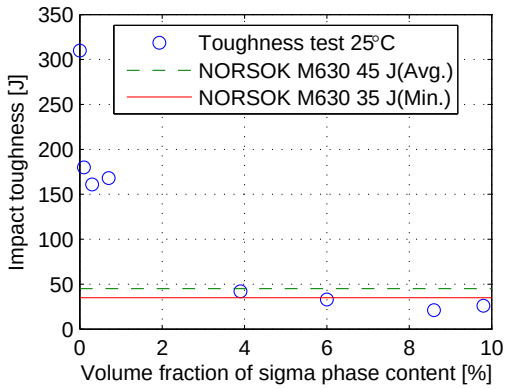

Figure 2.1: *Results from impact toughness testing and subsequent σ-phase counting, corresponding with table 2.1*

In the figure above, a dramatic drop in fracture toughness with increasing σ-phase levels is observed. The test implies that there is an exponential relation between fracture toughness and σ-phase levels, which consequently shook the oil and gas industry and initiated this research program.

2.2 Tensile Tests

SIMLab has done an experimental program for the tensile tests, this was reported in Børvik et al. (2010). The program consists of nine different test series. Here it is only focused on test series 1, 4 and 8, since these tests

were done at room temperature and were not pre-charged with hydrogen. 21 out of the 59 tensile tests are presented in table 2.2, divided into one dynamic and two quasi-static tensile test series. The tests were carried out using axisymmetric smooth specimens with gauge length of 5 mm and cross-sectional diameter of 3 mm, as shown in figure 2.2.

Table 2.2: *Experimental programme for tensile testing.*

Test series	Strain rate $[s^{-1}]$	Temp. [°C]	Pipe material direction	$\sigma-$ phase content (Num. of tests)		
				~ 0 *vol.* %	$1-5$ *vol.* %	~ 10 *vol.* %
1	$5 \cdot 10^{-4}$	+20	Longitudinal	3	2	2
4	$5 \cdot 10^{-4}$	+20	Hoop	2	2	2
8	50	+20	Longitudinal	4	2	2

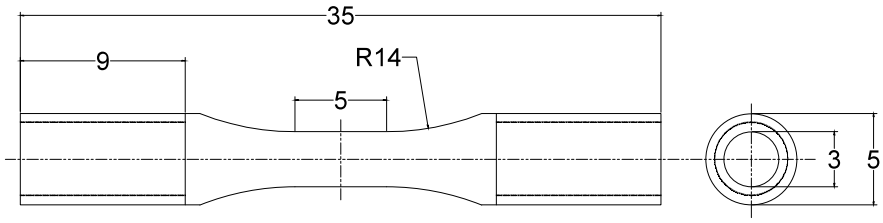

Figure 2.2: *Geometry of tensile specimen [mm]*

2.2.1 Quasi-Static Tensile Tests

Test series 1 and 4, covers the quasi-static test series. They were carried out using a 20 kN Dartec servo-hydraulic universal testing machine, with an Instro 8800 controller for displacement control. A purpose-made measuring jig; installed on a mobile frame with two perpendicular lasers, was used to ensure that the two diameters D_1 and D_2 always are measured at minimum cross-section. The cross-head velocity was 0.15 mm/min and given an initial strain rate in the gauge area of $5 \cdot 10^{-4} s^{-1}$.

The true stress and logarithmic strain were calculated as (Børvik et al., 2010):

$$\sigma = \frac{F}{A}, \qquad \varepsilon_l = ln\frac{A_0}{A} \tag{2.1}$$

Where F is the force, $A_0 = (\pi/4)D_0^2$ is the initial cross-section area and D_0 is the initial diameter of the gauge section. The current cross-sectional area where anisotropic plastic flow is allowed is then

$$A = \frac{\pi}{4}D_1 D_2 \tag{2.2}$$

The logarithmic strain at fracture is then calculated as

$$\varepsilon_f = ln\frac{A_0}{A_f} \tag{2.3}$$

where $A_f = (\pi/4)D_{1f}D_{2f}$ is the measured cross-sectional area of the specimen at fracture. The true stress/engineering stress relation and logarithmic strain/engineering strain relation (valid to incipient necking) are given as

$$\sigma_t = \sigma_e(\varepsilon_e + 1), \qquad \varepsilon_l = ln(\varepsilon_e + 1) \tag{2.4}$$

where σ_e and ε_e are engineering stress and strain, respectively. These expressions may now be used to calculate the engineering stress and strain based on the measured true (Cauchy) stress and logarithmic strain

$$\sigma_e = \frac{\sigma_t}{(\varepsilon_e + 1)} \tag{2.5}$$

Without σ-phase, e.i. ~ 0 vol.%, the DSS is very ductile. It yields at a true stress above 500 MPa and hardens considerably up to a true stress of nearly 1600 MPa, before it fails at about 1.4 in logarithmic strain. For increased content of σ-phase, a dramatic decrease in the fracture strain is seen. For specimens with $1-5$ vol.%, fracture strain drops to approximately 1.0 and for specimens with ~ 10 vol.% σ-phase to approximate 0.7. This gives a reduction in fracture strain to 30% and 50%, compared with ~ 0 vol.% precipitated σ-phase.

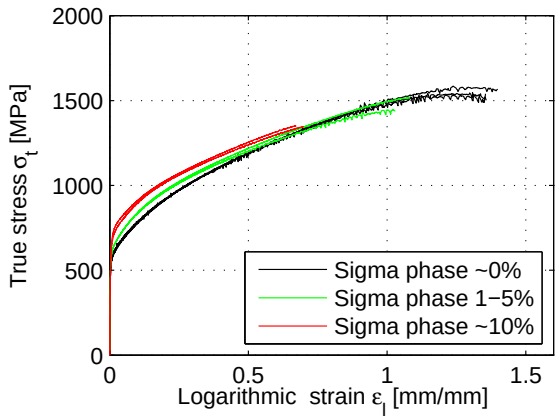

Figure 2.3: *True stress- logarithmic strain results from quasi-static tensile test series 1*

Another observation is that increasing σ-phase, increases the flow stress. Which is mainly caused by the increased initial hardening rate due to the brittleness of the precipitated σ-phase. At higher strains the hardening rate is lower for higher contents of σ-phase, see figure 2.3. Even with a severe drop in fracture strain from the specimens containing σ- phase, the material still dissipates a considerable amount of energy.

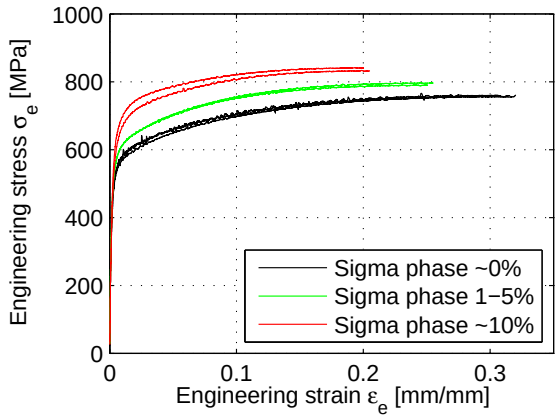

Figure 2.4: *Engineering stress-strain results from quasi-static tensile test series 1 until necking*

Figure 2.4 gives typical engineering stress-strain curves from test series 1. These curves are calculated by equation 2.5 based on the measured true

stress-logarithmic strain values. The curves are plotted to the strain at maximum load, i.e. the onset of necking. It is seen that the strain at necking decreases with increasing content of σ-phase, which is caused by higher stress levels and lower hardening rate at these strains (Børvik et al., 2010).

2.2.2 Dynamic Tensile Tests

This dynamic tensile test involves test series 8; in room temperature (+20 ℃) with a strain rate of 50 s^{-1}. The tests were carried out in a hydro-pneumatic tension machine, for the full test set-up see Børvik et al. (2010). The load resisted by the specimen was measured with strain gauges. The elongation of the specimen was measured by a displacement transducer, sensing the displacement of a metallic strip connected to the piston shaft.

In figure 2.5, true stress-logarithmic strain is plotted. The variations between the parallel tests are limited but larger than for the quasi-static tensile test. The trends for the dynamic tests are similar to the quasi-static as the content of σ-phase increases. That is, higher flow stress, slightly increase in yield stress, an increase in strain hardening and a decrease in strain at necking. All the specimens failed in a shear fracture mode.

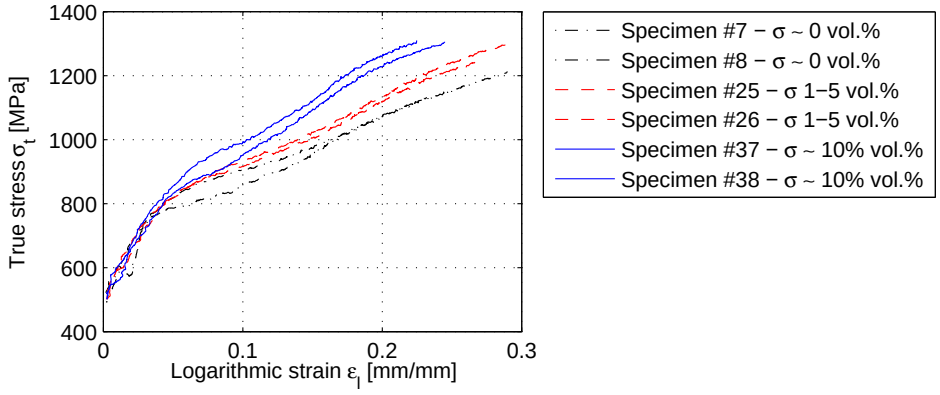

Figure 2.5: *True stress - logarithmic strain results from dynamic tensile test series 8*

2.3 CTOD Fracture Toughness Tests

The fracture toughness tests were determined by conducting a crack-tip opening displacement(CTOD) on single-edge notched bend(SENB) specimens according to the BS7448-1 standard, and reported in Lange and Hassel (2010). The test specimen, anvil and pendulum acting in the tests are shown in figure 2.6.

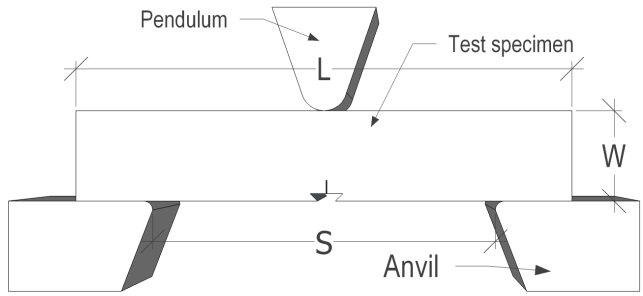

Figure 2.6: *Test set-up for the CTOD fracture toughness test*

The specimens were DSS pipe fittings and contained σ-phase levels equal to the tensile test, i.e. σ-phase content of ~ 0 *vol.*%, ~ 5 *vol.*% and ~ 10 *vol.*%. Every specimen had a nominal cross section of $7 \cdot 7$ mm, except ~ 10 *vol.*% specimens had nominal cross section of $5 \cdot 5$ mm. The CTOD testing was done in a 20 kN Dartec universal servo-hydraulic test machine, and the tests were only performed with the specimens submerged in cooled alcohol with a temperature of -10℃.

An MTS clip gauge was used to measure the crack mouth opening displacement (CMOD). The initial opening was 2 mm and the maximum travel was 4 mm. The test machine recorded force and vertical displacement during testing. After testing; the specimens were cooled in liquid nitrogen, before the fracture surface was opened for inspection.

In figure 2.7, the CTOD fracture toughness tests are summarized. After inspecting the σ-phase content after testing, it was found that the assumed σ-phase level of the SENB specimens in test series with $1-5$ *vol.*% was between $0.5-1$ *vol.*%. As seen in the figure, the increase in σ-phase content of 0 *vol.*% to $0.5-1$ *vol.*% gives an reduction in fracture toughness of about 40%, but there is a considerable spread in the test results. For SENB specimens containing σ-phase content of 10 *vol.*%, gives a severe reduction in fracture toughness, more than 90% compared to 0 vol.% σ-phase content.

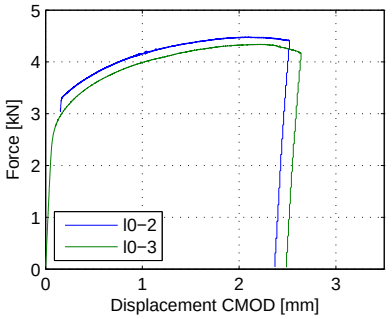

(a) σ-phase content ~ 0

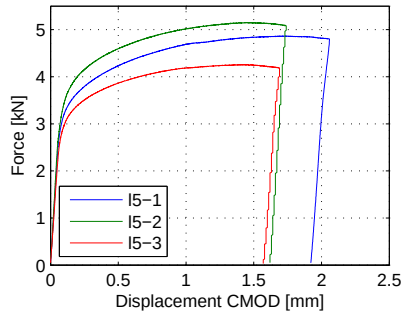

(b) σ-phase content $1 - 5$

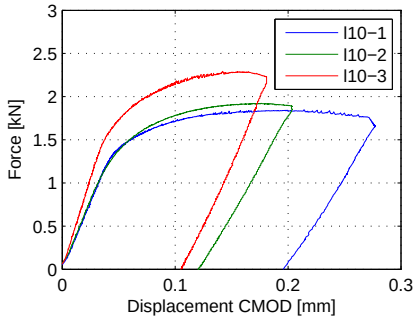

(c) σ-phase content ~ 10

Figure 2.7: *CTOD toughness test of longitudinal specimens*

In general the fracture toughness were lower for the specimens taken in the hoop direction compared to the specimens from the longitudinal directions.

2.4 Full-Scale Impact Tests

The experimental program presented in the report Børvik et al. (2012), contains both quasi-static and dynamic impact tests on real 3" pipe fittings. The program tests four quasi-static ($QS1 - 4$) and seven dynamic ($D1 - 7$) impact tests on 3" pipes, and three similar dynamic tests on 2" pipes ($D7 - 10$). The nominal thickness for the 3" pipes were 3.05 mm, where the wall thickness varied considerably over the cross-section, keep in mind that this could be very important to be aware of in an analytical or numerical analysis.

All the pipes tested were of the same material, duplex stainless steel (grade 2205), where the fittings were a 90° elbow of class AD200/BD200, or similar, with or without σ-phase. The elbow were welded to two straight pipes, without σ-phase. The test program contains testing of four different levels of precipitated σ-phase. These were ~ 0 $vol.\%$, $2-5$ $vol.\%$,~ 8 $vol.\%$ and ~ 15 $vol.\%$ σ-phase.

The fittings were loaded by a rigid, hemispherical nose with a radius of 25 mm and of length ~ 120 mm for all the tests. More details and figures can be found in Børvik et al. (2012).

2.4.1 Quasi-Static Impact Tests

The quasi-static part of the program was done in a 500 kN Dartec servo-hydraulic universal testing machine, under displacement control. The maximum actuator stroke of this machine is approximately 100 mm. The loading rate during testing was set to 2 mm/min, and the force- displacement relation was registered by the actuator. Two linear variable differential transformers (LVDT) were used to check if any axial contraction took place at the clamps, to verify if the pipe was thoroughly clamped at the supports during testing. Additional details and figures can be found in Børvik et al. (2012). The results from the quasi-static test are summarized in table 2.3.

Table 2.3: *Experimental program for quasi-static impact tests*

Test Number	Loading rate	Pipe size	Assumed $\sigma-$ phase level	Counted $\sigma-$ phase level	Fracture
QS1	$2mm/min$	3”	~ 0 $vol.$	N/A	No
QS2	$2mm/min$	3”	$2-5$ $vol.$	N/A	No
QS3	$2mm/min$	3”	~ 8 $vol.$	N/A	Crack
QS4	$2mm/min$	3”	~ 15 $vol.$	N/A	Yes

2.4.2 Dynamic Impact Tests

For this test a kicking machine has been used. The kicking machine, shown in figure 2.8, accelerates a trolley towards the test specimens, i.e, the pipe fittings. The test specimens are fixed to a reaction wall at impact. More detailed information regarding the operation and the set-up of the kicking machine can be found in Hanssen et al. (2003).

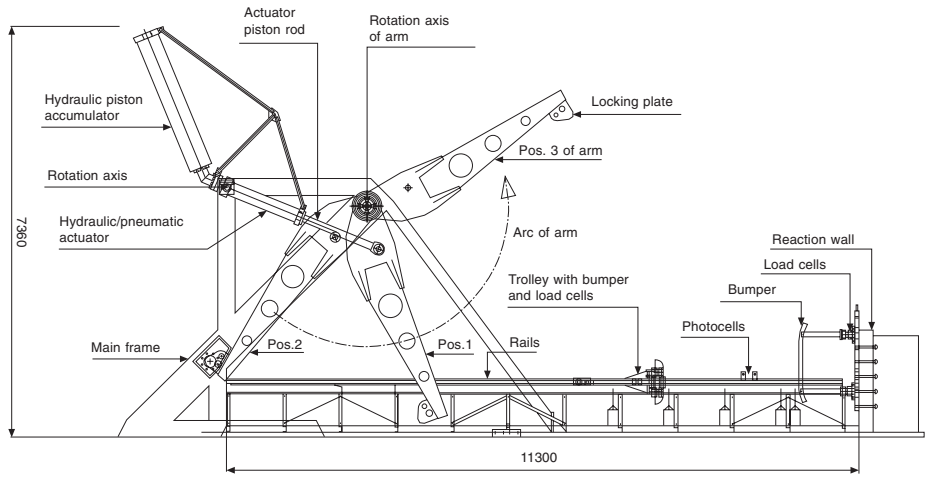

Figure 2.8: *Kicking machine used during dynamic impact tests (Hanssen et al., 2003)*

In these tests the mass of the trolley, including the hemispherical nose, was 378 kg. The velocities spans between 5 m/s and 10 m/s were carried out, which gives initial impact energies of 4.7 kJ and 18.9 kJ, respectively. These energies is equivalent to dropped object from heights up to $15 - 20$ m, from tools and scaffolding parts, that can be found and may damage pipes and such on a offshore process' plants. The results from the dynamic test are summarized in table 2.4.

In figure 2.9 the force levels between the nose and the pipe-fittings are plotted. These results show little deviation between force levels and σ-phase content, apart from the pipe-fittings containing ~ 8 vol.% σ-phase. Some of these specimens have a very brittle fracture propagation, which is reflected in the level of energy absorbed.

Table 2.4: *Experimental programme for dynamic impact tests*

Test Number	Loading rate	Pipe size	Assumed $\sigma-$ phase level	Counted $\sigma-$ phase level	Fracture
D1	$10m/s$	3”	~ 0 $vol.\%$	0.0	No
D2	$10m/s$	3”	$2-5$ $vol.$ $\%$	4.3	No
D3	$10m/s$	3”	~ 8 $vol.\%$	9.6	Yes
D4	$7m/s$	3”	~ 8 $vol.\%$	N/A	Yes
D5	$5m/s$	3”	~ 8 $vol.\%$	9.9	No
D6	$10m/s$	3”	~ 15 $vol.\%$	14.4	Crack
D7	$5m/s$	3”	~ 15 $vol.\%$	14.9	Yes
D8	$5m/s$	2”	$1-2$ $vol.\%$	N/A	No
D9	$10m/s$	2”	~ 0 $vol.\%$	N/A	No
D10	$10m/s$	2”	$1-2$ $vol.\%$	N/A	Crack

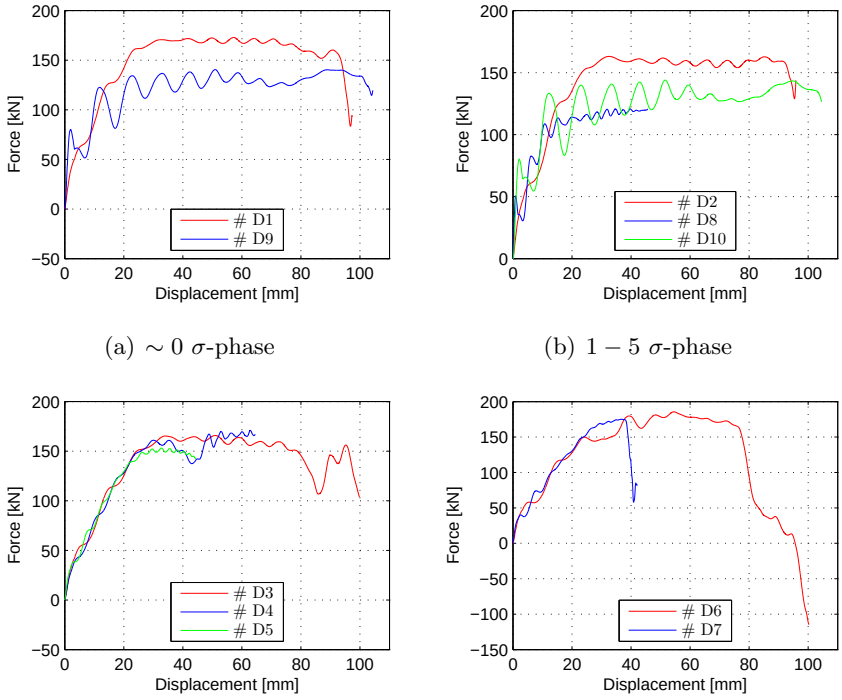

(a) ~ 0 σ-phase

(b) $1-5$ σ-phase

(c) ~ 8 σ-phase

(d) ~ 15 σ-phase

Figure 2.9: *Dynamic tensile tests corresponding to table 2.4*

2.5 Summary of previous work

The Charpy impact toughness test showed a strong correlation between σ-phase content and impact toughness. Already at a small fraction of σ-phase (≈ 1 *vol.*%), the impact toughness is dramatically reduced and does not satisfy the NORSOK requirements, see table 2.1 and figure 2.1. This may be from the combined effects of high strain rates, high brittleness of the precipitated σ-phase, and the high stress triaxiality in the V-notched specimens. The report initiated an increased interest for DSS with precipitated σ-phase content.

In the tensile test program, it was found that the effect of σ-phase in the tensile ductility of the DSS is considerable. Independent of the tensile direction, strain rate and temperature, the logarithmic strain at fracture decreased almost linearly with σ-phase levels between 0 *vol.*% and 10 *vol.*%. It was further observed that the tensile ductility decreased significantly with strain rate, while the influence of temperature was minor. The logarithmic fracture strain was still around 0.5, indicating a reasonably good ductility of the material in uniaxial tension even at 10 *vol.*% σ-phase.

The crack-tip opening displacement (CTOD) fracture toughness tests, said that increased content of σ-phase reduced the fracture toughness, and a distinct drop could be observed between the series with 2-5% (counted 1-2%) and 10% σ-phase.

Under the quasi-static impact loading on 3" pipe fittings, there was no noticeable effect of σ-phase, between 0 *vol.*% $\leq \sigma \leq$ 8 *vol.*%, in the force-displacement response. But as the level of σ-phase increased above 8 *vol.*%, perpendicular cracks were seen for large displacements. At 15 *vol.*% σ-phase, extensive fracture and cracking were observed.

The same trend is seen under the dynamic impact test on 3" pipes, that the effect of σ-phase is small at lower levels of precipitated σ-phase, i.e. 0 *vol.*% $\leq \sigma \leq$ 5 *vol.*%. During these tests there were no fracture found by visual inspection. At σ-phase of 8 *vol.*%, fracture only occurred at the highest impact velocities, at lower velocities there were only minor cracks that could be seen. In contrast, the components behaved very brittle with fragmentation and sever crack propagation at higher levels of σ-phase (15 *vol.*%). Also, the pipes nearly split in two for all impact velocities.

The dynamic tests showed a much higher force level compared to the quasi-static tests. This probably caused by the materials' tendency of being strain

rate sensitive, often observed in duplex stainless steel. Therefore similar tests were done on 2" pipes with precipitated σ-phase, $0\ vol.\% \leq \sigma \leq 2\ vol.\%$. However, neither fracture nor cracks were observed under the given impact conditions.

3. Theory

This chapter contains the constitutive relations and the fracture mechanics applied in this thesis. A porous plasticity model, namely the Gurson material model will be presented (Gurson, 1975). The study requires a thorough theoretical background; consequently this chapter will cover the constitutive relations in detail. At first, a description of the basic assumptions of the Gurson material model is described. Secondly, the development and assumptions under elastic straining is stated. Further, a description of the yield function with its properties and the development under plastic straining. Even though damage tends to make materials anisotropic (Hopperstad and Børvik, 2012), only isotropic materials with isotropic damage evolution will be covered. The last section will cover brittle fracture and the implementation of the combined fracture criteria will be mentioned.

The Gurson model is the basis for the solver applied in this thesis and implemented in the FEM program LS-DYNA. The theory manual (Hopperstad, 2012) from the SIMLab Metal Model states in the extended Gurson section:

The field of application of this model is quasi-static and dynamic simulations of structures made of materials with persistent isotropy where damage softening from void growth is important.

The theory presented in this chapter can be found in the references beneath. For more in depth studies on these fields the reader is referred to Hopperstad and Børvik (2012), Anderson (2005), Needleman and Tvergaard (2000), Pineau (2006), Pineau (2008) and Tvergaard and Needleman (1993).

3.1 Gurson Model

In the hypothesis the σ-phase precipitation is considered as brittle second-phase particles, which causes nucleation of voids. Based on the assumptions of voids, the material model must be able to describe, nucleation-, growth- and coalescence of voids, of which numbers of mathematical models are proposed. The most widely used was proposed by Gurson. This approach

modified by among others Needleman and Tvergaard (2000), will be discussed here.

The original Gurson material model is developed from a cylinder consisting of a cylindrical void. Further assuming an elastic perfectly plastic material behavior, the theory has developed a yield criterion dependent on the appearance of voids. The most basic assumption is then obviously, the appearance of voids in porous metals. Thus the usual assumption, that metals are incompressible materials, is no longer valid. The theory is further explained through a microscopic representative volume element (RVE) with a single void, shown in figure 3.1. The infinitesimal volume of the RVE can be decomposed in two parts

$$dV = dV_\omega + dV_M \tag{3.1}$$

where dV_ω and dV_M represent the infinitesimal volume of the void and the infinitesimal matrix volume, respectively. The void is interpreted as a measure for the damage evolution in the material, and is presented as a damage variable representing the fracture of voids of the total volume

$$\omega = \frac{dV_\omega}{dV} \tag{3.2}$$

(a) Initial $\omega_0 = 0.001$ (b) At fracture $\omega_{cr} = 0.15$

Figure 3.1: *Representative volume element with load carrying area reduced by defects in the form of microvoids*

In figure 3.1(a) the initial void volume fraction ω_0 is shown with a typical value for high strength steel (Avramovic-Cingara et al., 2009). When the RVE experience plastic straining the void grows and voids nucleate. Eventually the void becomes sufficiently large and it will coalesce with a neighbouring void, i.e. join another void. When the coalescence is initiated, formation

of macro cracks happens and the material will rapidly go towards failure. Figure 3.1(b) shows the void volume fraction at fracture ω_{cr} with values suggested by Tvergaard and Needleman (1993). It can easily be seen that at such void volumes the material is severely damaged. Thus, assuming that at a critical void volume fraction ω_{cr} represent the end of the materials load carrying capacity is reasonable.

3.1.1 Elastoplasticity

A basic assumption of plasticity models is that one can decompose the strain tensor ε_{ij} into an elastic and a plastic part

$$\varepsilon_{ij} = \varepsilon^e_{ij} + \varepsilon^p_{ij} \tag{3.3}$$

where ε^e_{ij} is the elastic strain tensor and ε^p_{ij} is the plastic strain tensor. The elastic part is assumed to be reversible and the plastic part is irreversible, causing the material to flow plastically and dissipate energy.

Another common decomposition is the sum of deviatoric (distortional)- and volumetric (dilatational) strain/stress tensors

$$\begin{aligned}
\sigma_{ij} &= \sigma^{'}_{ij} + \sigma_H \\
\sigma_H &= \frac{1}{3}\sigma_{kk}\delta_{ij} \\
\varepsilon_{ij} &= \varepsilon^{'}_{ij} + \frac{1}{3}\varepsilon_V\delta_{ij} \\
\varepsilon_V &= \varepsilon_1 + \varepsilon_2 + \varepsilon_3 = \varepsilon_{kk}
\end{aligned} \tag{3.4}$$

where the deviatoric stress tensor $\sigma^{'}_{ij}$ tends to distort the material, i.e. change the shape of the stressed body. The hydrostatic stress σ_H causes change in volume. The strain/stress deviator has the property that the sum of its normal components is identically equal to zero.

For isothermal conditions the elastic relations is simplified and the elastic stress then yields

$$\sigma_{ij} = \lambda_e \varepsilon^e_{kk}\delta_{ij} + 2\mu_e\varepsilon^e_{ij} \tag{3.5}$$

where δ_{ij} is the Kronecker delta and the Lamé constants, λ_e, μ_e, are defined as

$$\lambda_e = \frac{\nu E}{(1+\nu)(1-2\nu)}, \quad \mu_e = \frac{E}{2(1+\nu)} \tag{3.6}$$

The Poisson's ratio ν is assumed to be constant.

3.1.2 Yield Criterion

The Gurson yield function for a material containing voids is

$$f(\sigma, \omega, \sigma_M) = \frac{\sigma_{eq}^2}{\sigma_M^2} + 2\omega\beta_1 \cosh\left(\frac{3\beta_2\sigma_H}{2\sigma_M}\right) - 1 - \beta_3\left(\omega\right)^2 \leq 0 \tag{3.7}$$

where the macroscopic equivalent stress is expressed through the von Mises stress as

$$\sigma_{eq} = \sqrt{3J_2} = \sqrt{\frac{3}{2}\sigma'_{ij}\sigma'_{ij}} \tag{3.8}$$

and σ'_{ij} defined in equation 3.4 is the deviatoric stress tensor. σ_M is the microscopic equivalent stress of the unvoided matrix material and σ_H is the hydrostatic stress from equation 3.4. The fitting parameters, β_i, are proposed by Tvergaard (1982), with suggested values $\beta_1 = \frac{3}{2}$, $\beta_2 = 1$ and $\beta_3 = \beta_1^2$. At yielding, equation 3.7 gives the equivalent stress as a function of the material strength, the void volume fraction (ω) and the hydrostatic stress

$$\sigma_{eq} = \sigma_M\sqrt{1 + \left(\omega\beta_1\right)^2 - 2\omega\beta_1\cosh\left(\frac{3\beta_2\sigma_H}{2\sigma_M}\right)} \tag{3.9}$$

as a consequence of increasing magnitude of hydrostatic stress and void volume fraction, the equivalent stress decreases and the material will eventually completely loose its load-carrying capacity as seen in figure 3.2.

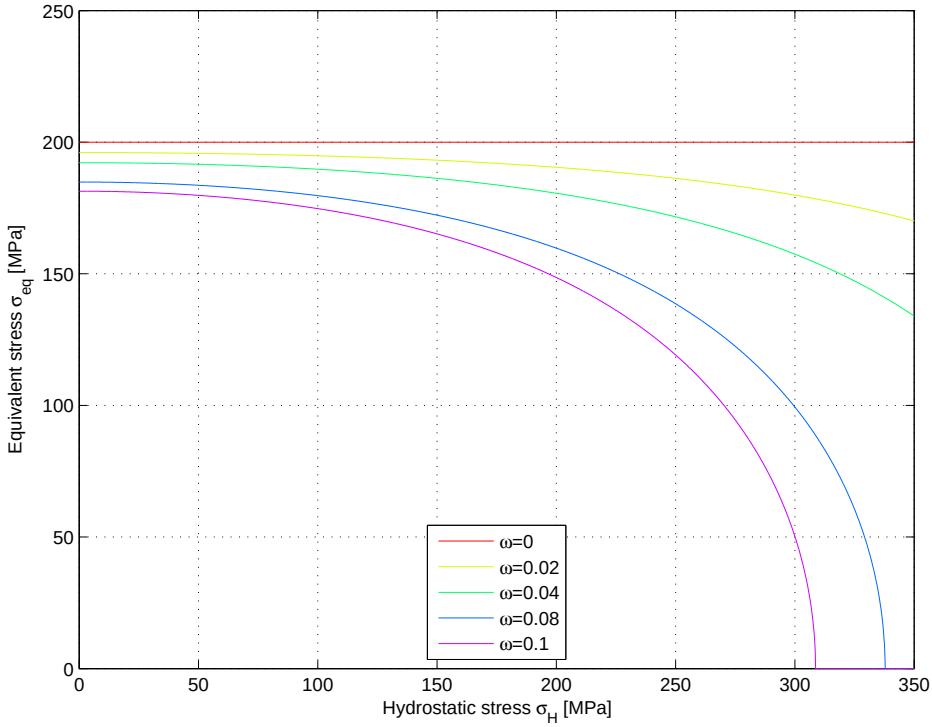

Figure 3.2: *The load carrying capacity of σ_{eq} as a function of the hydrostatic pressure σ_H for different values of ω*

3.1.3 Flow Rule

The plastic flow rule defines the plastic strain rate tensor $\dot{\varepsilon}^p_{ij}$ in a way that ensures non-negative dissipation, which comes as a requirement from the second law of thermodynamics. Here the associated flow rule is applied; i.e. the plastic potential is associated with the yield function. This leads to

$$\dot{\varepsilon}^p_{ij} = \dot{\lambda}\frac{\partial f}{\partial \sigma_{ij}} \tag{3.10}$$

The plastic flow is dependent on the rate of the plastic parameter $\dot{\lambda}$ and the yield surface gradient $\partial f/\partial \sigma_{ij}$. The gradient can be calculated by modifying the equation using equation 3.4, the gradient then becomes

$$\begin{aligned}\frac{\partial f}{\partial \sigma_{ij}} &= \frac{\partial}{\partial \sigma_{ij}}\left[\frac{\sigma_{eq}^2}{\sigma_M^2} + 2\omega\beta_1 \cosh\left(\frac{\beta_2 \sigma_{ij}\delta_{ij}}{2\sigma_M}\right) - 1 - (\omega\beta_1)^2\right] \\ &= 2\frac{\sigma_{eq}}{\sigma_M^2}\frac{\partial \sigma_{eq}}{\partial \sigma_{ij}} + \frac{\beta_1\beta_2\omega}{\sigma_M}\sinh\left(\frac{\beta_2\sigma_{ij}\delta_{ij}}{2\sigma_M}\right)\delta_{ij}\end{aligned} \tag{3.11}$$

To differentiate the equivalent stress we use equation 3.8 and obtain

$$\begin{aligned}\frac{\partial \sigma_{eq}}{\partial \sigma_{ij}} &= \frac{\partial}{\partial \sigma_{ij}}\left(\sqrt{\frac{3}{2}\left(\sigma_{ij} - \frac{1}{3}\sigma_{kk}\delta_{ij}\right)\left(\sigma_{ij} - \frac{1}{3}\sigma_{kk}\delta_{ij}\right)}\right) \\ &= \frac{\frac{3}{2}\left(\sigma_{ij} - \frac{1}{3}\sigma_{kk}\delta_{ij}\right)2}{2\sigma_{eq}} = \frac{3}{2}\frac{\sigma_{ij}^{'}}{\sigma_{eq}}\end{aligned} \tag{3.12}$$

Inserted in equation 3.11 we get

$$\frac{\partial f}{\partial \sigma_{ij}} = 3\frac{\sigma_{ij}^{'}}{\sigma_M^2} + \frac{\omega\beta_1\beta_2}{\sigma_M}\sinh\left(\frac{3\beta_2\sigma_H}{2\sigma_M}\right)\delta_{ij} \tag{3.13}$$

Finally, we get an expression for the plastic strain rate, which can be divided into deviatoric and volumetric parts, respectively. As we can see on the right side of equation 3.14

$$\dot{\varepsilon}_{ij}^p = \dot{\lambda}\left(3\frac{\sigma_{ij}^{'}}{\sigma_M^2} + \frac{\beta_1\beta_2\omega}{\sigma_M}\sinh\left(\frac{3\beta_2\sigma_H}{2\sigma_M}\right)\delta_{ij}\right) \tag{3.14}$$

Readily this gives an expression for the volumetric strain rate given as

$$\dot{\varepsilon}_V^p = 3\dot{\lambda}\frac{\beta_1\beta_2\omega}{\sigma_M}\sinh\left(\frac{3\beta_2\sigma_H}{2\sigma_M}\right) \tag{3.15}$$

To ensure positive dissipation in the plastic domain, we invoke power conjugacy

$$\sigma_{ij}\dot{\varepsilon}_{ij}^p = \dot{\lambda}\sigma_{ij}\frac{\partial f}{\partial \sigma_{ij}} \geq 0 \tag{3.16}$$

First, recall that the sum of the normal component in the deviatoric stress tensor is equal to zero. Then, by combining equation 3.13, 3.16 and assuring positive dissipation using $x \sinh x > 0$ for $x \neq 0$ we get

$$\sigma_{ij}\dot{\varepsilon}^p_{ij} = 3\dot{\lambda}\left(\frac{\sigma^{'}_{ij}\sigma^{'}_{ij}}{\sigma^2_M} + \frac{\beta_1\beta_2\omega\sigma_H}{\sigma_M}\sinh\left(\frac{3\beta_2\sigma_H}{2\sigma_M}\right)\right) \tag{3.17}$$

Loading and Unloading Conditions

Conditions must be established to distinguish between elastic- and plastic loading/unloading. The UMAT uses the *Kuhn-Tucker* conditions. These conditions require a stationary yield surface, meaning that the plastic flow vanishes in the elastic domain.

$$f \leq 0, \quad \dot{\lambda} \geq 0, \quad \dot{\lambda}f = 0 \tag{3.18}$$

Here f is the yield function and $\dot{\lambda}$ is the time differentiated plastic parameter.

3.1.4 Work-Hardening Rule

By definition the equivalent plastic strain is related to the flow stress of the matrix material as conjugate in power, i.e

$$\sigma_{ij}\dot{\varepsilon}^p_{ij} = (1-\omega)\sigma_M\dot{\varepsilon}^p_M \Rightarrow \dot{\varepsilon}^p_M = \frac{\sigma_{ij}\dot{\varepsilon}^p_{ij}}{(1-\omega)\sigma_M} \tag{3.19}$$

Since the plastic matrix strain is developed from equation 3.16 we see that the plastic matrix strain $\dot{\varepsilon}^p_M$ must be non negative.

For materials insensitive to viscosity, i.e independent of the strain rate, the isothermal matrix strength is defined as

$$\sigma_M = \sigma_y + \sum_{i=1}^{n} R_i \tag{3.20}$$

At reference temperature, the yield stress $\sigma_y = \sigma_0$. The UMAT uses the Voce hardening represented by n isothermal isotropic hardening terms R_i

$$R_i = Q_i \left(1 - e^{-C_i \varepsilon_M}\right), \quad C_i = \frac{\theta_i}{Q_i} \tag{3.21}$$

On rate form the given conditions can be developed as

$$dR_i = \theta_i \left(1 + \frac{R_i}{Q_i}\right) d\varepsilon_M \Rightarrow \frac{dR_i}{d\varepsilon_M} = \theta_i e^{-C_i \varepsilon_M} \tag{3.22}$$

3.1.5 Nucleation and Growth of Voids

In section 3.1, the different stages of damage evolution where mentioned. Written in a mathematical form, we express the change in void volume fraction as

$$\dot{\omega} = \dot{\omega}_n + \dot{\omega}_g + \dot{\omega}_s \tag{3.23}$$

the indices n, g and s represent nucleation, void growth and shearing respectively. The void shearing term accounts for the voids tendency to become elliptic under shear deformations. However, for simplicity this term is omitted. At first the nucleation is neglected, thus only growth of initial voids is present. To develop the void growth relation, we assume that the matrix material is plastically incompressible, i.e. the matrix volume remains constant throughout the deformation. Thus, the only contribution to the volumetric strains is the growth of existing voids. In addition, the elastic strains are neglectable compared to the plastic strains. These assumptions form the basis of the mass conversation of the macroscopic material element

$$(1 - \omega_0)\, \rho_m dV_0 = (1 - \omega)\, \rho_m dV \tag{3.24}$$

The initial void volume fraction is represented by ω_0. The density of the matrix material, ρ_M, is assumed not to vary with the deformation, and the initial- and current infinitesimal volume of the macroscopic element through dV_0 and dV. Further, to obtain the growth of the void volume fraction we must differentiate with respect to time. Applying the chain rule we get

$$0 = \dot{\omega} \rho_m dV + (1 - \omega)\, \rho_m (\dot{dV}) \tag{3.25}$$

As long as the growth of void fraction is the only growth considered, and small deformations are assumed $(d\dot{V})/dV_0 \approx (d\dot{V})/dV = \dot{\varepsilon}_V^p$ and combining equation 3.25 and 3.15 the void fraction growth becomes

$$\dot{\omega}_g = 3\dot{\lambda}\,(1-\omega)\,\frac{\beta_1\beta_2\omega}{\sigma_M}\sinh\left(\frac{3\beta_2\sigma_H}{2\sigma_M}\right) \tag{3.26}$$

The nucleation of voids happens when a sufficient stress is applied to break the interfacial bonds between a second phase particle and the matrix. Numerous models are presented, both stress and strain driven, but the UMAT is based on the latter case. The void fraction growth due to nucleation of void is here defined as

$$\dot{\omega}_n = D\dot{\varepsilon}_M \tag{3.27}$$

where

$$D = \frac{\omega_N}{S_N\sqrt{2\pi}}\left[-\frac{1}{2}\left(\frac{\varepsilon_M - \varepsilon_N}{S_N}\right)^2\right] \tag{3.28}$$

In this nucleation rule three material constants must be defined. ω_N is the volume fraction of void nucleating particles, ε_N is the mean plastic strain for nucleation and S_N is its associated standard deviation.

Coalescence of Voids

With initial voids and nucleations of voids growing, plastic straining and increased hydrostatic stress will eventually cause coalescence. An interpretation of this phenomenon is that neighbouring elements grow together and a macrocrack develops. To implement the accelerated void growth in the UMAT, a critical value of $\omega = \omega_c$ is defined, where $\omega \geq \omega_c$ represent the start of coalescence of voids. The void volume fraction is then substituted with an effective void volume fraction defined by

$$\omega^*(\omega) = \begin{cases} \omega & \text{for } \omega \leq \omega_c \\ \omega_c + \dfrac{\omega_u - \omega_c}{\omega_F - \omega_c}\,(\omega - \omega_c) & \text{for } \omega > \omega_c \end{cases} \tag{3.29}$$

$\omega_u = 1/\beta_1$ and $\omega^*(\omega_F) = \omega_u$. At the point where the material no longer has a load-carrying capacity the void volume fraction has reached the critical value ω_{cr}, which normally lies within the range $\omega_c < \omega_{cr} < \omega_F$.

3.2 Brittle Fracture

The Gurson model is considered a ductile material model, and is therefore not capable of capturing the brittle behavior experienced in the laboratory. To be able to do so, a brittle fracture criterion must be implemented in the material model.

It is widely known that brittle fractures are closely governed by the maximum principle stress. A criterion implementing this is proposed by Needleman and Tvergaard (2000) as

$$\frac{1}{V_{gr}} \int_{V_{gr}} \sigma_1 dV = \sigma_c$$

where V_{gr} is the cleavage grain volume and σ_1 is the maximum principle stress. The criterion is temperature and strain rate independent, and is defined as a specified material region with a maximum stress given as σ_c. Numerically this implies that the combined constrain erodes the critical element by either a maximum stress or maximum void volume fraction.

This chapter has given an introduction to the Gurson material model with governing equations and brief discussions of its physical behavior. The equations and statements given in this section will be used to substantiate further assumptions when interpreting results and obtaining analytical procedures.

4. Calibration of Material Model

The material model will be calibrated trough numerical simulations, such as tensile- and three point bending tests. The objective is to optimize the material parameters in the Gurson material model. The optimizations will be performed in LS-OPT through inverse modeling of the test specimens, where the laboratory test results are used as target curves. All simulations will be performed with the explicit solver available in the finite element code LS-DYNA. The material model is intended to be partially verified and further calibrated by the toughness test (CTOD) and later on used in the full scale component test.

4.1 Baseline Material Model

In all simulations the specimens have the physical properties of SAF 2205 DSS, as per Sandvik (2012) are given in table 4.1. If not specifically mentioned, default values are used as input values in LS-DYNA.

Table 4.1: *Material properties of SAF 2205*

Young's modulus E [MPa]	Poisson's ratio ν [N/A]	Thermal expansion α [$^\circ K^{-1}$]	Specific heat capacity C_p [Nmm/tonne·°K]	Density ρ [tonne]
2.0E+05	0.3	1.3E+05	4.8E+08	7.8E-09

4.1.1 Element Properties

Two different element types were suitable for comparison in the analysis. The different elements are plane solid (axisymmetric) and brick (volume) elements and will be referred to as AXIS and SOLID, respectively, in the analysis. The brick element is an 8-node solid element with constant stress. The

properties for the plane element are given in LS-DYNA with the following choices.

- Axisymmetric solid about y-axis. Loads, lumped masses, discrete element stiffness, etc. are interpreted as values per unit radian, *ELFORM=15*.
- Gauss integration rule by default, with 3 nodal points through thickness, *NIP=3*.
- Lagrangian 2D solid element type, default when selecting elform 15.

When modeling a fracture in a specimen, it has been shown that the material parameters are highly dependent on the mesh dimensions (de Borst, 2004). As mentioned previously, the full scale component test will be modeled in brick (volume) elements. Modeling with such elements is computationally expensive and refining of mesh will therefore increase the calculation time drastically. Consequently, the dimensions of the pipe-fittings decide the minimum dimensions of the elements. The dimensions of the elements must be able to describe the deformation of the pipe-fittings, but still within an acceptable calculation time. This implies that these rather coarse dimensions must be applied in the calibration of the material model, from now on referred to as coarse mesh. The elements have an edge length of 0.5 mm. Normally one would refine mesh until convergence of material parameters are obtained, instead a model with finer mesh will be used parallel to verify simulations and show the sensitivity of mesh discretization. The fine mesh models will not be shown in the report but results are to be found in appendix B.

4.1.2 Finite Element Analysis

The finite element code LS-DYNA is based on an explicit solver applied in this thesis. The solver is conditionally stable which results in having a critical time step (Cook et al., 2002).

$$\Delta t_{cr} \leq \frac{L_e}{c_d} = \frac{L_e}{\sqrt{E/\rho}} \tag{4.1}$$

where the critical time step is dependent on the smallest and stiffest element. L_e is the smallest length between nodes within an element in the model. c_d is the dilatational wave speed, i.e the speed of sound in the material. This results in a critical time step of $\sim 1.0 \cdot 10^{-7}$s, where $L_e = 0.5$mm. Since

the calculations are considered quasi-static, scaling the time or density can reduce the computational cost. It is chosen to scale with respect to the mass to increase the critical time step. Consequently an energy check must be done in order to verify that dynamic effects during the simulations are kept neglectable. The ratio between static load, F_s, and dynamic load, F_d, should be kept close to 1 and can, according to Reyes (2002), be approximated as:

$$\frac{F_s}{F_d} = L(t) \approx \frac{\Delta E_i}{\Delta E_i + \Delta E_k} \tag{4.2}$$

Where ΔE_i and ΔE_k is the change in internal and kinetic energy respectively.

4.2 Tensile Tests

The geometry of the tensile test specimen is axisymmetric, we can then use plane solid and brick solid elements in the discretization. The specimen has three orthogonal symmetry planes that could be used to reduce calculation time in the simulations. However, by modeling the specimen with symmetric boundary conditions we assume a symmetric fracture evolution, thus the energy required to initiate a crack is overestimated. To be able to calibrate the fracture criterion, the specimens are therefore simulated with their original geometry.

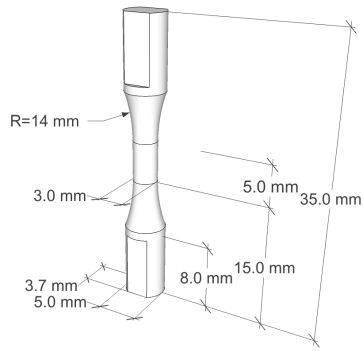

Figure 4.1: *Geometry of axisymmetric smooth tensile specimen*

To validate the results, three different analysis are carried out for the different σ-phase levels in the specimens. The simulations are performed by two different plane solid elements and one brick solid element. Due to increased calculation time when using brick solid elements in this analysis, the optimizations are only performed on the plane solid elements. The optimized material parameters are then used in the brick element model. A comparison between the plane- and brick element model is performed to validate this approach. The discretization of the models with coarse- and fine axisymmetric mesh are given with its symmetry properties in figure 4.2 and 4.3. The brick solid element model has approximately the same plane dimensions as the coarse plane solid element model. All dimensions and corresponding mass scaling factors are given in table 4.2.

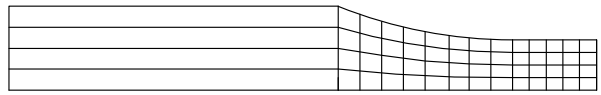

Figure 4.2: *Discretization of coarse mesh*

Table 4.2: *Different discretization models*

Discretization	Radial number of elements	Total number of elements	Min. element size	Mass scaling
Axiscoarse	4	128	0.1875 mm^2/rad	10^{10}
Axisfine	11	990	0.0283 mm^2/rad	10^{10}
Solidcoarse	4	1914	0.075 mm^3	10^{10}

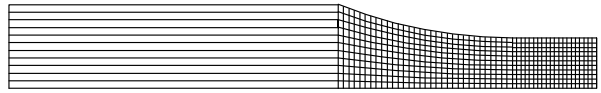

Figure 4.3: *Discretization of fine mesh*

4.2.1 Optimization

To calibrate the hardening parameters in the Gurson material model; in this case Voce hardening parameters, initial yield stress and initial void volume, a program called LS-OPT is used. This optimization program uses LS-DYNA's solver for the simulation. To calibrate, the user have to provide a target curve, define a response curve from the simulation, define range and initial value for the variables, and the level of accuracy by i number of iterations. Put shortly, LS-OPT guesses the first value for every variable, sends the job to LS-DYNA and retrieve the response curve. On the basis of calculations between the target- and response curve, the next values are guessed. For every iteration, the range for the variables is narrowed and the optimization converges. The result is a confidence interval for every variable with 95 % certainty.

During the optimization of the variables, LS-OPT calculates the mean square error for the deviation from the target- and response curve for every iteration. Between iterations, the program calculates the relations between every variables through Monte Carlo simulations, and the relation is weighted in a meta model. Based on the simulations it is build a response surface between the n number of variables. The calibrations converges if and only if a minimum in the response surface is found, therefore the range (Sub region boundaries) has to be wide enough to find the global minima and narrow enough to avoid numerical instability. If the minimum point for a variable is outside the sub-region boundary, the variable is held at the boundary value. This may cause an incorrect convergence for the other variables.

Table 4.3: *Input variables baseline model obtained from the thesis of Austnes and Bjørklid (2010)*

	σ_0 [MPa]	Q_1 [MPa]	θ_1 [-]	Q_2 [MPa]	θ_2 [-]
$\sigma_{\sim 0 vol.\%}$	478	618	2186	115	24890
$\sigma_{1-5 vol.\%}$	563	408	1087	228	3477
$\sigma_{\sim 10 vol.\%}$	541	411	2362	182	47052

As previously mentioned, the variables chosen to be calibrated in the Gurson material model are listed below, with initial values given in table 4.3.

- Initial yield stress, σ_0
- Voce hardening parameters; Q_1, Q_2, θ_1 and θ_2

- Initial void volume, ω_0

For the different σ- phases the variables differ, except the initial value of ω_0 that is set to 1.0E-6 as input for all optimization procedures. The material parameters listed in the table 4.3 are the optimized values given the thesis Austnes and Bjørklid (2010). In general, to create a response surface, LS-OPT needs 3-5 iterative simulations to build a response surface. To get really good convergence it is recommended to use at least 10 iterations. Therefore it has been chosen to use 15 iterations, to ensure optimized results.

Table 4.4: *Optimized material parameters from LS-OPT*

	$\sigma-$phase $[vol.\%]$	σ_0 [MPa]	ω_0 $[vol.\%]$	Q_1 [MPa]	θ_1 [-]	Q_2 [MPa]	θ_2 [-]
	~ 0	489	1.20E-03	720	2196	103	40197
AC	$1-5$	527	1.52E-03	577	2474	105	18676
	~ 10	524	2.91E-04	454	2328	204	28356

In table 4.4 optimized results from LS-OPT are given. For full details see Appendix A. In the appendix the confidence interval and plots of the sub-region boundaries for every parameter are given. Initially, it was expected that the initial void volume would increase as σ-phase content increased. This is only seen for σ-phase content from ~ 0 to $1-5$, but a clear reduction when σ- phase increases to $\sim$10. This could be explained by the reduction in plastic strain in the tests with $\sim$10 σ- phase levels, of about 40 %.

By examining the sub region boundaries in Appendix A, it is clear that almost all parameters have converged already at iteration 10. But at σ-phase 10, yield stress and hardening parameter θ_2 have some difficulty converging.

Figure 4.4 shows the response curve with optimized material parameters and the target curve from the laboratory.

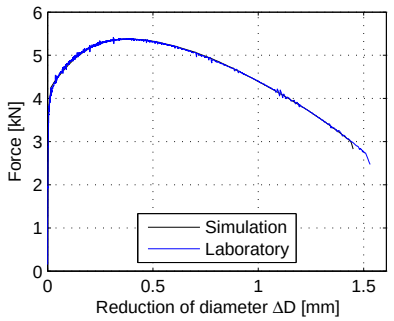

(a) Opt. 2D plane mesh, $\sigma \sim 0$

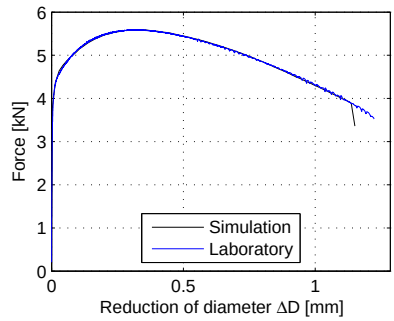

(b) Opt. 2D plane mesh, $\sigma 1 - 5$

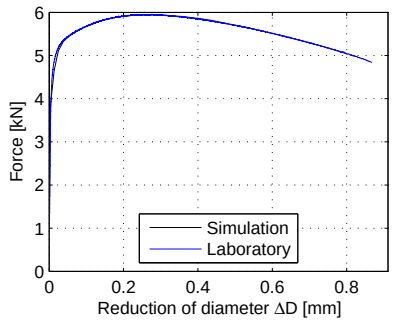

(c) Opt. 2D plane mesh, $\sigma \sim 10$

Figure 4.4: *Response curve for material values optimized for 2D plane coarse mesh, compared to laboratory target curve*

The figure above, figure 4.4, are in very good agreement with the target curve for all the σ-phase levels. In addition to calibrate the material parameters in LS-OPT, the critical void volume fraction, ω_{cr} has been determined. This has been done by extracting the void volume throughout the simulation and at the fracture strain from the laboratory, the critical void volume fraction has been noted. Then the simulations have been re-run with the given critical void volume fraction seen in the figure above. When an element reaches this critical value, the element is eroded from the simulation. The critical void volume fraction is given in table 4.4.

To be able to further compare the difference between the target- and response curve, some key values both from the laboratory tests and the simulations has been written in table 4.5 and 4.6. These values are

- Max. F: Maximum force
- σ_u: Ultimate true stress
- ε_{cr}: Failure logarithmic strain
- ω_{cr}: Critical void volume fraction
- Π: Total strain energy
- $\Delta\sigma$: Deviation between laboratory σ_u and simulated σ_u
- ΔF: Deviation between laboratory maximum force and simulated maximum force

Table 4.5: *Results from optimized AC material parameters, with different σ- phase content*

		σ_u [MPa]	ε_{cr} [mm/mm]	ω_{cr} *vol.*%	Π [J/mm^3]	$\Delta\sigma$ [MPa]	ΔF [N]
AC	$\sigma_{\sim 0\%}$	1570	1.32	2.22E-01	1647	15	34
	$\sigma_{1-5\%}$	1426	0.97	9.63E-02	1110	20	4
	$\sigma_{\sim 10\%}$	1326	0.62	5.61E-03	678	26	5

When comparing key values between the two tables, the largest deviation is the failure strain in $\sigma \sim 10$, about 8 %. Which in turn explains the drop in total strain energy, proximately 10 %. This is because the plotted response curve is cut at the time step when an element is deleted, due to the critical void volume fraction. This is a little early compared to the target curve from the laboratory. The result are still considered accurate, and will be used further.

Table 4.6: *Key values from laboratory target curve, with different σ- phase content*

		σ_u [MPa]	ε_{cr} [mm/mm]	Π [J/mm^3]	Max. F [kN]
Lab	$\sigma_{\sim 0\%}$	1585.6	1.40	1771.0	5.42
	$\sigma_{1-5\%}$	1446.1	1.03	1200.4	5.60
	$\sigma_{\sim 10\%}$	1352.6	0.67	744.7	5.96

Optimized Material Parameters for 2D Plane Coarse Mesh with 3D Brick Coarse Mesh Model

By using the material parameters optimized for the plane coarse mesh in the brick coarse mesh, the response curve should be somewhat similar. The result of this method is given in the figure 4.5 below. The same target curve from the laboratory tests used in the optimizations process is plotted on top of the response curve from simulations.

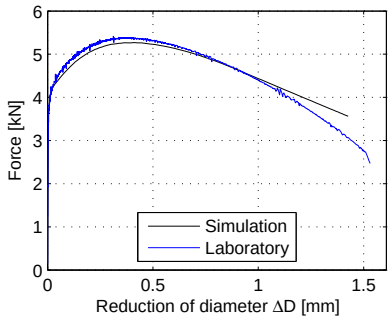

(a) 3D brick mesh, $\sigma \sim 0$

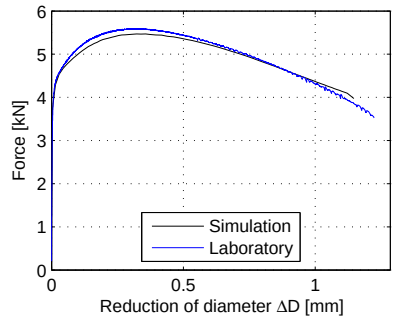

(b) 3D brick mesh, $\sigma 1 - 5$

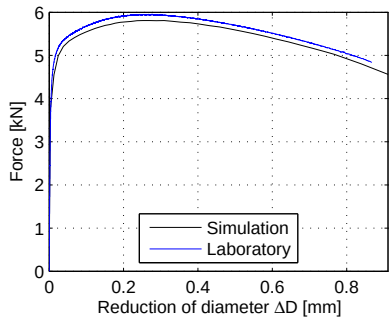

(c) 3D brick mesh, $\sigma \sim 10$

Figure 4.5: *3D brick response curve with optimized material values from 2D plane mesh, compared to laboratory target curve*

The trend for all analysis in the figure above, are that they undershoots maximum force. For large strains, they do not describe the behavior seen in the laboratory. For $\sigma \sim 10$ the results are very good, but the force is constantly below the target curve. Since this tensile test do not have as large plastic strains as the other tests, it is easier to get a more correct response.

In the table 4.7 above, is the same key values as seen before. Again, the

Table 4.7: *Key values for 3D brick element coarse mesh, with optimized 2D plane element coarse mesh material parameters*

		σ_u [MPa]	ε_{cr} [mm/mm]	ω_{cr} *vol.*%	Π [J/mm^3]	$\Delta\sigma$ [MPa]	ΔF [N]
SC	$\sigma_{\sim 0\%}$	1940	1.32	$1.23e-02$	1753	354	147
	$\sigma_{1-5\%}$	1551	0.98	$9.67e-03$	1169	105	124
	$\sigma_{\sim 10\%}$	1435	0.88	$1.10e-03$	1049	83	147

$\sigma \sim 10$ simulations have very good results, with logarithmic failure strain being identical to the strain in the laboratory. But the other tests are way off, $\sigma \sim 0$ has a deviation in maximum true stress above 20 %.

As seen for all previous simulations, that critical void volume at failure is decreasing as the σ-phase content increases. The expected results would be the exact opposite. This is because of the growth in void volume fractions is strongly related to the plastic straining. Put simply, the specimens in the more ductile material, i.e. $\sigma \sim 0$ and σ 1-5, are exposed to more plastic straining and therefore the growth in void volume fraction is higher. This also indicates that the effect of the Gurson model is limited for the specimens containing $\sim$10 σ-phase.

As a consequence for these poor results, when using optimized material parameters from plane course mesh model with brick coarse mesh model, makes it is necessary to do the same optimization procedure on the brick coarse mesh model for all σ-phase levels.

Optimizing Material Parameters for 3D Brick Coarse Mesh Model

The initial plan is to only optimize for the coarse 2D plane solid element model (AC), since this element model is not so computational expensive. After calibrating the material parameters, and running the parameters in the 3D brick solid model(SC), the obtained response curve were not satisfying. Therefore a optimization scheme is done also for the 3D solid coarse mesh as well. This gives the results given in table 4.8. For more detailed results see Appendix A.

Table 4.8: *Optimized material parameters from LS-OPT for 3D brick coarse mesh model*

	$\sigma-$phase [*vol.*%]	σ_0 [MPa]	ω_0 [*vol.*%]	Q_1 [MPa]	θ_1 [-]	Q_2 [MPa]	θ_2 [-]
SC	~ 0	500	5.43E-04	582	2000	154	50000
	$1-5$	535	6.28E-04	458	2033	171	50000
	~ 10	560	9.67E-05	360	1733	239	55000

The table above shows an increase in yield stress for increasing σ-phase. For all calibrations a decrease in initial void volume fraction is observed. More worryingly, many of the hardening parameters do not converge properly within the pre-described 15 iterations. Especially θ_1 and θ_2, giving an confidence interval of $+/-$ infinity and the same is for Q_1 at $\sigma_{\sim 0}$ and $\sigma_{\sim 10}$. Even when the sub-region boundaries narrows down for these parameters.

When comparing key values from table 4.6 with 4.9, the results are very good. The total deviation in strain energy varies between 3 % and up to 5 % and failure strain between 4.5 % and 6 %, which is much better than the previous result. And likewise the maximum force and ultimate stress is below 1 % of their target value.

However the non-physical high value of critical void volume fraction in $\sigma_{\sim 0}$ of 25 vol.%, can be explained by the large straining of elements in the necking area. When using such a coarse mesh used in this model, the elements in the necking region get strains up to 300 %, and since the development of void volume is highly correlated to equivalent plastic strain and triaxiality, we get non-physical values for plastic strain of the elements, consequently the value for critical void volume increases.

Table 4.9: *Optimized results from numerical quasi-static tensile test with 3D brick coarse mesh*

		σ_u [MPa]	ε_{cr} [mm/mm]	ω_{cr} *vol.%*	Π [J/mm^3]	$\Delta\sigma$ [MPa]	ΔF [N]
SC	$\sigma_{\sim 0\%}$	1576	1.31	2.58E-01	1657	10	32
	$\sigma_{1-5\%}$	1445	1.00	1.37E-01	1189	1	16
	$\sigma_{\sim 10\%}$	1336	0.60	5.15E-03	671	17	26

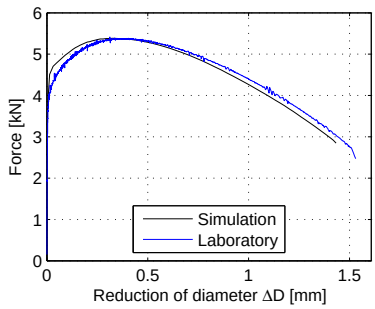

(a) σ-phase ~ 0

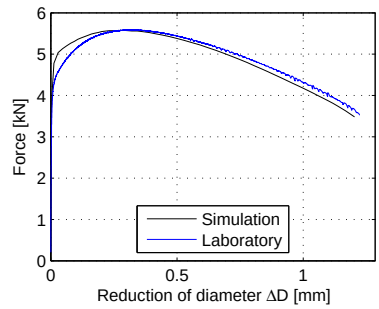

(b) σ-phase $1-5$

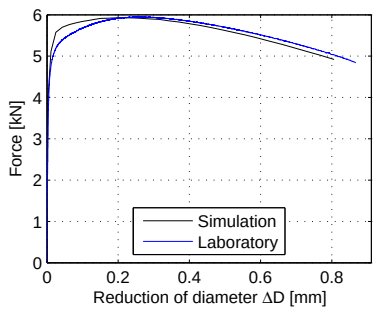

(c) σ-phase ~ 10

Figure 4.6: *Response curve from material parameters optimized for 3D brick solid coarse mesh, compared to laboratory target curve with different σ-phase content*

Figure 4.6 and 4.7 show the simulated optimized response curve with the laboratory target curve. In the force-displacement curve, the simulations seem to overestimate the force at yielding. The curve continuous by following the target curve with a slight negative offset. This is also seen in the stress-strain plot, an overestimation in the lower strain region, then for the larger

strains stresses are somewhat smaller.

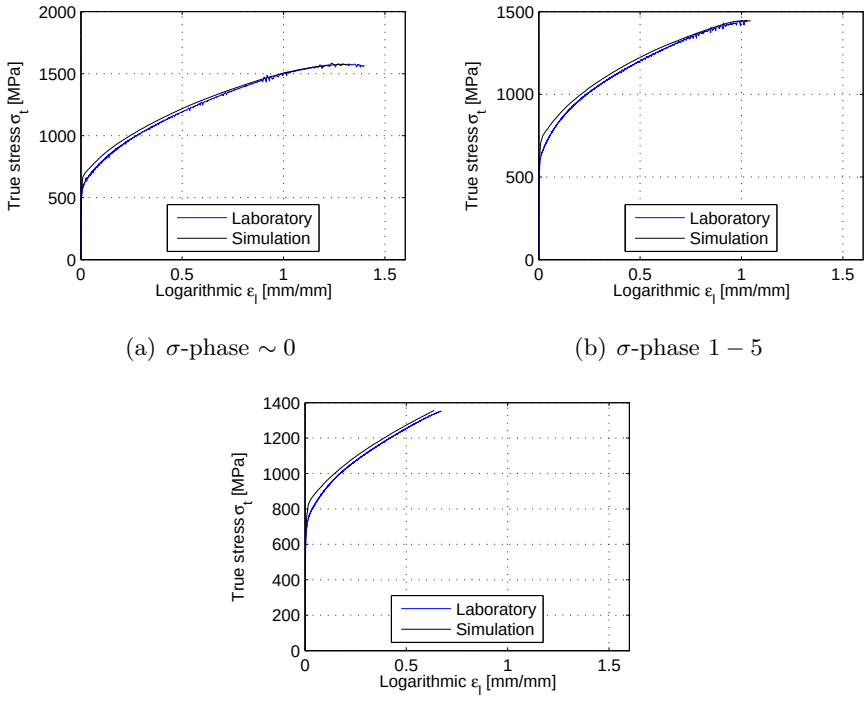

(a) σ-phase ~ 0

(b) σ-phase $1 - 5$

(c) σ-phase ~ 10

Figure 4.7: *True stress-logarithmic strain relations for material parameters optimized for 3D brick solid coarse mesh, with different σ-phase content*

Even though some inaccuracies are observed, it is chosen to use the obtained material for further studies. Since the hardening parameters do not converge, this is possible source of error in the simulations to come. It is important to have this in mind when interpreting results.

4.2.2 Discussion of Results

The mesh dimensions and mass scaling factors are studied to control the simulations and make them as efficient as possible. The different simulations of the various σ-phase levels are compared to the corresponding lab results. The mass scale factor shown in table 4.2 are controlled for dynamic influence according to equation 4.2 and plotted in figure 4.8. The initial relation between the dynamic- and static forces are approximately 1‰ and is therefore negligible. The dynamic influence seen late in the simulation is due to eroding elements, then forces is relocated to surrounding elements, creating dynamic effects.

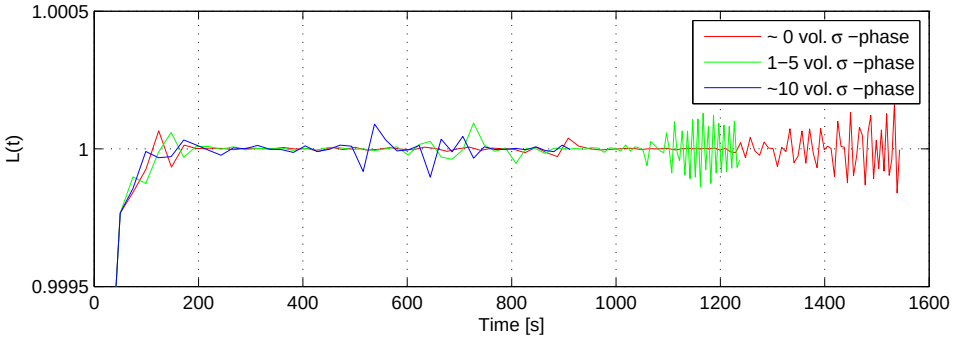

Figure 4.8: *Control of dynamic effects from mass scaling*

When optimizing the material parameters in LS-OPT, it is experienced that the initial input values are crucial to obtain the correct solutions. The optimization for each of the specimens has been done several times with different input values and varying initial sub-region boundaries. The results show a highly dependency on these input parameters. This implies that the user must be able to do an educated ”guess” on these input values in a range not too far from the correct value. The results from the optimization process can at first seem to be in good agreement with the target curve from the laboratory. However, a closer study shows that these material parameters are not necessarily valid for all cases. This can be explained by the occurrence of local minima in the surface build by LS-OPT during optimization. Thus, the solutions for the optimized material parameters are not unique. When combining this with the coarse mesh, it becomes very difficult to distinguish the origin of the errors. Further investigation of the optimized results, show

that the initial void volume fraction has a strong covariance to the other material parameters, i.e. the other parameters are highly dependent on this parameter. To eliminate some of the problems, it is recommended to determine the void volume fraction in other ways. Previous studies have managed to do this on dual phase steel (Avramovic-Cingara et al., 2009), and for further research this is recommended. Another ambiguous result is the material parameters obtained. It would be reasonable to presume that the optimized parameters obtained in with AC model, should be able to describe the SC model. This correlation between the material parameters and element types is not observed in this material model, and should be investigated in further work.

To be able to describe necking with the coarse mesh has shown to be unfortunate, and a massive source of error. The elements in the necking region, get strains up to 300 %, these strains are not observed in the laboratory. The coarse mesh used in the model causes an unrealistic deformation of the elements to be able to describe the physical deformations occurring after necking. Even with the finer (AF) mesh discretization, the same problems occurred with plastic strain being non-physically large. The proper solution would be to ensure a refinement of the mesh to the extent where necking is properly described. To obtain this behavior in the mesh, the elements should be modeled as rectangular elements, such that the deformed element at the onset of necking has a quadratic form. For these test specimens it requires a discretization where there are approximately 40-50 elements over the diameter for a smooth axisymmetric specimen, like the one used in this tensile test. This gives the required dimensions in our case of 0.075 mm in radial direction and 0.0375 mm in longitudinal direction.

To confirm this, a different specimen with the mentioned discretization of mesh has been used with the modified Gurson material model. The material values are equal to optimized SC $\sigma_{10vol.\%}$ and at the last time-step before global failure a contour plot of equivalent plastic strains have been plotted in figure 4.9. The computational time drastically increases when using this mesh compared to the coarse mesh. An approximate estimation, suggests an increased factor of 74 in total calculation time for every simulation. The optimization scheme would then take approximately 7-10 days, when running all sub incremental simulations simultaneously on an equivalent computer used in this thesis.

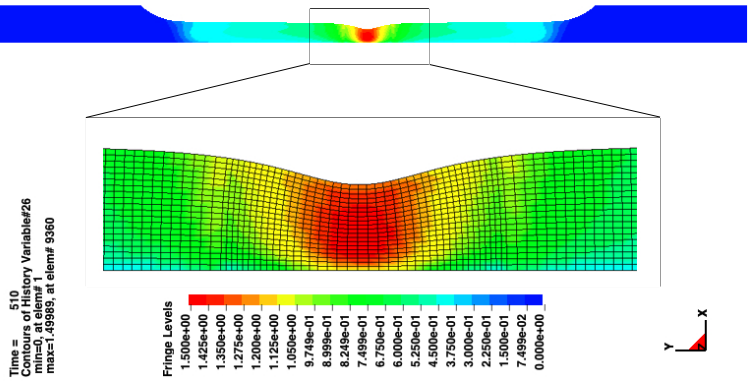

Figure 4.9: *Properly refined mesh for describing necking in an axisymmetric smooth tensile test specimen*

The material model used in this thesis is a new implementation of the modified Gurson material model in SIMLab Metal Model. It was not clear whether this material model would work or not prior to this thesis. It has, to some extent been verified by the semester report by Øien. However, quite a few errors and faults have been detected during the simulations. Consequently, the material model has been updated on regular basis throughout the thesis where minor- and major faults have been fixed. The result being that simulations have been run several times, including the optimization of the material parameters. This has lead to some ambiguous results, which has been very challenging when interpreting the results from the simulations.

Figure 4.10 show two different stress strain curves done on the exact same specimen, with same baseline of material parameter. Performing the exact same optimization with two different solvers, we observe a completely different result.

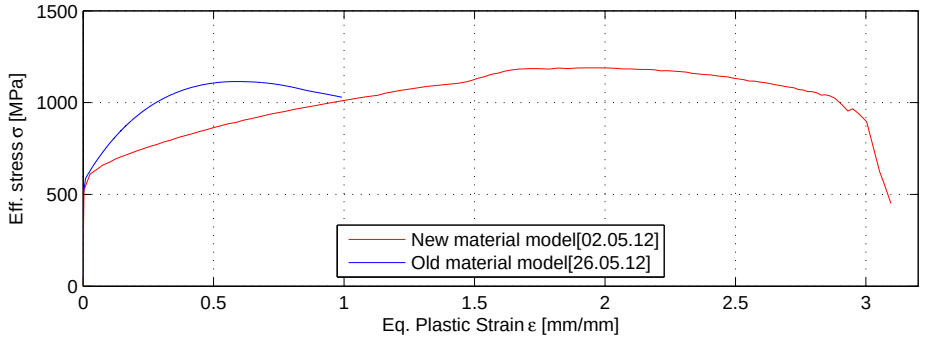

Figure 4.10: *Comparing stress-strain relation difference using old and new SIMLab Metal Model solver*

As seen in the figure above, figure 4.10, the change in plastic strain is extensive. Comparing equivalent plastic strain from the old with the new SIMLab Metal Model, gives an increase of plastic strain of a factor 3.5. It is clear, after thoroughly investigating the plastic strain, that the latter solution is the more correct one when using coarse mesh. The deformation seen in both analyses are identical, but the reason for the deviation in plastic strain has not yet been found.

As a concluding remark to this section, it is seen that the Gurson model has a limited effect on the brittle specimens, i.e. specimens containing $\sim$10 σ-phase. This could indicate that the Gurson model is probably not necessary to describe this problem.

4.3 CTOD Fracture Toughness Tests

This section contains the simulations of the crack-tip opening displacement (CTOD) with the optimized values from the tensile tests. The simulations are performed to verify the results obtained in the tensile tests. A previous attempt to simulate the full scale component test mentioned in section 2.4 (Austnes and Bjørklid, 2010) have shown that is difficult to capture the transition between the ductile and brittle fracture. The specimens containing a large amount of σ-phase ($> 8.vol\%$) shows this ductile-brittle fracture pattern, and it is therefore expected that these test specimens will behave too ductile. Thus it requires an additional criterion, namely the maximum stress given in section 3.2 to be able to describe these tests.

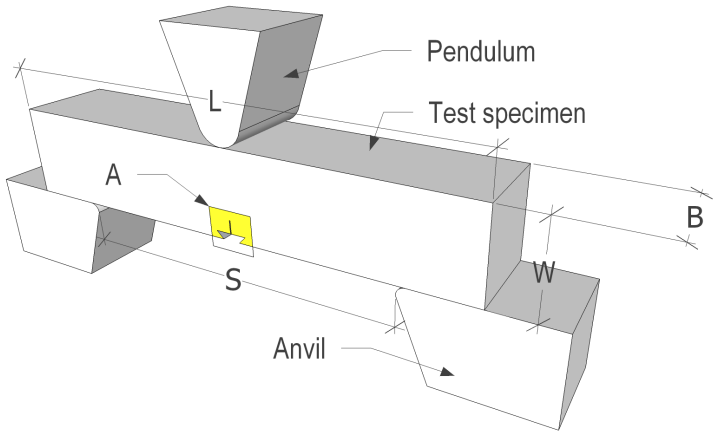

Figure 4.11: *Test set-up for the CTOD fracture toughness test*

Simplified, the CTOD test shown in figure 4.11 can be explained as a three point bending procedure. That is, the pendulum presses the specimen at a constant strain rate (sufficiently slow to be considered quasi-static) until maximum load is reached, then the specimen is unloaded. The scope of the test is to find the force needed to ”open” the specimen, i.e. the measured displacement, CMOD, in the critical section shown in figure 4.12 and 4.13.

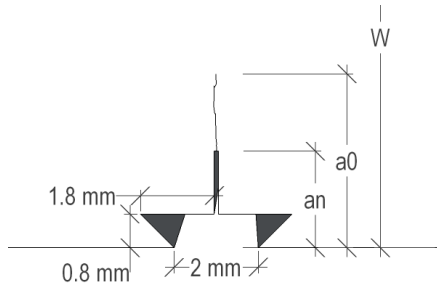

Figure 4.12: *Detail A from figure 4.11, showing the spark eroded notch with pre-stressed fatigue crack*

Figure 4.13: *Deformed test specimen at detail A in figure 4.11, showing crack mouth opening displacement (CMOD)*

4.3.1 Discretization

The numerical test set-up contains three parts; The anvil, pendulum and specimen shown in figure 4.11. Both the anvil and the pendulum are modeled with 2D plane elements extruded 15 mm. The specimen is modeled with 8-node 3D solid elements, with the same coarse mesh size as in the tensile test, 0.5 mm along edges. Only a quarter of the specimen is modeled due to the symmetry planes. Thus the computational cost is considerably reduced and only one half of the pendulum and one anvil are therefore necessary. Both the anvil and the pendulum are rigid bodies, and the specimen is constrained in the perpendicular direction of the symmetry planes. At the midspan of the test specimens are modeled with an effective cross-sectional height given as

$$h_0 = W - a_n \tag{4.3}$$

Thus, the symmetric cross-sectional area at the midspan, given as $A_{eff} = h_0 B/2$, is constrained to translate in the longitudinal direction of the test specimen.

As mentioned in section 2.3, the tests where only performed at -10 °C. Since the material parameters are calibrated for isothermal conditions this is a plausible source of error. However, a drop in temperature in this order of magnitude ($\Delta K = 30$) will only change the material behavior in a slightly stiffer manner. The effect of change in temperature is therefore neglected.

Nine different specimens are tested in the longitudinal direction through three series with 0 %, 5 % and 10 % vol. fraction precipitated σ-phase. Longitudinal test with 0 % vol. σ-phase specimen 1 (L0-1), have been excluded for comparing since the clip gauge hit the anvil and therefore the measured CMOD can not be used.

Table 4.10: *Geometry of single edge notched specimens (SENB)*

σ-phase [vol. %]	Test id [#]	W [mm]	B [mm]	a_0 [mm]	a_n [mm]
∼0	0-2	6.64	6.88	3.14	1.88
	0-3	6.62	6.97	3.09	1.80
1-5	5-1	6.99	6.91	3.22	1.93
	5-2	6.71	6.90	2.90	1.92
	5-3	6.49	6.91	2.95	1.88
∼10	10-1	5.03	4.97	2.26	1.47
	10-2	4.87	4.96	2.05	1.35
	10-3	4.84	4.94	1.78	1.41

All test specimens have been modeled with their exact geometry listed in table 4.10. Where B is the width, W is the height and a_n[1] is the dimension from the bottom of the specimen to the end of the notch. The initial crack length a_0 is the initial crack length including pre-stressed fatigue crack and is measured by n equally spaced points and averaged as (Minnebruggen et al., 2011)

[1]These dimensions are not available from any previous tests. The dimensions are therefore calculated by measuring lengths in the pictures from Lange and Hassel (2010) and using the relation between known dimensions and the relative dimensions in the picture, i.e a possible source of error.

$$a_0 = \frac{1}{i-1}\left[\frac{a_1 + a_i}{2} + \sum_{k=2}^{i-1} a_k\right] \tag{4.4}$$

4.3.2 Contact Formulations

Previous attempts to simulate the CTOD have shown that the choice of contact formulation is essential. Therefore, several built-in contact formulations from LS-DYNA have been used in these calculations:

- *CONTACT_AUTOMATIC_SURFACE_TO_SURFACE
- *CONTACT_ERODING_SURFACE_TO_SURFACE
- *CONTACT_SURFACE_TO_SURFACE

The most common explicit constraints are the Lagrange multipliers and penalty functions. The latter algorithm is used in the formulations above. The penalty method is often preferable to the Lagrange multiplier because it neither increases the total number of unknowns nor destroys the positive definiteness of the equation system. The main disadvantage is appearance of ill-conditioned set of equations may occur, in addition it may alter the topology of the stiffness matrix which makes the equation solving cumbersome. The constraint equations that relate d.o.f in $\{D\}$ can be written in the form

$$[C]\{D\} - \{Q\} = \{t\} \tag{4.5}$$

so that $\{t\} = 0$ defines satisfaction of the constraints. $[C]$ and $\{Q\}$ contain the constraint constants. The penalty method introduces a diagonal matrix $\lceil\alpha\rfloor$ which can be interpreted as a "spring-stiffness", meaning that the algorithm allows some penetration of the contact surfaces such that the constraints in eq. 4.5 are more nearly satisfied. The penalty function can be implemented by augmenting the constraint $\frac{1}{2}\{t\}^T\lceil\alpha\rfloor\{t\}$ in the potential energy function and make it stationary, thus the expression for the implemented constraint yields

$$\left([K] + [C]^T\lceil\alpha\rfloor[C]\right)\{D\} = \{R\} + [C]^T\lceil\alpha\rfloor\{Q\} \tag{4.6}$$

It can readily be seen as $\lceil\alpha\rfloor$ approaches zero that the constraints are ignored, i.e. the expression is reduced to its origin. Thus the value of $\lceil\alpha\rfloor$

must be chosen appropriately such that it is large enough to be effective but not so large as to provoke numerical error. LS-DYNA chooses this value approximately in the order of magnitude as the stiffness of the interfacial elements normal to the interface. This results in an unaffected critical time step as calculated in equation 4.1. However, if the penetration becomes unacceptably large, one can increase the "spring-stiffness" and with that decrease the critical time step. Be aware of the ill-conditioning that may occur due this manual editing.

In the CTOD tests there are two different contact formulations. The anvil/test specimen and the pendulum/test specimen. To obtain a better contact surface the mesh of the anvil and the pendulum are refined. The test specimen is defined as the master segment, hence the anvil and the pendulum are defined as slave segments. This means that the test specimen is to some extent allowed to penetrate the specimen, but not the other way around.

Even though a previous thesis (Kalstad and Nord, 2011) has experienced problems with contact formulations, it is only observed minor differences between the contact formulations. The AUTOMATIC_SURFACE_TO_SURFACE formulation gives the smallest amount of sliding energy, and is therefore applied in further calculations. The most decisive change is caused by the master/slave formulation. The opposite formulation gives a "hammock" effect, i.e. the nodes in the test specimen are hooked to the nodes in the anvil giving spurious stiffness to the specimen. In addition, the elements are fully integrated, to reduce the artificial energy occurring when using hourglass control.

4.3.3 Numerical Results

When simulating the test specimens it becomes clear that the effective height defined in equation 4.3 overestimates the forces in the specimen. Thus it is chosen to do a study on how the effective height h_0 influences the response of the specimens. The different tests vary in lab-force levels, this is mainly caused by different geometries in the test specimens. It is chosen to study the effect of the efficient height on one specimen for each level of σ-phase content(L0-3, L5-1 and L10-1).

To validate the assumption of quasi-static loading the dynamic influence according to equation 4.2 is calculated an plotted in figure 4.14. The dotted lines show the maximum deviation recommended to be classified as a quasi-static loading.

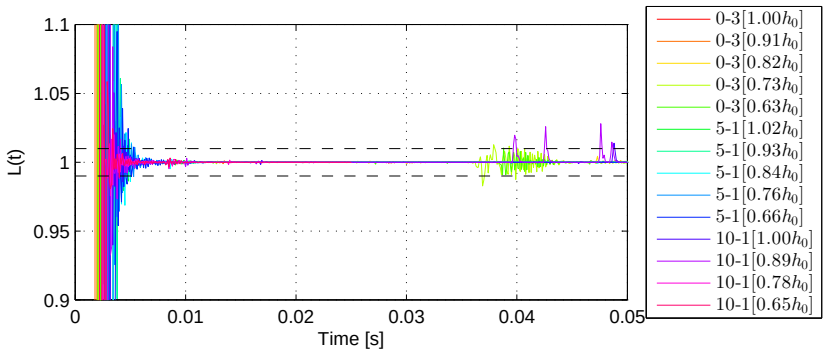

Figure 4.14: *Dynamic influence in all simulations*

Initially, a substantial dynamic influence is observed when the pendulum hits the test specimens. In an attempt to minimize the dynamic "shock-wave", the velocity of the pendulum is gradually increased over a time period of 0.025 s, and the time scaling factor is reduced to approximately 10^{-4}. Unfortunately, the dynamic effect is still present. However, since the dynamic influence is narrowed within the accepted levels further in the analysis, it can be classified as quasi-static in this region. When the first elements are eroded the effect increases again. Since the main interest is the crack initiation, some dynamic influence beyond this point is accepted.

Figure 4.15 shows the response of the test specimens with varying heights for ~ 0 *vol.*% σ-phase content. The test specimen simulated with expected effective height, given in equation 4.3, overestimates the stiffness. This is the trend for all the simulated test specimens as shown in appendix D.

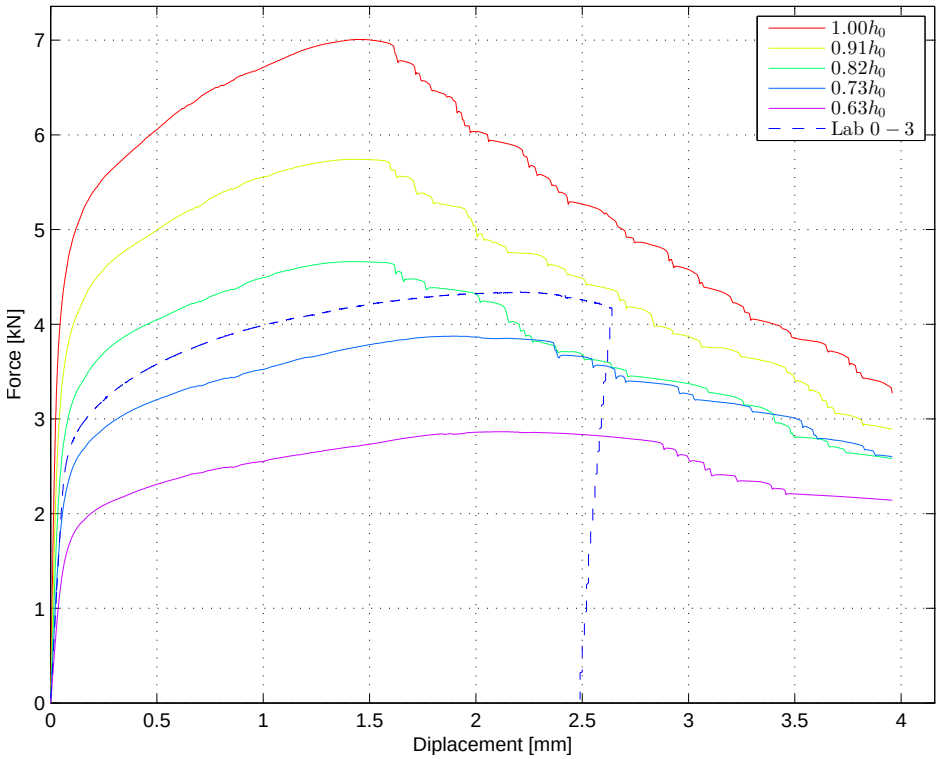

Figure 4.15: *CTOD tested with varying effective heights, ~0 vol% σ-phase*

When the loads in figure 4.15 reaches its maximum, the first elements are eroded. The simulations overestimating the stiffness and force levels ($1.00h_0$, $0.91h_0$ and $0.82h_0$) initiate the eroding of elements prematurely. A possible source of error is the coarse mesh overestimating the plastic strains to be able to describe the large deformations. Thus the growth in void volume fraction accelerates in a corresponding manner. Consequently the elements reach their critical void volume fracture prematurely, i.e. the elements are eroded too early.

With increasing σ-phase content (1-5 *vol.*%), figure 4.16 shows the same trend as in figure 4.15. The main difference is the eroding of elements, which is initiated too early even for the effective heights underestimating the stiffness and force levels. The premature crack initiation for $\sim$0 σ, is most likely caused by the coarse mesh giving an increase in the plastic strains for large deformations. Apart from a somewhat more brittle behavior, the force levels are quite similar to the test specimen containing $\sim$0 σ-phase.

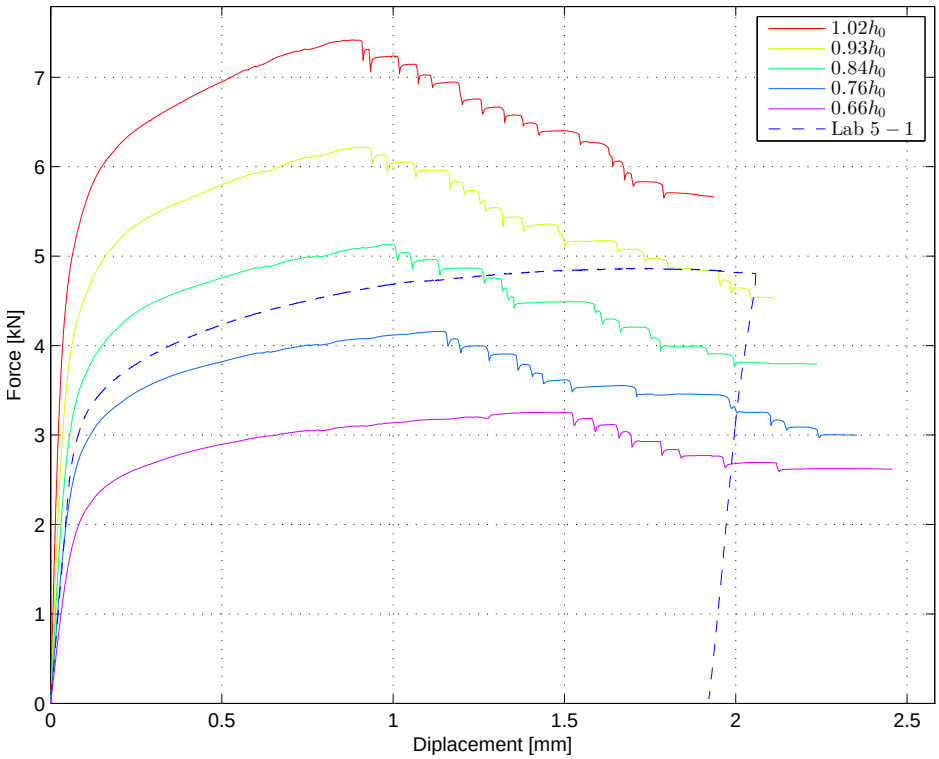

Figure 4.16: *CTOD tested with varying effective heights, 5 vol% σ-phase*

For test specimens containing σ-phase $\sim$ 10 *vol.*%, the overestimation of the stiffness and force levels for the expected effective height is still present. The response is plotted in figure 4.17. A more ductile response is observed independent of the effective height compared to the lab data. Additionally, it seems that the hardening parameters are incorrect, since the material continuous to harden throughout simulations. This could indicate that the fracture criterion obtained in the tensile test simulations in section 4.2, is not sufficient to describe the behavior of the material. The brittle fracture criterion, mentioned previously, given in equation 3.2 is therefore proposed to handle the deviation. The results are highly uncertain due to the lack of correspondence between the expected efficient height and simulated response. It is therefore chosen to pick a range of values for the maximum principle strain criterion. These values are "guessed" from the simulation ($0.78h_0$) who seems to describe the response in the best manner.

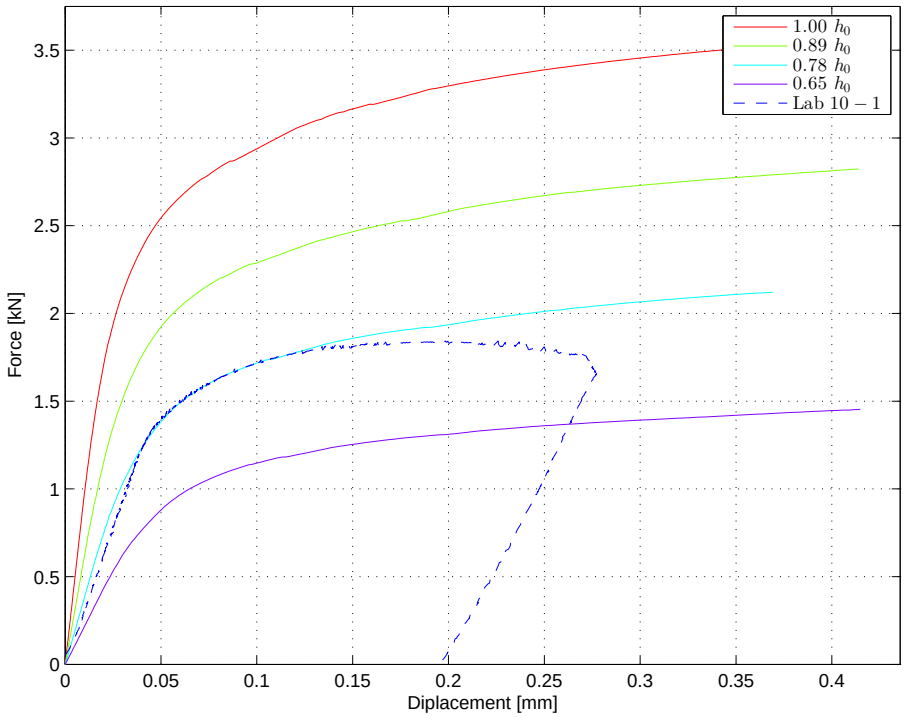

Figure 4.17: *CTOD tested with varying effective heights, 10 vol% σ-phase*

4.3.4 Discussion of Results

The main source of error in the CTOD simulations are the effective height. A possible explanation is the fatigue crack given by cyclic loading before the specimen was exposed to bending. The effect of the varying cross-sectional height has been plotted as a fraction of the initial effective height h_0 in figure 4.18 for a given displacement. The displacement corresponds to the maximum force from the lab-results.

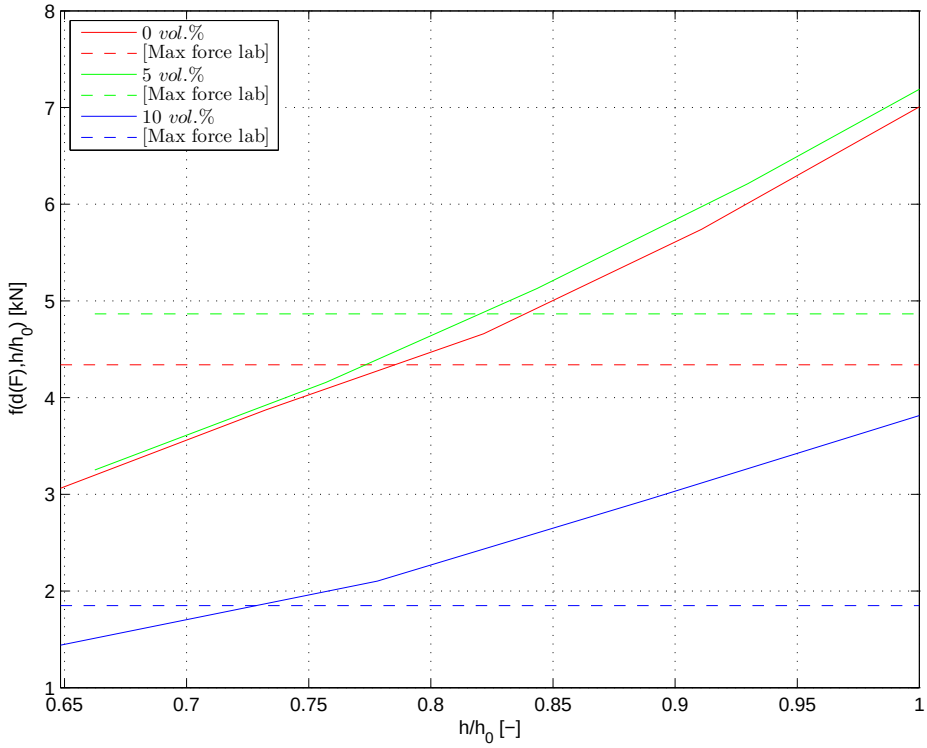

Figure 4.18: *Describes how the force-level, at a given displacement, vary with the effective height, h/h_0*

It can be seen that the "correct" effective height vary for the different levels of σ-phase content. A range between 0.73 $h_0 \rightarrow$ 0.83 h_0 is observed, indicating the fatigue crack to some extent has weakened the material. The weakening may come from macro cracks occurring under the cyclic fatigue loading process. When modeling problems like this, it is crucial to know such effects in the specimens to be able to describe its behavior.

Another source of error is the coarse mesh. In figure 4.19 the equivalent plastic strain is plotted for the specimens modeled with the expected efficient height($\sim$ 0- and 1-5 σ-phase). The strain levels are nearly doubled in order of magnitude compared to the logarithmic fracture strain predicted in the tensile test given in table 4.6. Thus the assumption of increased plastic straining due to the elements attempt to describe the large deformations, seems to be a reasonable explanation for the premature eroding of elements.

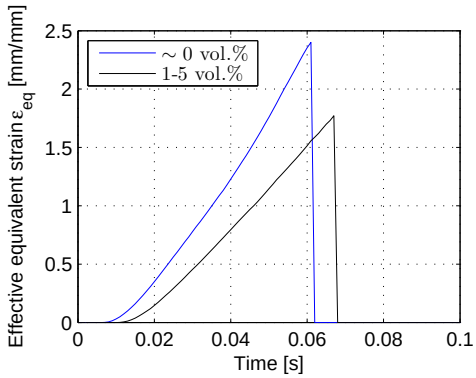

Figure 4.19: *Equivalent plastic strain in the first eroded element corresponding to its σ-phase content*

This section has shown that the CTOD tests are very hard to simulate. For further work it is strongly recommended to have exact measures for all data from the lab-results, knowing that the test is highly dependent on the geometry. In addition, it is advised to check the specimens exposed to fatigue loading by taking some samples and check them for macro cracks in the fatigued area.

For σ-phase levels of $\sim$ 0 vol.% and 1-5 vol.% the brittle fracture is considered unnecessary since the crack initiation for these levels initiate prematurely. Unfortunately, this implies the desired verification this test initially was intended to do, is not obtained.

The study of the effective height does not imply a single success criterion to determine the geometry of the cross-section. It is therefore chosen to extract a range of stress levels for the brittle fracture criterion for $\sim$ 10 vol.%. This range lies within 1350 [MPa] $\rightarrow$ 1400 [MPa]. These values reflect the maximum principle stress in the area corresponding to the maximum force in the lab-results.

5. Analytical Verification

This chapter contains the development of analytical approaches and its corresponding results obtained for verification of the thesis' results. Since the Gurson UMAT (user defined material model) implemented in the SIMLab Metal Model is considered an alpha version, it consequently can contain some errors. In order to verify the results obtained from the implemented material model, independent analytical approaches are developed. The analytical results are also meant to verify the results obtained in the simulations where suitable. To obtain equal premises for the analytical approach, some assumptions have been done, but the results are still considered valid for verification. The evolution of the void volume fraction has been calculated for one element and for the tensile tested specimens simulated with the UMAT. In addition the analytical necking has been compared to the necking extracted from the tensile-test data.

5.1 Analytical Void Volume Fraction

The theory behind the equations implemented in the computations has been thoroughly described in section 3.1. For the calculation of void volume fraction, a Matlab script from Christian Øien's semester project (Øien, 2011) is used with some modifications. The main idea behind the script is to express the void volume growth as a function exclusively depending on the equivalent macroscopic stress σ_{eq}, the microscopic stress σ_M and the triaxiality given as

$$\sigma^* = \frac{\sigma_H}{\sigma_{eq}} \tag{5.1}$$

The triaxiality is considered an interesting parameter when discussing ductile fracture because the peak of the triaxiality corresponds to the crack initiation for rounded notch bar specimens (Tamura et al., 2009). In the original Matlab script, a constant triaxiality through the calculation is assumed. Instead, a modification where we do a step-by-step integration with a constant

triaxiality within each strain increment has been performed. The void volume fraction growth is assumed only to be driven from growth of existing voids, i.e. nucleation and coalescence of voids are neglected. Based on these assumptions one can create a numerical calculation scheme, which can be explained in the pseudo code presented in the next section.

5.1.1 Pseudo code

- Define the material parameters for the Gurson model. That is, the Voce hardening parameters Q_i, θ_i, the initial void volume fraction ω_0 and the yield stress σ_0
- Prescribe the equivalent plastic strain array ε^p_{eq} until simulated failure strain
- Define an associated triaxiality array σ^*
- Set initial values for ε^P_M and $\Delta\lambda$. If the initial conditions is at the start of plastic straining, set the values to 0

Algorithm 1 Pseudo code for analytical void volume fraction calculation

for the prescribed equivalent plastic strain array **do**
- Define a plastic strain array within the increment with a satisfying strain resolution
- Calculate a corresponding mean triaxiality σ^*_n within the increment

for the plastic strain array within the incriment **do**
- Calculate σ_M from equation 3.20
- Set $\sigma_{eq} = \sigma_M$
- Calculate σ_{eq} by equating the yield function 3.7 to zero, using e.g Newton-Raphson iterations
- Calculate $\Delta\lambda^i$ by equation 3.17
- Calculate $\Delta\varepsilon^{i+1}_M$ by equation 3.19 and then $\varepsilon^{i+1}_M = \varepsilon^i_M + \Delta\varepsilon^{i+1}_M$
- Calculate the void volume growth $\Delta\omega$ by equation 3.26 and then $\omega^{i+1} = \omega^i + \Delta\omega^i$

end for
- Set $\omega_{n+1} = \omega^i_n$ where i represent the last sub-increment, and use this as the initial value for the next step
- Set $\varepsilon_{M,n+1} = \varepsilon^i_{M,n}$,where i represent the last sub-increment, and use this as the initial value for the next step

end for

In the original script there are several opportunities to calculate different values at the instability loci. The shear term from the extended Gurson model as mentioned in section 3.1.5 is also included in the original script. These opportunities and the additional shear term are not relevant in this thesis, and are therefore omitted in the *pseudo-code* above. For more in-depth studies of the expression in the pseudo code see appendix C.

5.1.2 Eight-node Element

To verify the modification, a comparison of the void volume growth with a single 8-node solid element is performed. The element has unit dimensions, i.e. 1x1x1, where one node is placed in the origin of the global coordinate system. It is strained from a prescribed displacement in the z-direction, given to the top set of nodes in the xy-plane. To ensure a constant strain rate the incremental displacement, ΔL, can be defined as

$$\varepsilon = \int_0^t \dot{\varepsilon} dt = \dot{\varepsilon}_0 t = \ln\left(\frac{L}{L_0}\right) \Rightarrow \frac{\Delta L + L_0}{L_0} = \exp\left(\dot{\varepsilon}_0 t\right)$$

$$\Delta L(t) = L_0\left(\exp\left(\dot{\varepsilon}_0 t\right) - 1\right) \tag{5.2}$$

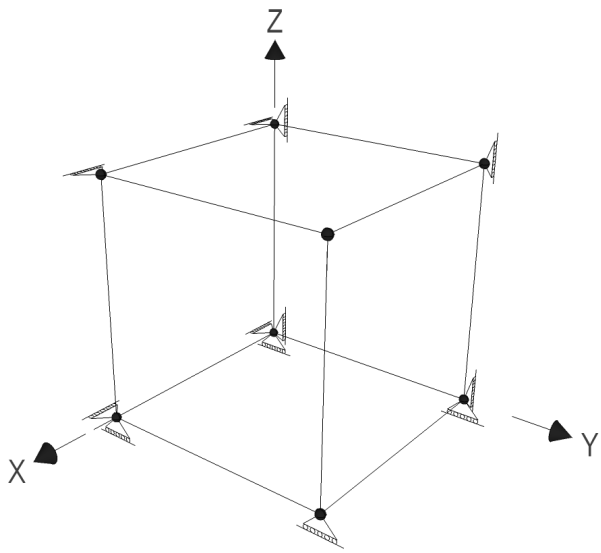

Figure 5.1: *Boundary conditions for the 8-node solid brick element in a global axis-system*

The boundary conditions shown in figure 5.1 are given such that each node placed in one of the basis planes(xy-, yz-, zx-plane) are constrained to translate out of their plane and free to translate in their plane. This will cause stresses in one direction only. Readily the triaxiality according to equation 5.1 then becomes

$$\sigma_{eq} = \sigma_{zz} \vee \sigma_H = \frac{1}{3}\sigma_{zz} \Rightarrow \sigma^* = \frac{1}{3}$$

The analytical void volume fraction is calculated as shown in the pseudo code above and is compared to the results obtained in the simulation with the UMAT in LS-DYNA. Since the triaxiality is constant throughout the simulation, there should not be any deviation between the analytical calculation performed with constant- and varying triaxiality. This is used to verify the modification in the Matlab script.

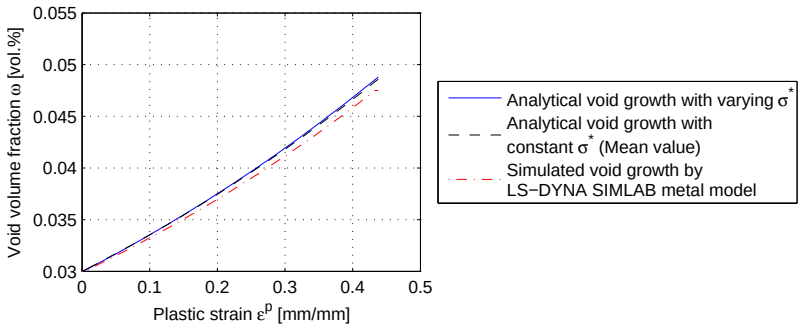

Figure 5.2: *8-node element comparing analytical and simulated growth in void volume fraction*

Figure 5.2 shows a quite good agreement between the analytical calculations and the simulation. The different analytical approaches are identical which implies that the modification is valid. However, we observe a slight negative offset between the simulated- and the analytical void volume fraction. A possible reason for the small negative offset is the assumption of constant plastic strain rate. LS-DYNA decompose the strain tensor in an elastic- and plastic strain tensor as mentioned in section 3.1.1. When assuming constant strain rate, this only ensure that the sum of the elastic- and plastic strain rate tensor is constant. The magnitude of the plastic strain rate will therefore be somewhat smaller; consequently this causes a negative offset.

5.1.3 Void Growth in Tensile Test

The verification is further done by comparing the simulated- with the analytical void volume fraction in the tensile tests. To obtain quasi-static loading the velocity imposed on the specimens is gradually increased to avoid dynamic influences. Thus the assumption of a constant strain rate is only valid to some extent. Figure 5.3 shows the analytical- and simulated void volume fraction for the model with coarse brick elements(SC-model). The analytical approach is performed with both varying and constant triaxiality.

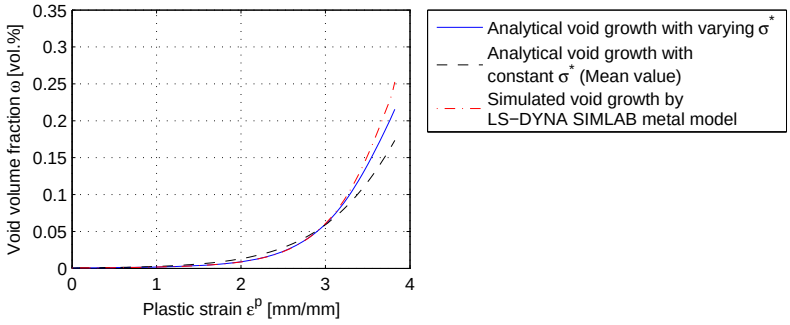

(a) σ-phase ~ 0

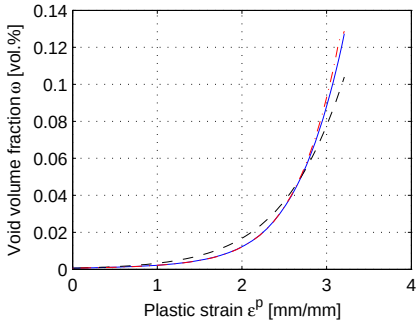

(b) σ-phase $1 - 5$

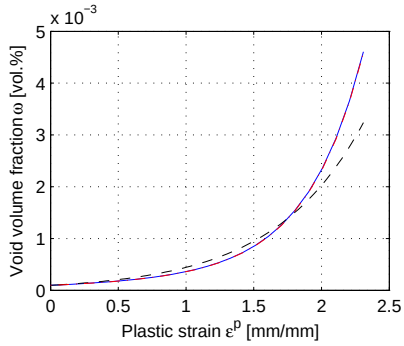

(c) σ-phase ~ 10

Figure 5.3: *Verification of the analytical and simulated void volume fraction for the SC model*

The results presented in figure 5.3 show excellent agreement between the analytical calculations with varying triaxiality and the simulated. Only small deviations are observed in figure 5.3(a) and can be explained by the coalescence of voids that accelerates the void growth, and becomes relatively

large at such void volume fractions. The same procedure is performed for the plane solid model with coarse mesh (AC model), and is plotted in figure 5.4.

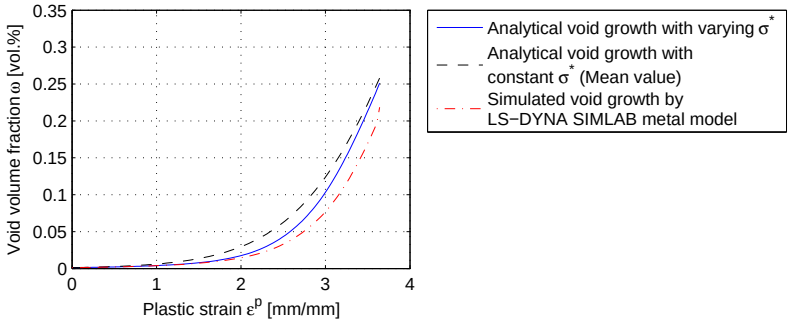

(a) σ-phase ~ 0

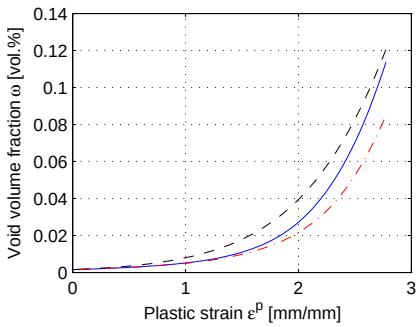

(b) σ-phase $1 - 5$

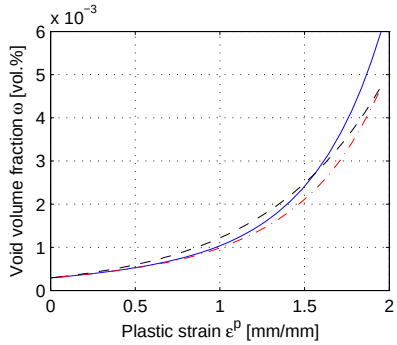

(c) σ-phase ~ 10

Figure 5.4: *Verification of the analytical and simulated results of the AC model*

These simulations are in good agreement at first, but deviates when the plastic straining becomes large. The reason for this underestimation seems to be quite complex. A possible explanation for some of the deviations is the coarse mesh. The void volume growth is driven by the volumetric plastic strains according to equation 3.26. Since the plane solid elements represent a rotational volume, the volumetric strains are consequently more sensitive to the large deformations occurring after necking. The SC elements represents only a fraction of the volume in the AC element, thus it becomes

less sensitive to such large deformations. To substantiate the assumption of mesh sensitivity for plane solid elements, the same calculations have been performed on the verification specimen mentioned in section 4.2.2. The specimen is modeled with a substantially finer- and optimized mesh net to capture the necking in a correct way. The result is plotted in figure 5.5.

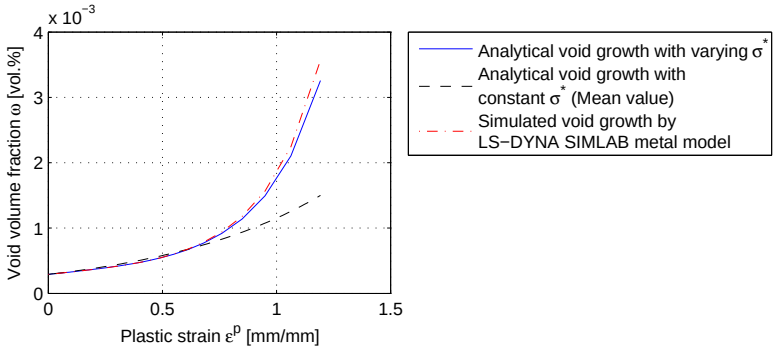

Figure 5.5: *Verification of the analytical and simulated void growth results of the properly refined verification model*

The verification model is simulated with same the parameters as the specimen containing ∼10 vol.%. σ-phase. The figure shows a good agreement between the simulated and analytical approach. The small deviations in the simulations can be explained in the way as for the SC model, i.e. the coalescence of voids. The AF model has a mesh density between the AC model and the verification model, and has been calculated with results presented in appendix C.2.1. This refined mesh shows some improvement, but it has some deviations for ∼0 vol.% σ-phase. Based on these analyses, it seems like the Gurson model is very mesh-sensitive.

5.2 Necking

To verify the optimized material values, we compare the calculated necking from the lab-results with the analytical necking developed from the constitutive relations.

5.2.1 Derivation of Analytical Necking

In uniaxial tension, we have $\sigma_{eq} = \sigma_1$, where σ_1 is the principle stress in the longitudinal direction. Until necking we assume that the macroscopic and microscopic stresses are close to equal i.e. $\sigma_{eq} \approx \sigma_M$. Under these assumptions necking should according to equation 5.3 occur when

$$\frac{d\sigma_M}{d\varepsilon_M} = \sigma_M \tag{5.3}$$

Thus, combining equation 3.20 and 3.22 one can readily obtain the differential in equation 5.3

$$\frac{d\sigma_M}{d\varepsilon_M} = \sum_{i=1}^{n} \theta_i e^{-C_i \varepsilon_M} \tag{5.4}$$

This implies that no explicit expression of the strain, at the onset of necking, can be developed unless some assumptions are made. For large values of θ_i, R_i will quickly converges towards Q_i as it approach the necking strain shown in the figure. For this reason we introduce a modified yield stress

$$\begin{aligned} \sigma_0^* &= \sigma_0 + \sum_{j=1}^{m} R_j \\ R_j &= Q_j \left(1 - e^{-C_j \varepsilon_{eq}^p}\right) \end{aligned} \tag{5.5}$$

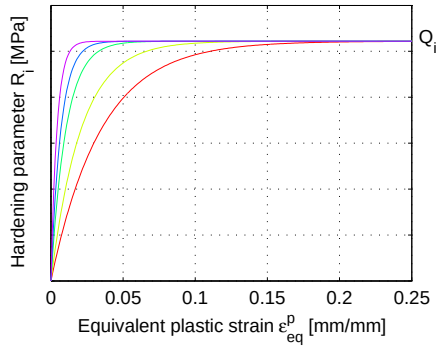

In this figure, evolution of hardening parameter R_i at increasing plastic straining for different values of θ_i

where m is the number of "constant" terms; i.e m corresponds to the number of θ_j parameters with large values.

For most problems with Voce hardening, according to equation 3.21, the problem will be reduced, such that only one set of parameters, corresponding to the set with the lowest value of $\theta = \theta_m$, is sufficient for the calculations. Thus, an explicit solution of the strain at necking, ε_u, can be derived using equation 5.4, 3.20 and 5.5

$$\begin{aligned} \theta_m e^{-C_m \varepsilon_u} &\approx \sigma_0^* + Q_m \left(1 - e^{-C_m \varepsilon_u^p}\right) \\ e^{C_m \varepsilon_u} &\approx \frac{\theta_m + Q_m}{\sigma_0^* + Q_m} \end{aligned}$$

The expression for the necking strain then yields

$$\varepsilon_u \approx C_m^{-1} \ln \left(\frac{C_m + 1}{\sigma_0^* / Q_m + 1} \right) \tag{5.6}$$

5.2.2 Derivation of Numerical Calculation of Necking

The lab-results from the tensile tests are interpreted by calculating the necking strain. To simplify the calculation of the necking, we use the expression for the engineering stress given in equation 2.5. When the stress is related to the initial configuration of the area, the necking is readily described as the point where the force in the specimen reaches its maximum. Using equation 5.3 the necking is now written as

$$\frac{d\sigma_t}{d\varepsilon_l} = \sigma_t$$

Where the true stress can be expressed through the engineering stress

$$\sigma_t = \frac{F}{A} = \frac{F}{A_0}\frac{A_0}{A} = \sigma_e \exp(\varepsilon_l)$$

On incremental form the stress and strain becomes

$$d\sigma_t = d\sigma_e \exp(\varepsilon_l) + \sigma_e \exp(\varepsilon_l)\, d\varepsilon_l$$
$$d\varepsilon_l = d\varepsilon_e \exp(-\varepsilon_l)$$

Inserting in the necking criterion we get

$$\frac{d\sigma_e \exp(\varepsilon_l) + \sigma_e \exp(\varepsilon_l)\, d\varepsilon_l}{d\varepsilon_l} = \sigma_e \exp(\varepsilon_l))$$
$$\frac{d\sigma_e \exp(\varepsilon_l)}{d\varepsilon_l} = 0 \Rightarrow \frac{d\sigma_e}{d\varepsilon_e} = 0 \text{ for } \varepsilon_l > 0$$

The criterion can be rewritten to a numerical scheme

$$\frac{\sigma_e^{i+1} - \sigma_e^i}{\varepsilon_e^{i+1} - \varepsilon_e^i} = 0$$

Consequently, the necking occurs when

$$\sigma_e^{i+1} \leq \sigma_e^i \text{ for } d\varepsilon_e \neq 0 \tag{5.7}$$

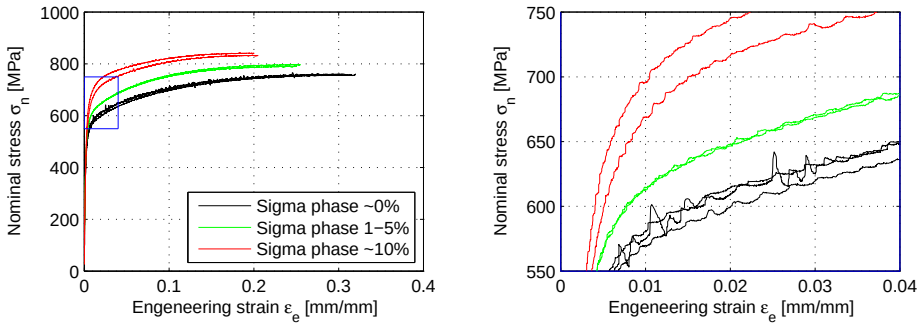

(a) Overview of lab data

(b) Close up for oscilating data

Figure 5.6: *Noise in extracted lab data from engineering strain - nominal stress used in calculation for necking*

Figure 5.6(b) shows that there is some noise the laboratory data. To capture the correct necking strain, moving averages are used to smooth the curve. The moving averages are given as

$$\sigma^i_{e,mov}(N) = \frac{\sigma_e^{i-N} + \sigma_e^{i+1-N} + \cdots + \sigma_e^{i} + \cdots + \sigma_e^{i-1+N} + \sigma_e^{i+N}}{2N+1} \tag{5.8}$$

where N is the length of the moving average. The moving average is unfortunately numerically unstable. Meaning, N must be long enough to smooth irregularities, but still short enough to avoid an underestimation of the necking. To handle this problem a small algorithm running a number of moving average lengths N is implemented when calculation the necking strain. The necking criterion then becomes

$$\sigma^i_{mean} = \frac{1}{N_{max} - N_{min} + 1} \sum_{j=N_{min}}^{N_{max}} \sigma^i_{e,mov}(N_j) \tag{5.9}$$

by inserting this in equation 5.10 we get

$$\sigma^{i+1}_{mean} \leq \sigma^i_{mean} \text{ for } d\varepsilon_e \neq 0 \tag{5.10}$$

The amount of data obtained from the lab-results is quite large. Consequently the calculation of necking by this method tends to be tedious. In the next

section, a study of the deviation between the analytical necking and the numerical calculation scheme presented.

5.2.3 Results Necking

Table 5.1 shows calculated logarithmic necking strain from the lab-results by equation 5.10 and the necking strain from the optimized material parameters calculated by equation 5.6. The lab results in yellow represent the necking strain corresponding to the lab-data used as target curves in the optimization process performed by LS-OPT.

Table 5.1: *A comparison between calculated necking from lab-data, and calculated analytical necking from optimized material parameters*

	σ-phase	~ 0 vol.%			$1-5$ vol.%		$\sim 10\%$	
	Test id	#1	#2	#3	#1	#2	#1	#2
	Lab	0.260	0.269	0.269	0.219	0.224	0.179	0.185
ε_u	AC	0.262			0.216		0.167	
	SC	0.214			0.171		0.123	
	AF	0.248			0.192		0.168	

The general trend for the analytical results is a premature necking for increasing content of σ-phase. The material parameters for the AC model are in good agreement with the lab data. The solid plane element (AF) model with refined mesh has some deviations, and has a negative offset for all values. The SC model has a substantial deviation, which increases for higher levels of σ-phase.

To explain the cause of the deviations, the assumptions behind the development of the analytical necking strain are investigated. For the analytical necking to be valid, the macroscopic stress, σ_{eq}, must be equal to the microscopic matrix stress, σ_M.

Figure 5.7 shows how the simulated equivalent stress, σ_{eq}, vary with the simulated matrix stress, σ_M. In addition the simulated void volume fraction, ω, is plotted to see how it varies with the equivalent plastic strain, ε^p_{eq}.

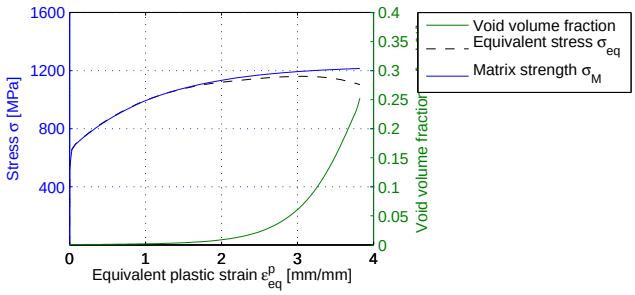

(a) σ-phase ~ 0

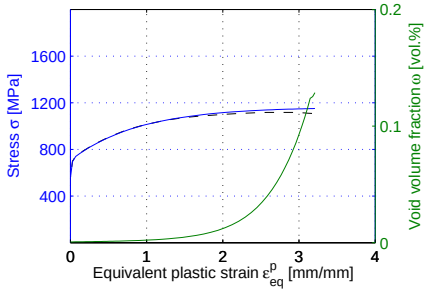

(b) σ-phase $1 - 5$

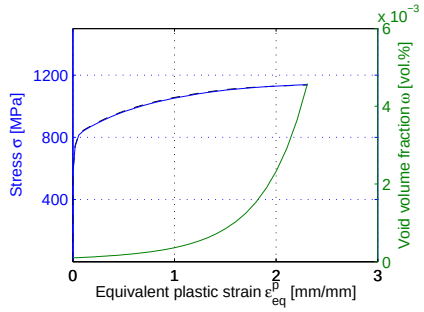

(c) σ-phase ~ 10

Figure 5.7: *A comparison of the microscopic stress, σ_M, and the macroscopic stress, σ_{eq}, with the corresponding void volume fraction ω for the SC model*

As seen in the figure above the deviation between the macroscopic and microscopic stresses does not occur until the specimens experience large plastic strains, and even at large plastic strains the deviations are small. The other simulations show same tendency and the results is given in appendix C.2.2. These results are omitted since they show reasonably good agreement with the lab results.

In table 5.2 the relation between the different stresses at necking are quantified.

Table 5.2: *Relation between macroscopic equivalent stress, σ_{eq}, and microscopic matrix stress, σ_M, at necking*

$\sigma-$phase	~ 0 vol.%			$1-5$ vol.%		$\sim 10\%$	
Test id	#1	#2	#3	#1	#2	#1	#2
σ_{eq}/σ_M	1.002	1.002	1.002	1.001	1.001	1.003	1.003
(AC) σ_{eq}/σ_M		1.002			1.001		1.003
(SC) σ_{eq}/σ_M		1.003			1.004		1.005
(AF) σ_{eq}/σ_M		1.005			1.004		1.003

The table above clearly shows that the assumption of equal stresses at necking is valid. However, the table gives some questionable results, that is $\sigma_{eq} > \sigma_H$. For the equivalent stress to be larger than the macroscopic stress, the void volume fraction according to equation 3.9 must be

$$\omega > \frac{2}{\beta_1} \cosh\left(\frac{3\beta_2\sigma_H}{2\sigma_M}\right) \tag{5.11}$$

For uniaxial tension and assuming that $\sigma_{eq} = \sigma_M$, the expression becomes

$$\omega > \frac{2}{\beta_1} \cosh\left(\frac{\beta_2}{2}\right) \tag{5.12}$$

The proposed fitting parameters implies that $\omega \approx 1.5$. Intuitively, a void volume fraction in this order of magnitude is interpreted as a non-physical behavior, thus it seems to be a small numerical error in the UMAT.

5.3 Discussion of Results

In this chapter it is obtained independent procedures to calculate the void volume fraction, analytical necking and numerical necking. The results vary a lot, even though some results are in good agreement with the expected results, it is generally too many deviations to verify the results completely. The optimization of the Gurson material model is not simple, and requires extensive knowledge of the nature of its behavior.

An interesting observation is that the SC model seems to be more accurate in the end but deviates somewhat in the beginning of the simulations. On the other hand, the AC model behave in an opposite manner by estimating the behavior until necking very well, but loses its accuracy in the end of the simulations. It has been implied that a part of the explanation probably is caused by the large rotational volume in the plane solid elements and its lack of ability to describe post necking behavior. However, another possible contribution to the deviations can be the optimization process in LS-OPT. The optimized material parameters should be in the same range, but we see huge difference between the AC parameters and the SC parameters. This could explain some of the strange behaviors occurring in some of the tests.

For further simulations of the pipe-fittings, the optimized results are applied. However, the results are interpreted with great caution knowing that there are several deviations from the behavior experienced in the laboratory results.

6. Numerical Analysis of Component Test

In this chapter the discretization of the dynamic impact test and the numerical model with its properties will be explained. The numerical results will be analysed and discussed with respect to the laboratory results. The main goal for this thesis is to capture the ductile-brittle fracture seen in the laboratory test. Therefore, the dynamic impact test $D1_{\sigma\sim0}$, $D2_{\sigma=1-5}$ and $D3_{\sigma\sim10}$ are simulated for comparison with the laboratory test results. The force-displacement curves are compared and the fracture propagation are examined from the numerical model. The calculations are done by numerical simulations with the optimized material parameters obtained in the previous chapters. A challenge from the previous thesis Austnes and Bjørklid (2010) has been the transition between the ductile- and brittle fracture observed in the laboratory program. By expanding the Gurson material model with an additional brittle fracture criterion, it is believed to describe the ductile-brittle fracture.

In figure 6.1 the test fixture is shown and its dimensions in 6.2, with the hemispheric nose as the dynamic impact actuator. The pipes fittings are 3" pipes, the straight pipe is 500 mm long, and the radius of the 90° elbow is 114.2 mm. From the welded seam between the pipes and the clamped fixture measures 188 mm.

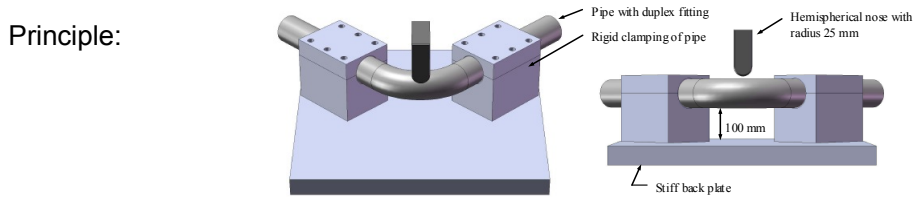

Figure 6.1: *Principle of fixture used in experimental program, Børvik et al. (2012)*

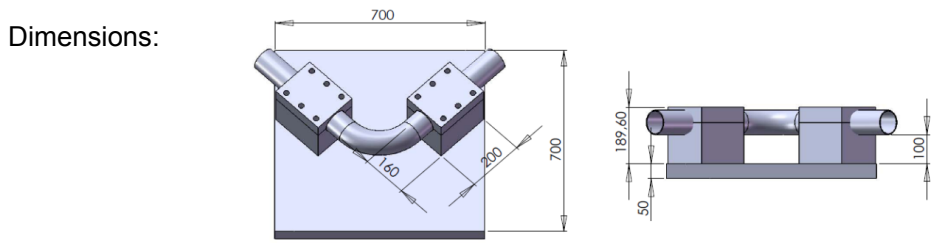

Figure 6.2: *Dimensions of fixture used in experimental program, Børvik et al. (2012)*

As previously mentioned in section 2.4, both quasi-static and dynamic impact test on 3" steel pipe fittings were performed, with and without σ-phase. In this section it will be focused on three dynamic impact tests with id: $D1_{\sigma\sim0}$, $D2_{\sigma=1-5}$ and $D3_{\sigma\sim10}$ where the volume fraction of sigma phase is $\sim$ 0 %, 2-5 % and $\sim$ 8 % (counted to 9.6), respectively.

The straight pipes welded to the elbow do not contain σ-phase, and are therefore modeled with the material parameters for $\sim$0 σ-phase. The investigated part, that is the elbow, will be simulated with the material parameters corresponding to its level of σ-phase.

The dynamic impact test energy is equivalent to tools and such dropped at a height of 15-20 m. Were the trolley including the nose weight 378 kg and velocities between 5-10 m/s. In figure 6.3(b) the numerical model is shown with the elbow in red and nose in green.

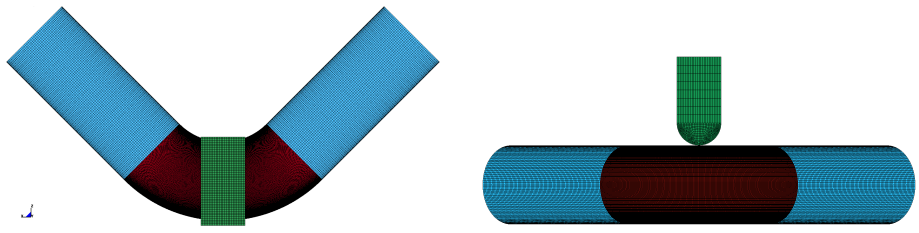

(a) x-z plane (b) y-z plane

Figure 6.3: *Numerical test set-up, model reflected along x-y plane*

6.1 Discretization

Knowing that the fracture criterion follows the mesh dimensions, the pipe thickness is used to decide the element dimensions. In the preliminary discussions it was proposed that 7 nodes over the thickness should be sufficient to describe the deformation and still give a reasonable calculation time. This implies that the element dimensions have to be approximately $0.5 \cdot 0.5 \cdot 0.5$mm for solid brick elements. Figure 6.4 shows the discretization.

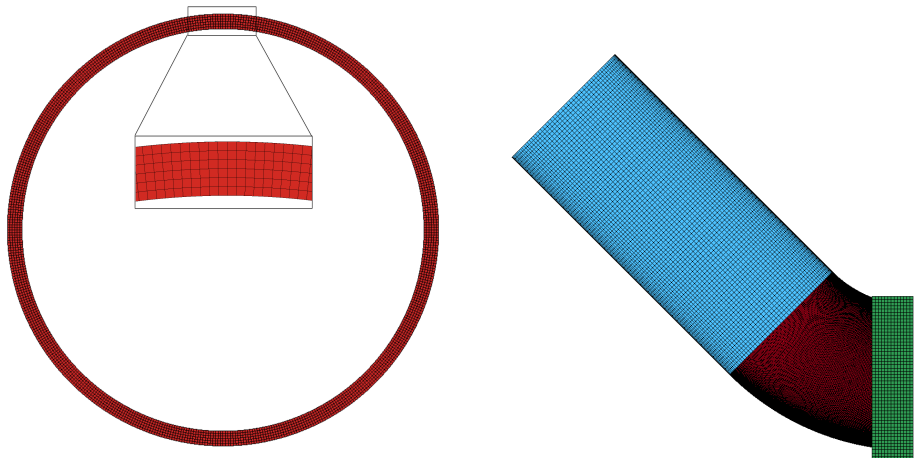

(a) Cross section of elbow (b) Analytical model

Figure 6.4: *Discretization of mesh as used in simulations*

This will in turn require 6 elements over the thickness as shown in figure 6.4(a), 520 elements the circumferential direction and consequently 360 elements along the elbow. A somewhat coarser mesh is given for the straight pipe, with 3 elements over the thickness, 120 elements in the circumferential direction and 90 elements along the pipe. This should be sufficient to describe the local buckling expected at the clamped support. Due to a rather time-consuming calculation process, the specimens are modeled with symmetric boundary conditions. At the support, the pipe is clamped, this is considered valid since there was not measured any movements at the support during the laboratory tests.

There are three contact formulations in the analysis; tied-, surface- and self-contact. The tied contact is between nodes in the elbow and straight pipe. Surface contact between the nose and elbow, and self-contact for the elbow. The tied contact is imposed to insure connectivity between the pipes. There are other methods to obtain connectivity, but in general they are more cumbersome.

6.2 Dynamic Impact

Modeling a dynamic impact, it is important to have control over the energies in the system. As said, the trolley weighs 378 kg, and at velocities between 5-10 m/s, this corresponds with energies between 4.73 kJ - 18.9 kJ. The energies in the simulation is halved, due to modeling with symmetry. In the analysis, the nominal velocity is set to 10 m/s, and for test series $D3_{\sigma\sim10}$ it is set to measured velocity from laboratory test, i.e. 9.96 m/s. That corresponds to initial kinetic energies of 9.45 kJ, 9.45 kJ and 9.37 kJ for $D1_{\sigma\sim0}$, $D2_{\sigma=1-5}$ and D3, respectively.

6.2.1 Results

To validate the explicit dynamic analysis, an energy balance check has been performed to see if artificial energy occurs during simulations, this is plotted in figure 6.5.

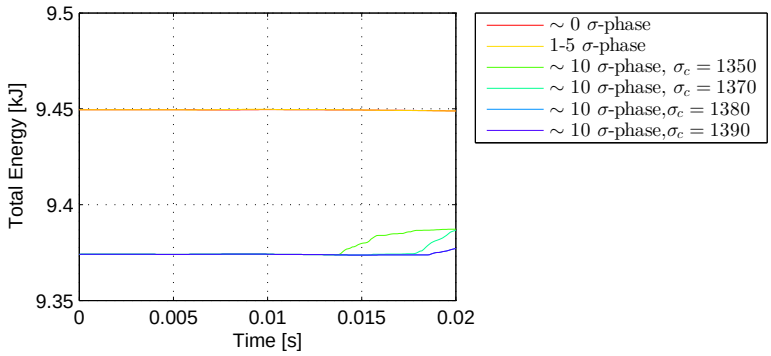

Figure 6.5: *Energy balance check for the dynamic explicit analysis*

It is recommended that the total energy should not vary with more than $\approx 1\%$. For test series $D1_{\sigma\sim0}$ and $D2_{\sigma1-5}$ the total energy remains constant throughout the simulation, while the test series containing $\sim$10 σ-phase, the maximum variation is approximately 1.4 ‰. This small variation comes from hourglass energy, however it is within the recommended range and therefore neglectable. Here you can see the difference the initial velocity has on the energy development trough-out the simulations. The sudden change at the end of $\sim$10 σ-phase is due to rapidly eroding of elements, and eventually global failure.

$\mathbf{D1_{\sigma\sim0}}$ and $\mathbf{D2_{\sigma=1-5}}$

The initial velocity for test series $D1_{\sigma\sim0}$ and $D2_{\sigma1-5}$ are 10 m/s. In laboratory there are not observed any cracks or fractures, only large plastic deformations. In figure 6.6, the force-displacement relations is plotted. In the simulations, the displacements represent the vertical (z-direction) translation of the nose, and the force is the force between the nose and pipe.

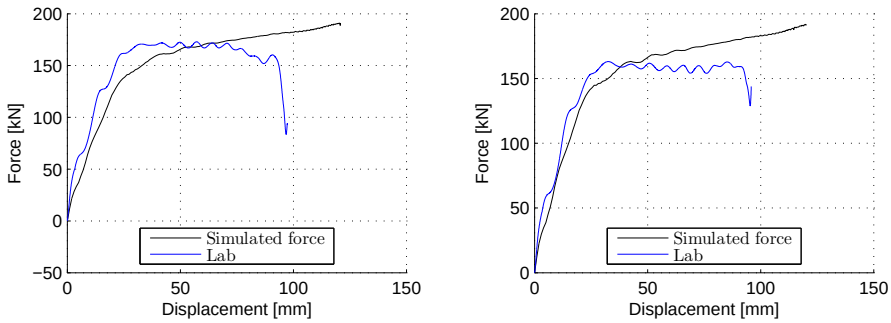

(a) $\sim$0 σ-phase (b) 1-5 σ-phase

Figure 6.6: *Dynamic impact test with inital velocity of 10 m/s on test series $D1_{\sigma\sim0}$ and $D2_{\sigma=1-5}$*

The translation of the nose was stopped after 100 mm, giving the specimens an elastic spring-back after impact in the laboratory. This causes a drop in the force levels at the end of the curve. The simulations are terminated after 20 ms, explaining the absence of drops in force levels at the end of the simulations. These observations are shown in figure 6.6.

For both analysis the elastic stiffness is a little lower compared to laboratory results. The same is seen in when the simulations yields, at a lower force

level. As mention in the report Børvik et al. (2012) and thesis Austnes and Bjørklid (2010), the deviation in wall thickness of the pipes varies greatly for all the specimens and within specimens. The wall thickness of the pipes used in test $D1_{\sigma\sim0}$ was measured and the average thickness was 3.4 mm. The allowed deviation in reduced wall thickness for these kinds of pipe fittings is 12.5 %, defined by Statoil. They have not defined an upper limit. An upper limit tolerance is given for straight pipes only in ASTM as 22.5 % (ASTM, 2008). The wall thickness in the straight pipes can then vary between 2.68 - 3.72 mm. This variation could explain the deviation between the simulations and laboratory response curve.

However, it is clear that the hardening parameters are incorrect. For both analyses the force level increases too much throughout the analysis, whereas the lab results have a distinctive plateau after yielding. This deviation could be traced back to the optimization of the material in the tensile test. LS-OPT's miscalculations of the hardening parameters could be traced back to the non-physically large plastic deformations of the elements in the coarse mesh.

As seen in table 6.1, the total energy is substantially higher in the lab data compared to the simulations. An interesting observation is the level of absorption is almost identically for the different levels of σ-phase.

Table 6.1: *Total energy absorbed by pipe fittings*

	Energy absortion [kJ]	
	$\sim$0 σ-phase	1-5 σ-phase
Lab	32.879	32.125
$D1_{\sigma\sim0}$	37.014	-
$D2_{\sigma1-5}$	-	37.059

$\mathbf{D3}_{\sigma\sim10}$

Impact test $D3_{\sigma\sim10}$, counted to 9.6 vol. % after testing, has been given the $\sigma \sim 10$ material parameters calibrated previously, henceforth $D3_{\sigma\sim10}$. The process of calibrating the critical stress used in the brittle fracture criterion was inaccurate. Thus, a case study with the range given in the same section is therefore performed. The range of critical stress, σ_c, is set to be between 1350 MPa and 1400 MPa.

The goal of the case study is to try and obtain the effect of a brittle fracture. It is believed to be successful with introducing a critical stress. There are 6 simulations with critical stress levels, set evenly spaced between 1350 MPa and 1400 MPa.

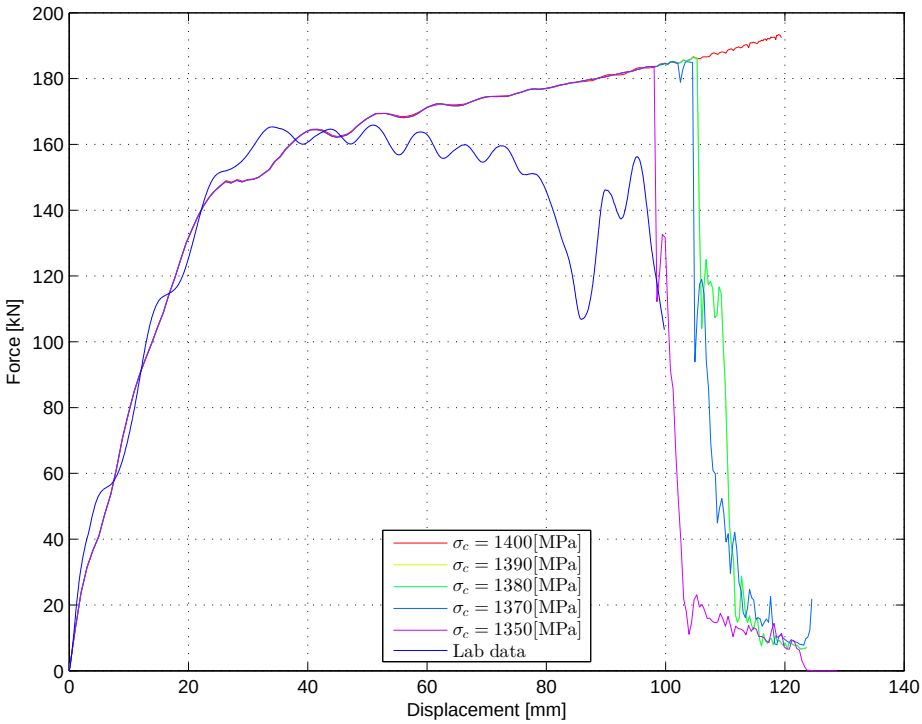

Figure 6.7: *Study of influence from varying brittle fracture criterion σ_c for $\sim$ 10 σ-phase*

In the figure above, 6.7, all the simulations are shown with the laboratory results. Except σ_c=1360, this simulation experienced non-physical deformation involving internal element nodes crossing, returning ”negative” volume

and therefore an error termination of the simulation.

All the simulations behaves in the manner until fracture. The elastic stiffness of the simulations are in good agreement with lab results. However, the dynamic oscillations observed in the lab-results are not capture in the simulations. The material yields at approximately the correct force level, and we se some dynamic oscillations as observed in the laboratory. As the material goes further in to the plastic domain, the same trend as in $D1_{\sigma\sim0}$ and $D2_{\sigma1-5}$ is observed. The materials hardens to much, and when the laboratory test specimen observes the fracture initiation, the simulated specimens continuous the material hardening. This is reflected in table 6.1, where the total energy absorbed in the pipe fittings is calculated.

Table 6.2: *Total energy absorbed by pipe fittings for different critical fracture stresses*

		$D3_{\sigma\sim10}$				
	Lab	1350	1370	1380	1390	1400
Π [kJ]	28.885	30.573	32.906	33.312	33.312	37.129

As mentioned previously, the nose was physically stopped after a deformation of 100 mm. In the simulations, the termination of the analysis was only controlled by a time parameter, i.e. the nose was free to move as long as simulations were ongoing. Thus, the calculated absorbed energy is somewhat overestimated, due to the simulated displacement greater than 100 mm. Nevertheless, the main reason for the greater energy absorption is the overestimated hardening and lack of ductile fracture.

The different fracture stresses initiate fracture, but they are all initiated too late. The most strict fracture criterion ($\sigma_c = 1350$MPa) initiates fracture at a deformation of about 95 mm, which is within the range of the nose. However, the force level is far of the experienced levels in the laboratory. As the fracture stress increases, the force and displacement level are consequently increased, until the fracture stress reaches 1400 MPa. This fracture criterion does not initiate fracture. In figure 6.8 the fracture propagation for fracture criterion $\sigma_c = 1390$MPa is shown and compared to the lab result.

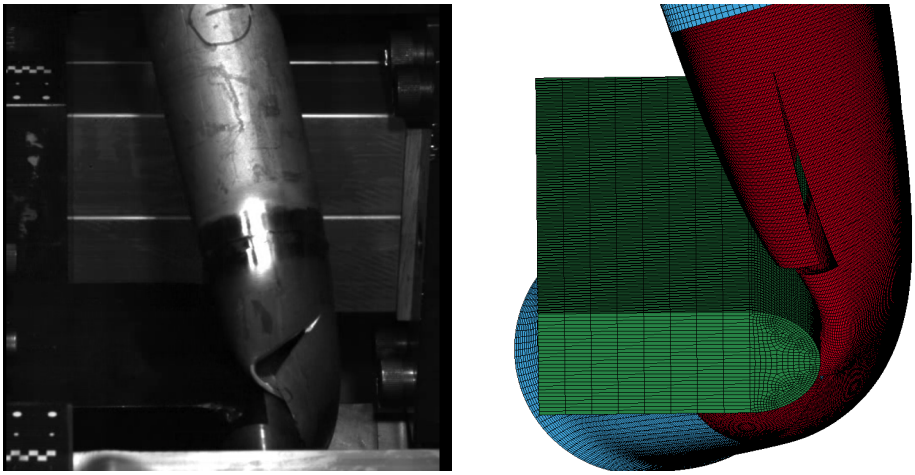

(a) Laboratory at $\sim$ 16 ms (b) Simulation at 15.5 ms

Figure 6.8: *Brittle crack propagation*

As seen in figure 6.8(b), the simulation initiates brittle fracture prematurely. Further in the simulations, the fracture propagates rapidly in to the transition zone where the elbow is welded to the straight pipe. The straight pipe is modeled with material parameters corresponding to $D1_{\sigma\sim0}$. This material has not been modeled with the brittle fracture criterion the. Consequently, the fracture is not allowed to go any further when reaching the straight pipe. Thus, it propagates along the weld until the elbow is completely separated from the straight pipe. When the fracture propagation initiates, it seems that the material is unable stop further propagation. With only an increase of 10 MPa the fracture is not existent, and the behavior of the pipe is similar to $D1_{\sigma\sim0}$ and $D2_{\sigma1-5}$. This indicates that the fracture criterion is extremely sensitive, and very hard to control. In figure 6.9 we see the major difference in response due to the minor decrease in critical fracture stress.

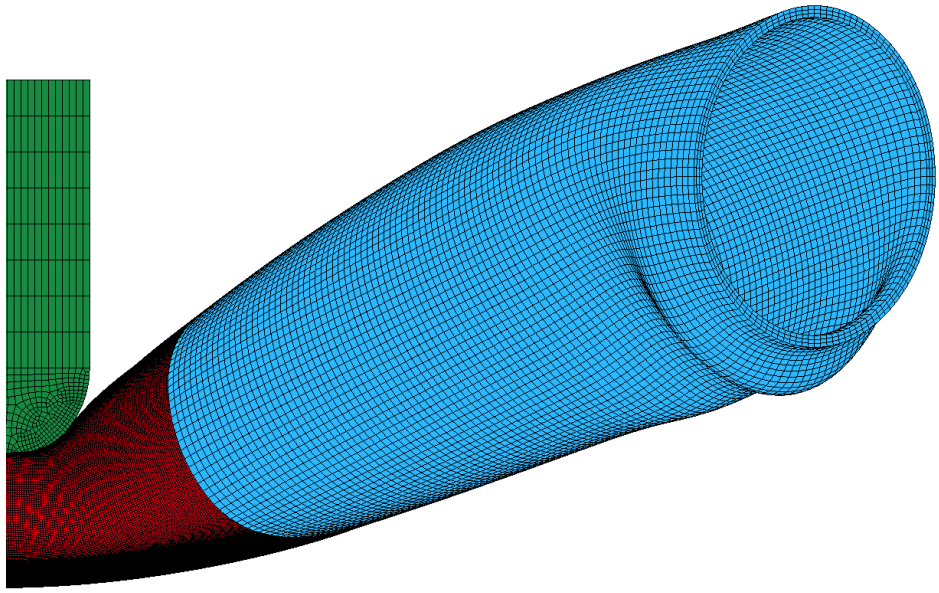

(a) σ_c=1400MPa

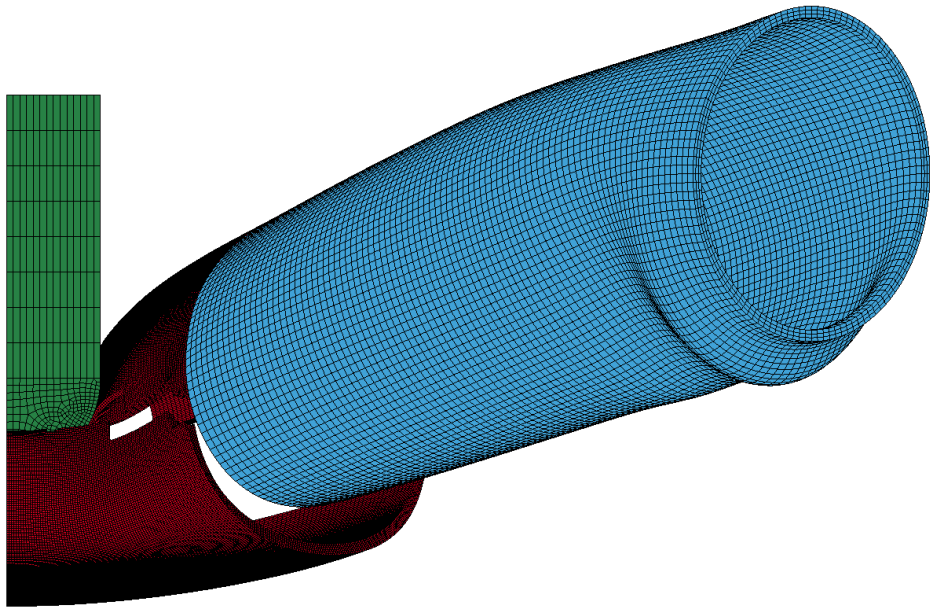

(b) σ_c=1390MPa

Figure 6.9: *Comparing brittle fracture criterion values at end of simulation*

6.2.2 Discussion of Results

In this chapter we have simulated the dynamic response of offshore pipe fittings subjected to impact loading. The results are discussed and trends are commented. Since several problems during the calibration process occurred, the results from these calculations were expected to deviate somewhat from the laboratory results. Initially, it was intended to focus on the pipe fittings with σ-phase levels of ~ 8, with the different velocities. However, since the material optimization was unable describe the behavior for the previous problems, it was therefore concluded that causes of error was more likely to be detected in the simpler problems.

The first observation is the small deviation in the initial elastic stiffness. Investigating the pipes from the laboratory, there is a deviation in the nominal thickness. A possible solution to obtain this effect is to distribute the thickness in a probabilistic manner. When the simulations enter the plastic domain the hardening parameter is overestimated. This trend is already observed in the CTOD test in section 4.3, and was therefore expected. This is most likely caused by the optimization scheme producing incorrect parameters due to the coarse mesh.

The ductile fracture is not observed in any of the simulations. Since the tensile tests overestimate the critical void volume fraction, the component test never reach these levels of void volume fraction. Thus, the ductile fracture seen in the laboratory will be impossible to obtain with the given material parameters. With the correct ductile fracture criterion, local ductile fracture will occur, and further cause an increase in the stress in the area surrounding the crack. Calibrating the fracture stress for these local stress levels could give a higher fracture stress, which hopefully would lead to more controllable fracture propagation.

7. Concluding Remarks

In this thesis a numerical approach to simulate the behavior of duplex stainless steel with precipitated σ-phase has been performed. The simulations have been done using the Gurson material model, which is implemented in the user defined material model in the SIMLab Metal Model. In addition the material model has been combined with a brittle fracture criterion also available in the SIMLab Metal Model. The hypothesis and the results obtained from these simulations will be summarized and concluded here.

In the thesis it is experienced that the Gurson material model is very complex, and requires extensive knowledge. The influence of the Gurson model becomes applicable in materials with more ductile fractures. For problems such as pipe fittings with precipitated σ-phase, it has proven to be redundant to apply this model.

TENSILE TESTS

Using the tensile tests, the Gurson material model is inverse modeled by LS-OPT for the optimization scheme. Further the ductile fracture criterion ω_{cr} has been calculated. The results are somewhat ambiguous, meaning that the optimized material parameters are not directly transferable between plane solid- and brick elements. LS-OPT is a terrific tool, but requires good insight and should be used with caution. When used incorrectly, multiple solutions can occur and sensitive variables should be either individually calibrated or obtained with another method. For convergence of the material model, a sufficiently fine mesh is necessary for the given problem. A combination of these challenges, makes it very difficult to distinguish the origin of the errors experienced.

- LS-OPT is sensitive to input parameters, consequently this can provoke multiple outcomes
- The initial void volume fraction should be determined separately from the other material parameters
- The Gurson model is very mesh sensitive, and correct material parameters are impossible to determine with a coarse mesh

CTOD FRACTURE TOUGHNESS TESTS

The simulations of these tests were performed to verify the results obtained in the tensile tests. Further, it was meant to calibrate the brittle fracture criterion. The expected results were not achieved and it was therefore performed a case study investigate the source of errors. The main source of error was the effective height in the specimens, giving a too stiff behavior. The spark eroded notch with fatigue cracks proved to weaken the material, in a non-systematically manner. Thus it was not found a success criterion to determine the effect of the fatigue loading on the stiffness. The mesh dimensions were coarse causing too large plastic strains. Consequently, the voids reached their critical value prematurely, i.e. initiated the eroding of elements.

- The test has not been able to verify the results obtained in the tensile tests
- SENB specimens with a spark eroded notch and fatigue cracks proved to be hard to simulate, due to the fatigue cracks' unknown effects to the bending stiffness.
- The brittle fracture criterion has not been calibrated in a satisfying manner, only an approximate range for the fracture stress has been taken from these tests

ANALYTICAL VERIFICATION

Independent analytical procedures have been developed to verify the results simulated in the user defined material model (UMAT). The calculation of the analytical void volume fracture has been compared to a simple 8-node element and the tensile tested specimens. The results have partially been verified by this procedure, but the reasons for the deviations are very complex. A possible source of error is the rotational volume in the plane solid elements being sensitive to volumetric plastic straining. Results from the necking calculations verify some of the results, but have large deviation from the brick element models. However, the results are interpreted with great caution knowing that there are several deviations from the behavior experienced in the laboratory results.

- Analytical approaches have shown that the Gurson model is very complex, and interpreting results is difficult
- The calculations verify some results, but in general the deviations occur frequently. Thus the results obtained must be handled with

caution

NUMERICAL ANALYSIS OF THE COMPONENT TESTS

The full scale pipe fittings have been simulated with the optimized material parameters obtained in the previous chapters. A small deviation in the elastic stiffness is observed for some test specimens, this most likely caused by the varying thickness in the real pipe fittings. The hardening parameters seem to be incorrect. This causes an incorrect response in the plastic domain with overestimation of forces and absorbed energy. Ductile fracture is completely absent in the simulations. It seems that the tensile tests overestimates the critical void volume fraction ω_{cr}. Thus, the simulations have not been able to describe the transition between the ductile and brittle behavior seen in the laboratory. When brittle fracture initiates, the propagation of the fracture is difficult to terminate, consequently it continuous until global failure.

- Varying pipe thickness causes deviations in initial stiffness
- Incorrect hardening parameters overestimates the force levels, consequently the pipe fitting absorbs too much energy
- Ductile fracture is not observed during the simulations, possible caused by incorrect critical void volume fraction
- Brittle fracture is obtained, but propagates non controllable manner
- The initiation of brittle fracture is very sensitive, only small decrease in fracture stress causes major differences in the response

8. Further Work

Several aspect has been covered in this thesis and previous work by Austnes and Bjørklid (2010). However, the aim to assemble a numerical model that could describe the ductile-brittle transition and fracture propagation has not yet been achieved. Several interesting problems have occurred, and some of them are proposed for further investigation. It will also be given some guidelines for further research on this topic.

- A study of the initial void volume is important to establish reliable material parameters. It is recommended to look at the work performed by Avramovic-Cingara et al. (2009)
- Further verification of the Gurson Material Model is needed due to unstable sub-routine
- The effect of mesh sensitivity in the Gurson model should be further investigated with respect to the optimization of the material parameters
- A convergence study of the relation between the mesh convergence and the material parameters when using LS-OPT
- Thorough examination of the critical section (spark eroded notch/-fatigue crack) of the test specimens used in the toughness test and accurate measurements of the specimen
- For calibration and investigation of the brittle fracture criterion, a V-notched specimen is preferred
- A procedure to distribute the thickness in a probabilistic manner should be investigated to be able to describe the varying thickness observed in the pipe fittings
- Calibration and investigation of a Weibull distribution of the brittle fracture criterion
- To describe ductile fracture, it is sufficient to apply modified Johnson-Cook material model with the Cockcroft-Latham fracture criterion

Bibliography

T.L Anderson. *Fracture mechanics: Fundamentals and Applications*. Taylor & Francis, Boca Raton, Fla., 3rd ed. edition, 2005.

ASTM. Astm e562-08 standard test method for determining volume fraction by systematic manual point count, 2008. URL `www.astm.org`.

M. B. Austnes and O. Bjørklid. Impact on duplex stainless steel pipes with and without precipitated sigma phase. Master's thesis, NTNU, 2010.

G Avramovic-Cingara, Ch.A.R Saleh, M.K Jaim, and D.S Wilkinson. Void nucleation and growth in dual-phase steel 600 during uniaxial tensile testing. *The Minerals, Metals & Materials Society and ASM International 2009*, 2009. doi: 10.1007/s11661-009-0030-z.

T. Børvik, H. Lange, M. Langseth, and O. S. Hopperstad. Tensile tests of duplex pipe fittings with deviaton in quality caused by sigma phase precipitation. Technical report, NTNU, SINTEF, Statoil ASA, 2009.

T. Børvik, H. Lange, L.A. Marken, M. Langseth, O.S. Hopperstad, M. Aursand, and G. RÃ¸rvik. Pipe fittings in duplex stainless tel with deviation in quality caused by sigma phgase precipitiation. 2010.

T. Børvik, H. Lange, M. Langseth, and O. S. Hopperstad. The behaviour of duplex stainless steel pipe fittings with and without sigma phace precipitation during structural impact. 2012.

Robert D. Cook, David S. Malkus, Michael E. Plesha, and Robert J. Witt. *Concepts and applications of finite element analysis*. John Wiley & Sons, INC., 2002. ISBN 9780471356059. URL `http://books.google.no/books?id=b8seAQAAIAAJ`.

René de Borst. *Damage, Material Instabilities, and Failure*. John Wiley & Sons, Ltd, 2004. ISBN 9780470091357. doi: 10.1002/0470091355.ecm035. URL `http://dx.doi.org/10.1002/0470091355.ecm035`.

G. Fargas, M. Anglada, and A. Mateo. Effect of the annealing temperature on the mechanical properties, formability and corrosion resistance of hot-rolled duplex stainless steel. *Journal of Materials Processing Technology*, 209(4):1770 – 1782, 2009. ISSN 0924-0136. doi: 10.1016/j.jmatprotec.2008.

04.026. URL `http://www.sciencedirect.com/science/article/pii/S092401360800352X`.

A.L Gurson. Continuum theory of ductile rupture by void nucleation and growth. part i. yield criteria and flow rules for porous ductile media. Technical report, Brown Univ., Providence, R.I. (USA). Div. of Engineering, Sep 01 1975.

A.G. Hanssen, T. Austad, T. Tryland, and M. Langseth. The kicking machine: A device for impact testing of structural components. *International Journal of Crashworthiness*, 36:12–24, 2003.

Daniel H. Herring. Sigma-phase embrittlement. *The International Journal of Thermal Technology*, 02 2012.

O. Hopperstad and T. Børvik. *Lecture notes, TKT 4135 Mechanichs of Materials*. NTNU, 2012.

Odd Sture Hopperstad. Theory manual: Simlab metal model. Draft, 2012.

IMOA. Duplex stainless steel, January 2012. URL `http://imoa.info/moly_uses/moly_grade_stainless_steels/duplex_stainless_steel.php`.

S. Kalstad and T. S. Nord. Fragmentation of metallic materials during impact. Master's thesis, Norwegian University of Science and Technology (NTNU), 2011.

I.M. Kulbotten, L.A. Marken, and M. Aursand. The effects of σ phace precipitation on the impact toughness of 22cr duplex stainless steel. Technical report, TNE MTO MAT, 2009.

Hans Lange and Einar Hassel. Ctod fracture toughness testing of duplex and super duplex stainless steels containing σ-phase. Technical report, SINTEF Materials Technology, 2010.

K.Van Minnebruggen, D. Van Puyvelde, W. De Waele, M Verstraete, S Hertele, and R. Denys. Implmentation of an unloading compliance procedure for measurement of crack growth in pipeline steel. Technical report, Gent University, Laboratory Soete, Belgium, 2011.

A. Needleman and V. Tvergaard. Numerical modeling of the ductile-brittle transition. *International Journal of Fracture*, 101:73–97, 2000.

Christian Dalheim Øien. Validation of a modified gurson model ls-dyna user material sub-routine. Project report, NTNU SIMLab, 2011.

A Pineau. Development of the local approach to fracture over the past 25 years: Theory and applications. *International Journal of Fracture*, 138(1-4):139–166, 2006. URL http://www.springerlink.com/index/10.1007/s10704-006-0035-1.

A. Pineau. Modeling ductile to brittle fracture transition in steels – micromechanical and physical challenges. *International Journal of Fracture*, 150:129–156, 2008. ISSN 0376-9429. URL http://dx.doi.org/10.1007/s10704-008-9232-4. 10.1007/s10704-008-9232-4.

Aase Gavina R. Reyes. *Oblique loading of aluminum crash components*. PhD thesis, NTNU, 12 2002.

Sandvik. Datasheet. Technical report, Sandvik Material Technology, 2012.

Z. Stradomski and D. Dyja. Sigma phase precipitation in duplex phase stainless steel. Technical report, Czestochowa University of Technology, Institute of Materials Engineering, 2005. URL http://www.ysesm.ing.unibo.it/Abstract/57%20Dyja.pdf.

H Tamura, E Sasaki, H Yamada, H Katsuchi, and T Chanpheng. Involvements of stress triaxiality in the brittle fracture during earthquakes in steel bridge bents. Vol 9, NBo 3, 2009. URL http://www.ceric.net/kssc/KSSC_3_2009_9_3_241%28C%29.pdf.

V. Tvergaard. On localization in ductile materials containing spherical voids. *International Journal of Fracture*, 18:237–252, 1982. ISSN 0376-9429. URL http://dx.doi.org/10.1007/BF00015686. 10.1007/BF00015686.

V. Tvergaard and A. Needleman. An analysis of the brittle-ductile transistion in dynamic crack growth. *International Journal of Fracture*, 59:53–67, 1993.

A. Convergence and SRB from LS-OPT

This appendix contains the optimization scheme for the plane element model and the brick element model. All the figures and intervals are output from LS-OPT. The confidence interval i=16 is the last increment from LS-OPT and are the best fit for the given variables. The figures show the variables at iteration i with sub-region boundary (SRB).

- Coarse 2D plane solid element model
  - AC $\sigma \sim 0$ vol.%
  - AC $\sigma = 1 - 5$ vol.%
  - AC $\sigma \sim 10$ vol.%
- Coarse 3D brick solid element model
  - SC $\sigma \sim 0$ vol.%
  - SC $\sigma = 1 - 5$ vol.%
  - SC $\sigma \sim 10$ vol.%

Coarse 2D Plane Solid Element Model

AC $\sigma \sim 0$ vol.%

```
============================================================
        C O N F I D E N C E   I N T E R V A L S

                      ITERATION 16
============================================================
```

95% Confidence intervals for individual optimal parameters

Name	Value	Confidence Interval Lower	Upper
Q1	719.945902	695.282208	744.609595
Q2	103.390054	93.8270511	112.953056
theta1	2196.05367	−inf	+inf
theta2	40196.641	−inf	+inf
sigma_0	489.013394	483.091244	494.935544
omega_0	.001199341	.001029203	.00136948

```
============================================================
```

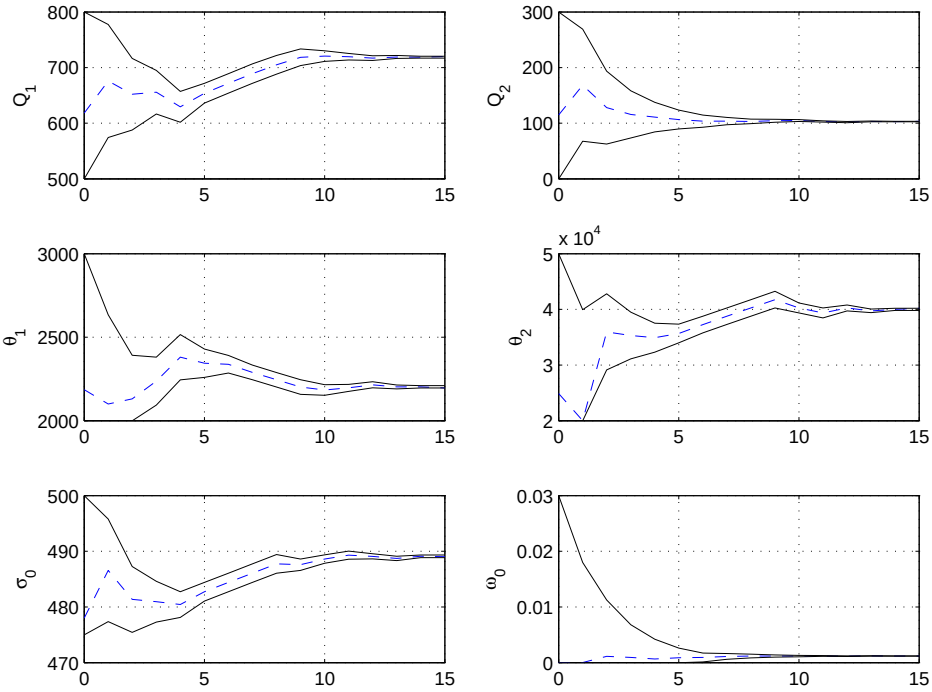

Figure A.1: *Iteration for material parameters, in blue dashed and SRB in black, with* ~ 0 σ*-phase levels*

AC $\sigma = 1 - 5$ vol.%

```
============================================================
         C O N F I D E N C E   I N T E R V A L S

                      ITERATION 16
============================================================
```

95% Confidence intervals for individual optimal parameters

Name	Value	Confidence Interval Lower	Upper
Q1	577.105605	559.163969	595.04724
Q2	105.313476	98.4428109	112.184141
theta1	2473.76341	−inf	+inf
theta2	18675.8114	−inf	+inf
sigma_0	527.16198	521.943551	532.380409
omega_0	.001523122	.001263731	.001782513

```
============================================================
```

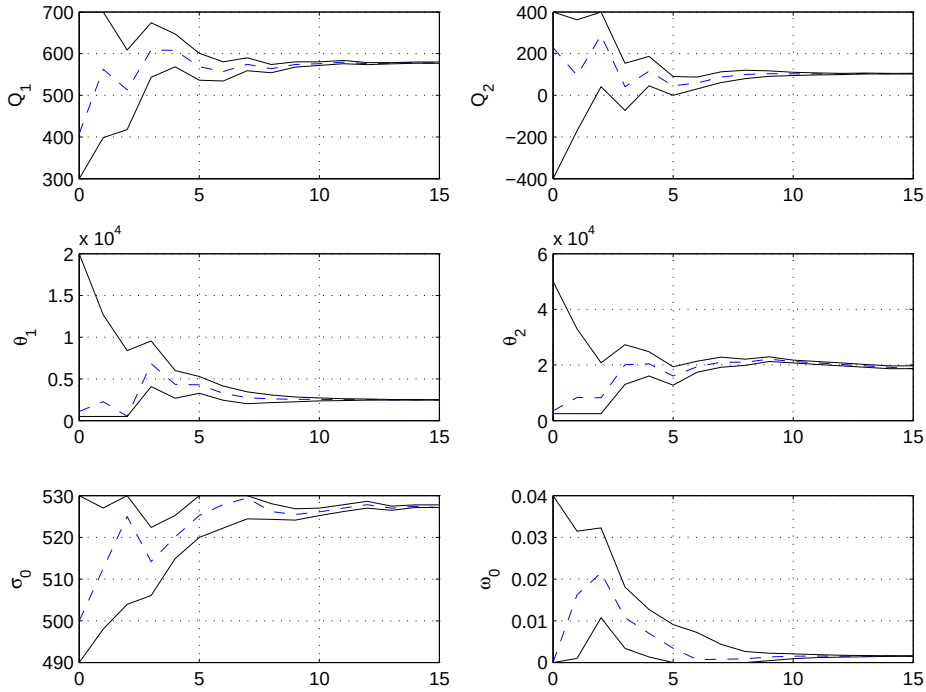

Figure A.2: *Iteration for material parameters, in blue dashed and SRB in black, with* $1-5$ σ*-phase levels*

AC $\sigma \sim 10$ vol.%

```
============================================================
         C O N F I D E N C E   I N T E R V A L S

                      ITERATION 16
============================================================
```

95% Confidence intervals for individual optimal parameters

Name	Value	Confidence Interval Lower	Upper
Q1	453.528048	445.467504	461.588592
Q2	203.751943	193.337042	214.166845
theta1	2328.4124	2219.83371	2436.9911
theta2	48355.7238	−inf	+inf
sigma_0	524.203674	516.545991	531.861358
omega_0	.000291473	8.53216e−5	.000497624

```
============================================================
```

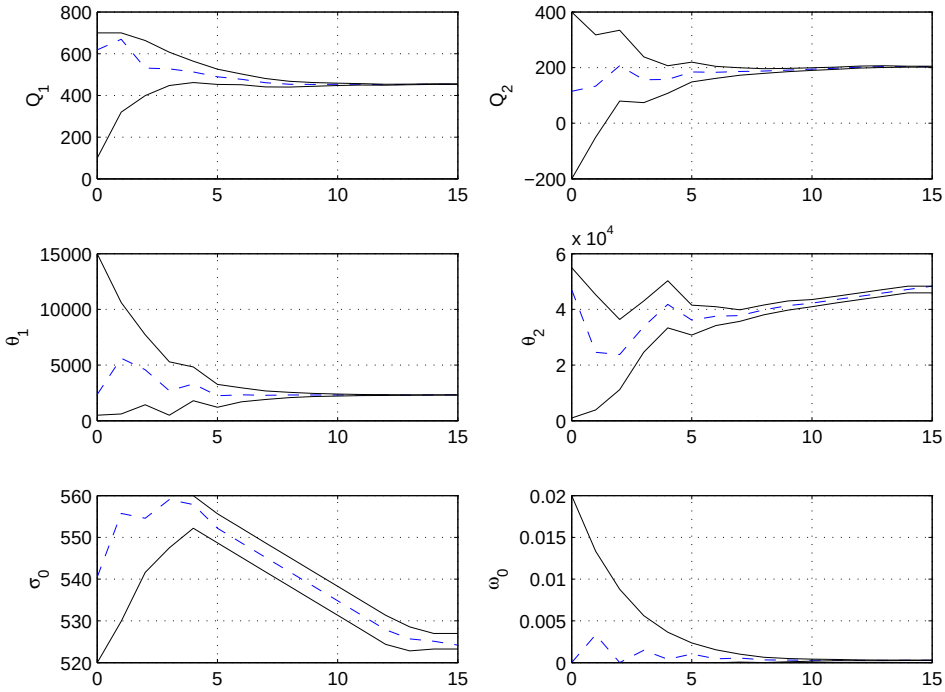

Figure A.3: *Iteration for material parameters, in blue dashed and SRB in black, with* ~ 10 σ*-phase levels*

Coarse 3D cubic solid element model

SC $\sigma \sim 0$ vol.%

```
============================================================
        C O N F I D E N C E   I N T E R V A L S
                      ITERATION 16
============================================================
```

95% Confidence intervals for individual optimal parameters

Name	Value	Confidence Interval	
		Lower	Upper
Q1	582.127274	−inf	+inf
Q2	154.114842	144.495786	163.733897
theta1	2000.12194	−inf	+inf
theta2	49999.9126	−inf	+inf
sigma_0	499.941279	498.831646	501.050913
omega_0	.000543218	.000461312	.000625124

```
============================================================
```

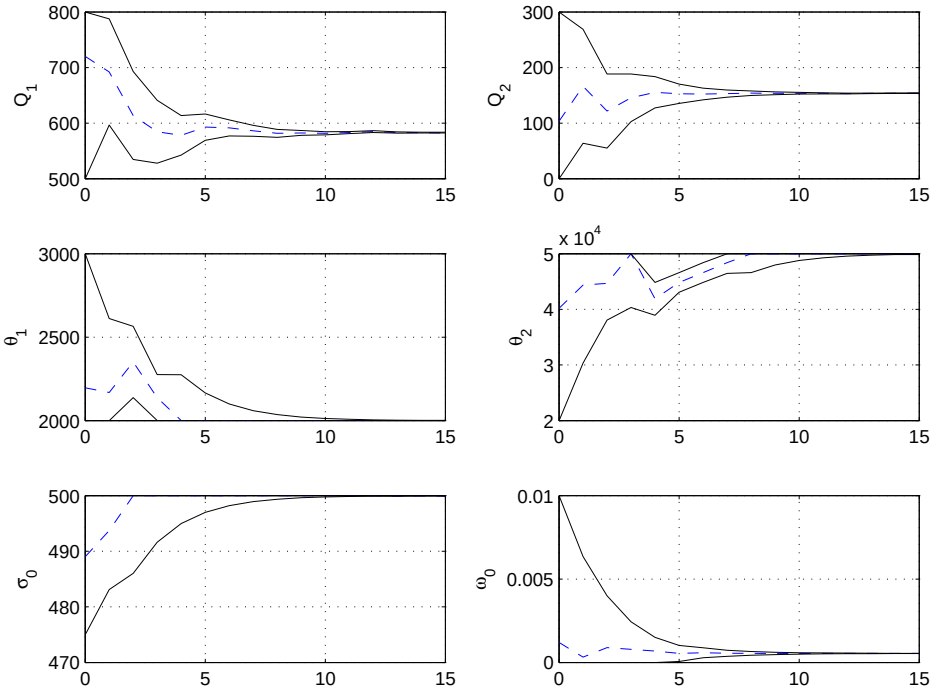

Figure A.4: *Iteration for material parameters, in blue dashed and SRB in black, with* ~ 0 σ*-phase levels*

SC $\sigma = 1 - 5$ vol.%

```
============================================================
        C O N F I D E N C E   I N T E R V A L S

                      ITERATION 16
============================================================
```

95% Confidence intervals for individual optimal parameters

Name	Value	Confidence Interval Lower	Upper
Q1	457.685702	441.170068	474.201336
Q2	170.701565	166.562175	174.840955
theta1	2032.66275	−inf	+inf
theta2	49999.949	−inf	+inf
sigma_0	534.999987	534.5725	535.427474
omega_0	.000627906	.0005411	.000714713

```
============================================================
```

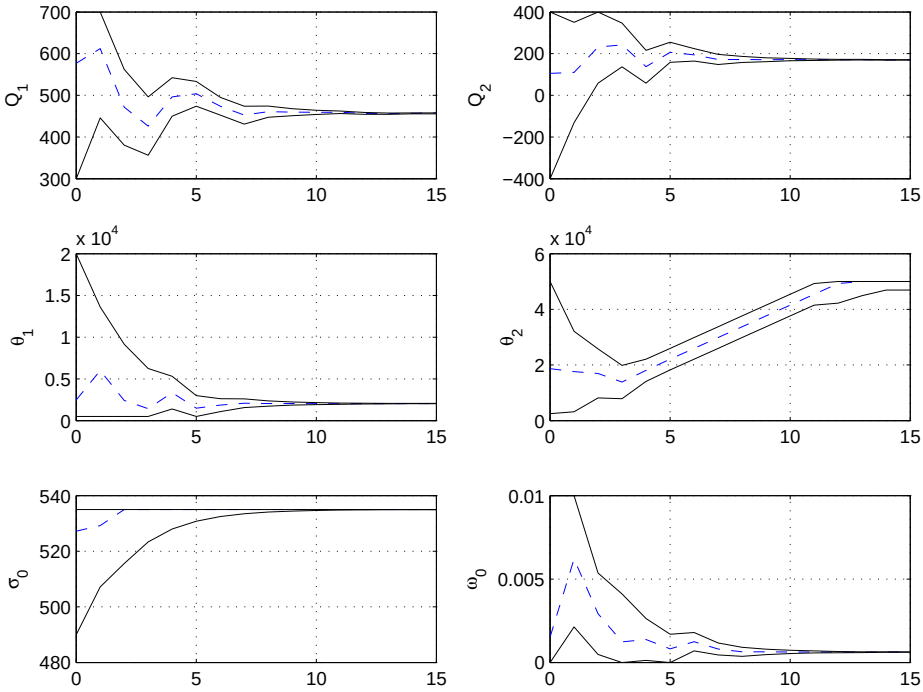

Figure A.5: *Iteration for material parameters, in blue dashed and SRB in black, with* $1-5$ σ*-phase levels*

SC $\sigma \sim 10$ vol.%

```
============================================================
        C O N F I D E N C E   I N T E R V A L S

                      ITERATION 16
============================================================
```

95% Confidence intervals for individual optimal parameters

Name	Value	Confidence Interval Lower	Upper
Q1	359.567005	−inf	+inf
Q2	239.41734	232.51275	246.32193
theta1	1733.33655	−inf	+inf
theta2	5.5e4	−inf	+inf
sigma_0	559.999994	559.003738	560.996249
omega_0	9.66934e−5	4.99271e−5	.00014346

```
============================================================
```

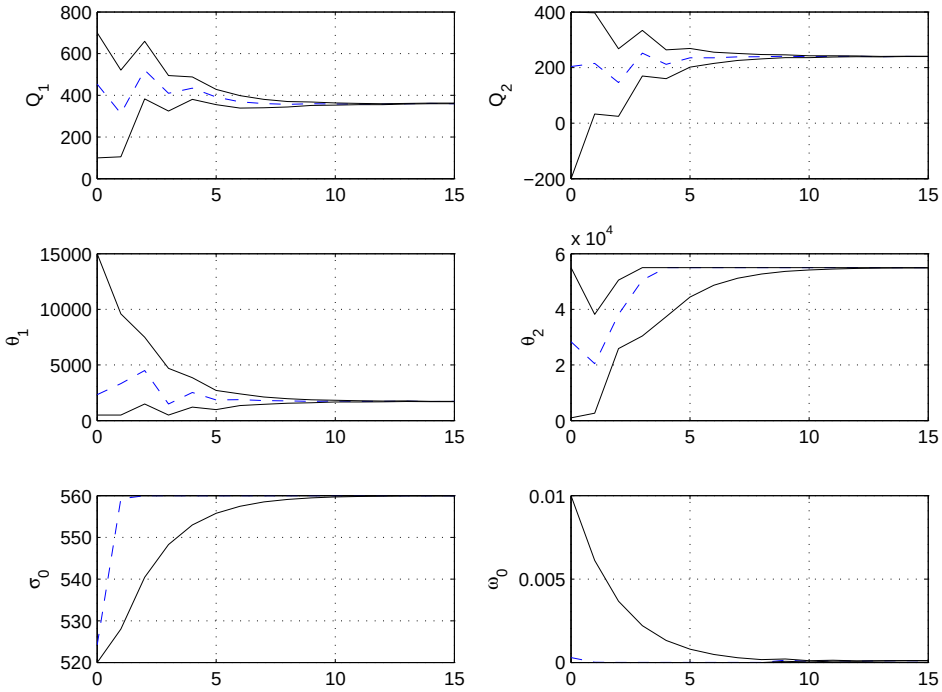

Figure A.6: *Iteration for material parameters, in blue dashed and SRB in black, with* ~ 10 σ*-phase levels*

B. Tensile Test

In this appendix, the simulated strain-stress relation for the tensile tests is shown, for all the mesh models and fractions of $\sigma-$phase content.

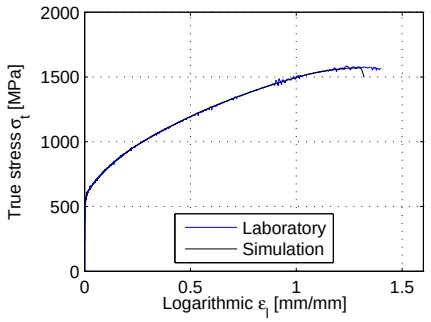

(a) Coarse plane mesh

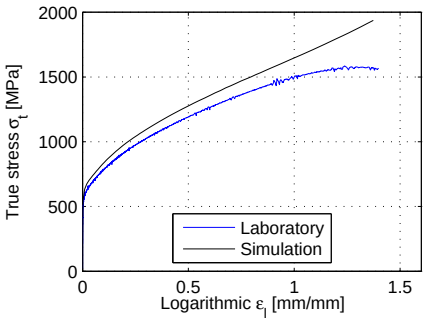

(b) Fine plane mesh

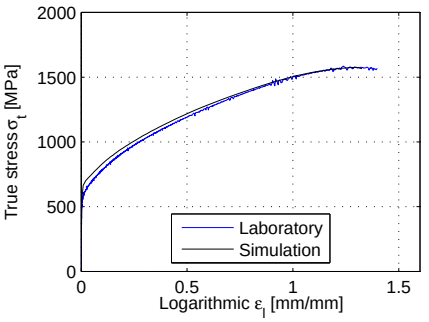

(c) Corse brick mesh

Figure B.1: *Stress-strain relation for optimized material parameters for the different simulations, ∼0 vol% σ-phase*

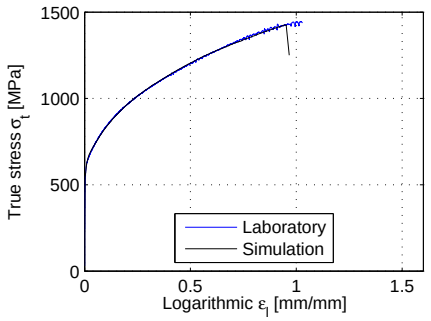

(a) Coarse plane mesh

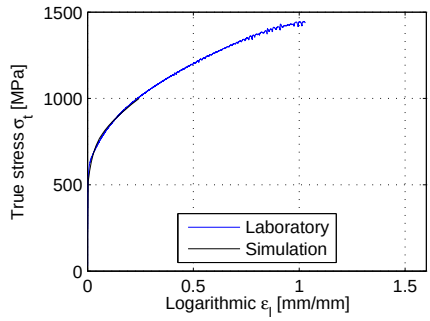

(b) Fine plane mesh

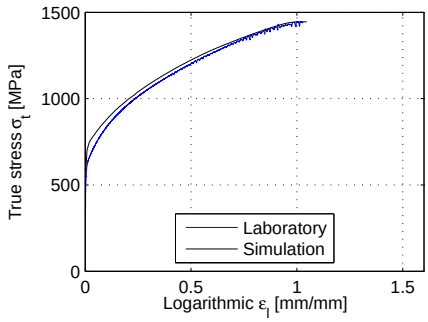

(c) Coarse brick mesh

Figure B.2: *Stress-strain relation for optimized material parameters for the different simulations, 1-5 vol% σ-phase*

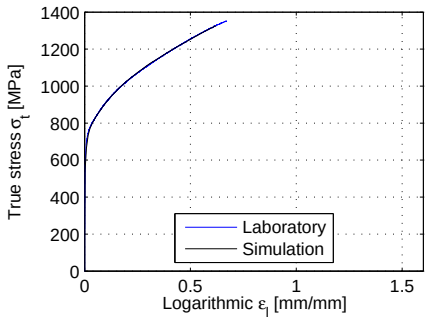

(a) Coarse plane mesh

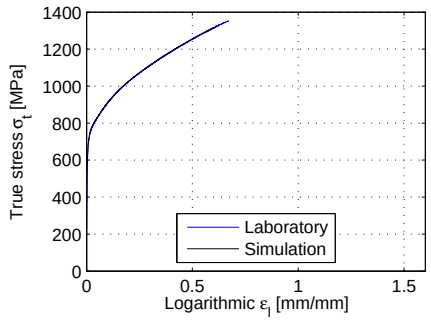

(b) Fine plane mesh

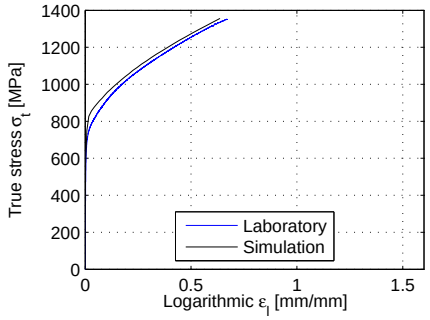

(c) Coarse brick mesh

Figure B.3: *Stress-strain relation for optimized material parameters for the different simulations, ∼10 vol% σ-phase*

C. Analytical Verification

In this appendix the expressions behind the calculations performed in chapter 5 will be discussed. This method is also briefly described in section 5.1.1. The calculations are based on a given strain tensor with a corresponding triaxiality vector. Void volume growth is then calculated for each strain increment through a sub incremental procedure. The appendix is divided into two parts. Part one cover the description of the sub incremental calculations and part two the incremental evolution of the void volume fraction.

C.1 Sub Incremental Growth of Void Volume Fraction

The theory behind the formulas presented here are thoroughly discussed in section 3.1. The incremental equations are presented in the order of appearance in the script.

The first equation applied is the backward Euler scheme to equilibrate the yield function by iterating the equivalent stress. Making the yield function dependent only on σ_{eq} and σ_M, further given a constant triaxiality within the sub increment, the iterative calculation scheme of the equivalent stress becomes

$$
\begin{aligned}
\sigma_{eq,n+1}^{\{0\}} =& \sigma_{M,n+1} \\
f\left(\sigma_{eq,n+1}^{\{i\}}\right) =& \frac{\sigma_{eq,n+1}^{2\{i\}}}{\sigma_{M,n+1}^{2}} + 2\omega_n\beta_1 \cosh\left(\frac{3\beta_2\sigma_{eq,n+1}^{\{i\}}\sigma^*}{2\sigma_{M,n+1}}\right)\cdots \\
& - 1 - (\omega_n\beta_1)^2 \\
\frac{df\left(\sigma_{eq,n+1}^{\{i\}}\right)}{d\sigma_{eq}} =& 2\frac{\sigma_{eq,n+1}^{\{i\}}}{\sigma_{M,n+1}^{2}} + 3\frac{\omega_n\beta_1\beta_2\sigma^*}{\sigma_{M,n+1}} \sinh\left(\frac{3\beta_2\sigma_{eq,n+1}^{\{i\}}\sigma^*}{2\sigma_{M,n+1}}\right) \\
\sigma_{eq,n+1}^{\{i+1\}} =& \sigma_{eq,n+1}^{\{i\}} - \frac{f\left(\sigma_{eq,n+1}^{\{i\}}\right)}{df\left(\sigma_{eq}^{\{i\}}\right)}
\end{aligned}
\tag{C.1}
$$

where i represents the iteration and n the sub increment.

Knowing the equivalent stress, we express the differentiated plastic parameter $d\lambda$ for the sub increment. By using the associated flow rule (eq. 3.6) and invoking power conjugacy (eq. 3.17) for the inner product in equation 3.16 and the scalar quantities we get

$$\sigma_{ij}\dot{\varepsilon}_{ij}^{p} = \sigma_{eq}\dot{\varepsilon}_{eq}^{p}$$

Hence is the plastic parameter can be expressed by σ_M,σ_{eq} and σ^* as

$$
d\lambda_{n+1} = \frac{\sigma_{eq,n+1}d\varepsilon_{eq,n+1}^{p}}{2\frac{\sigma_{eq,n+1}^{2}}{\sigma_{M,n+1}^{2}} + 3\frac{\beta_1\beta_2\omega\sigma_{eq,n+1}\sigma^*}{\sigma_{M,n+1}} \sinh\left(\frac{3\beta_2\sigma_{eq,n+1}\sigma^*}{2\sigma_{M,n+1}}\right)}
\tag{C.2}
$$

The equivalent plastic strain is prescribed from the user, and to calculate the corresponding matrix strain we use eq. 3.20 and obtain

$$\sigma_{eq,n+1}\dot{\varepsilon}_{eq,n+1}^{p} = (1-\omega_n)\sigma_{M,n+1}\dot{\varepsilon}_{M,n+1}^{p}$$

thus the incremental increase of matrix strain becomes

$$
\begin{aligned}
d\varepsilon_{M,n+1}^{p} =& \frac{\sigma_{eq,n+1}d\varepsilon_{eq,n+1}^{p}}{(1-\omega_n)\sigma_{M,n+1}} \\
\varepsilon_{M,n+1}^{p} =& \varepsilon_{M,n}^{p} + d\varepsilon_{M,n+1}^{p}
\end{aligned}
\tag{C.3}
$$

Using the equations above we can calculate the incremental growth in void volume fraction from eq. 3.26 as

$$\begin{aligned} d\omega_{n+1} =& d\lambda_{n+1} 3\beta_1\beta_2 \frac{\sigma_{eq,n+1}\sigma^*}{\sigma_{M,n+1}} \sinh\left(\frac{3\beta_2\sigma_{eq,n+1}\sigma^*}{2\sigma_{M,n+1}}\right) \\ \omega_{n+1} =& \omega_n + d\omega_{n+1} \end{aligned} \tag{C.4}$$

C.1.1 Matlab Script - Sub Incremental Void Volume Growth

```
function [pM,omega] = gursonincrement...
                      (P,T,p0,p_max,mat,matrixstrain)

% Declaring the material parameters
s0=mat(1); Q1=mat(2); C1=mat(3); Q2=mat(4); C2=mat(5);
Q3=0; C3=0;

 % Creating a strain resolution and a corresponding plastic
 % strain vector within the increment
 dp=(p_max-p0)/100;
 p=p0:dp:p_max;

 % Puts the values from last increment as the initial
 % values for this iteration
 pM(1)=matrixstrain;
 omega(1)=P(3);

  for i=1:length(p)
   s_M(i)=s0+Q1*(1-exp(-C1*pM(i)))...
            +Q2*(1-exp(-C2*pM(i)))...
            +Q3*(1-exp(-C3*pM(i)));
   s_eq(i)=s_M(i);

   % Using the Newton-Raphson method to solve the
   % equation Yieldfunction=0 for s_e according to eq. C1
   Yieldfunction=1;
    while abs(Yieldfunction)>10^-6
     Yieldfunction=(s_eq(i)/s_M(i))^2+...
       2*P(1)*omega(i)*cosh(3*P(2)*T/2*s_eq(i)/s_M(i))...
       -1-(omega(i)*P(1))^2;
     dYieldfunction=2*s_eq(i)/s_M(i)^2+...
         P(1)*omega(i)*3*P(2)*T/(s_M(i))...
          *sinh(3*P(2)*T/2*s_eq(i)/s_M(i));
     s_eq(i)=s_eq(i)-Yieldfunction/dYieldfunction;
    end
```

```
    % Calculating the incremental plastic parameter
    % according to eq C2
    dLambda(i)=s_eq(i)*dp/(2*(s_eq(i)/s_M(i))^2+...
        3*omega(i)*P(1)*P(2)*T*s_eq(i)/s_M(i)...
        *sinh(3*P(2)*T/2*s_eq(i)/s_M(i)));

    % Calculate the microcopic strain according to C3
    pM(i+1)=pM(i)+s_eq(i)*dp/((1-omega(i))*s_M(i));

    % calculate void volume fraction according to C4
    omega(i+1)=omega(i)+(1-omega(i))*dLambda(i)...
                *3*omega(i)*P(1)*P(2)/s_M(i)*...
                sinh(3*P(2)*T/2*s_eq(i)/s_M(i));
  end
end
```

C.2 Evolution Void Volume Fraction

The calculation scheme for the sub incremental void volume growth is incorporated in this script which calculate the total void volume fraction vector for the prescribed- straining and stress state.

```
%————————————————————————————————————————————————————————————%
%% Calculation of analytical omega
%  The script calculates the analytical value of the void
%  volume fraction omega. The first calculation is done
%  with varying triaxility and further on compared to a
%  constant triaxility. Last the simulated value from
%  LS—DYNA is plotted for comparisson
%
%  Abbreviations:
%  Void volume fraction = VVF
%
%  Variables:
%  T — Triaxility = Sigma_h/Sigma_eq
%  p — equivalent plastic strain, p_0 — initial ,
%  p_max — end strain
%
%%
% Gurson matrix contains triaxility(:,2) and equivalent
% plastic strain(:,1) from simulation:
gursoninput=importdata('gurson.mat');
%
% Imports material parameters used in the simulations:
omega_0=importdata('results/omega_0.txt');
mat(1)=importdata('results/sigma_0.txt');
mat(2)=importdata('results/Q1.txt');
mat(3)=importdata('results/theta1.txt')/mat(2);
mat(4)=importdata('results/Q2.txt');
mat(5)=importdata('results/theta2.txt')/mat(4);
%
%%
% P = ['fitting parameter beta_1' 'fitting
%       parameter beta_2' 'Initial VVF omega_0']:
n=length(gursoninput(:,1)); P=[1.5 1.0 omega_0];
analyticomega(1)=P(3); matrixstrain=0;

% Loop calculates VVF for each increment of equivialent
% plastic strain, within each increment the triaxility
% remains constant:
%
for i=2:n
    T=gursoninput(i-1,2);
```

```
    p_max=gursoninput(i,1);
    p0=gursoninput(i-1,1);
    P(3)=analyticomega(i-1);
    [pM,Omega]=gursonincrement(P,T,p0,p_max,mat...
                               ,matrixstrain);
    analyticomega(i)=max(Omega);
    matrixstrain=max(pM);
end
%
%%
% For comparison the VVF is calcualted with a constant
% triaxility throughout the plastic strain evolution:
matrixstrain=0; T=mean(gursoninput(:,2));
P=[1.5 1.0 omega_0 0]; p0=min(gursoninput(:,1));
p_max=max(gursoninput(:,1));
[p,Omega]=gursonincrement(P,T,p0,p_max,mat,matrixstrain);
%%
```

C.2.1 Verification of Void Volume Fraction

This section contains a further substantiation of the arguments presented in the analytical verification section. The plots contains analytical void volume fraction with both varying- and constant triaxiality. In addition the simulated void volume fraction from the UMAT in LS-DYNA.

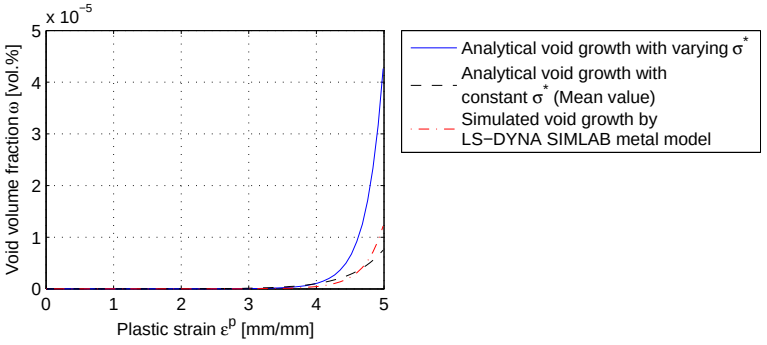

(a) σ-phase ~ 0

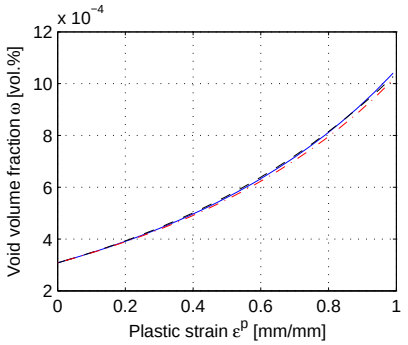

(b) σ-phase $1 - 5$

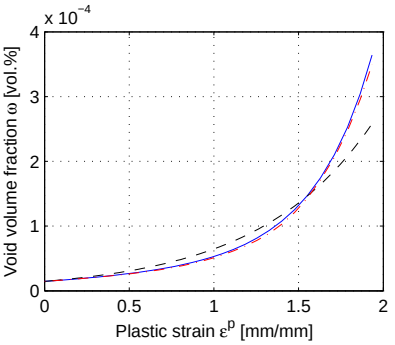

(c) σ-phase ~ 10

Figure C.1: *Verification of the analytical and simulated results in the AF model*

C.2.2 A Comparison of Macroscopic and Microscopic Stresses

This section contains plots of the macroscopic stresses, σ_{eq}, and the microscopic stresses, σ_M with the corresponding void volume fraction, ω, for the different simulations performed in this thesis. It is given to substantiate the comments and assumptions given in section 5.2.

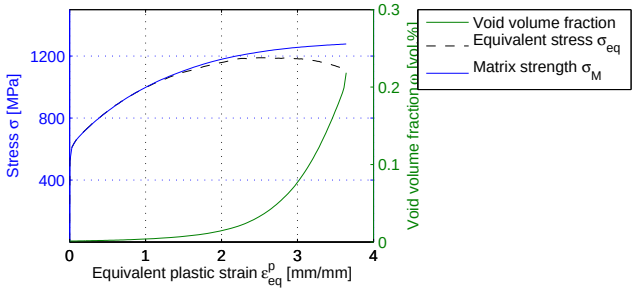

(a) σ-phase ~ 0

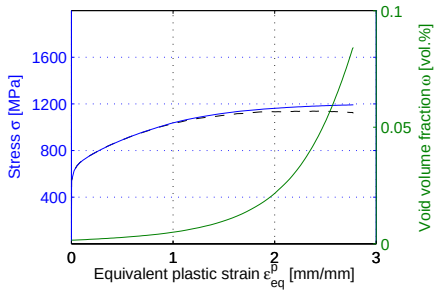

(b) σ-phase $1 - 5$

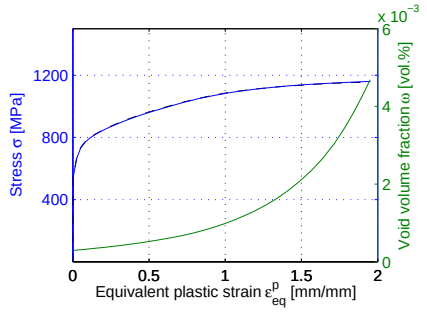

(c) σ-phase ~ 10

Figure C.2: *A comparison of the microscopic stress, σ_M, and the microscopic stress, σ_{eq}, with the corresponding void volume fraction ω for the AC model*

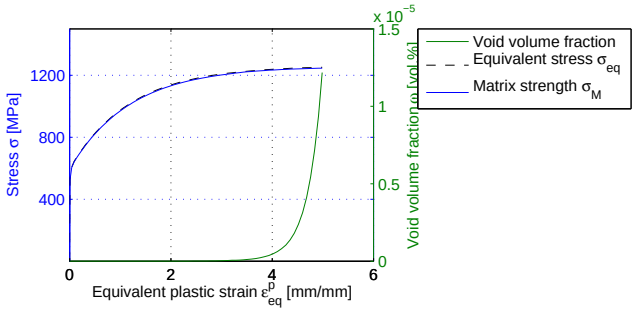

(a) σ-phase ~ 0

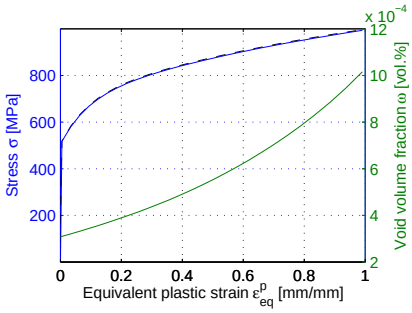

(b) σ-phase $1-5$

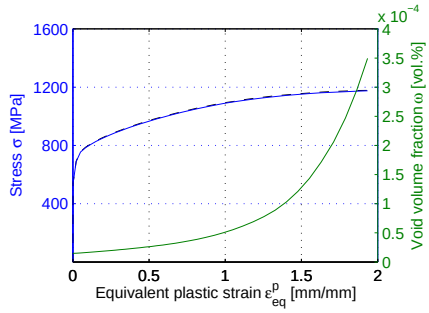

(c) σ-phase ~ 10

Figure C.3: *A comparison of the microscopic stress, σ_M, and the microscopic stress, σ_{eq}, with the corresponding void volume fraction ω for the AF model*

D. CTOD Calculations

In this appendix it is given a brief summary of the preliminary work done prior to the study presented in section 4.3.

All specimens are calculated with the exact geometry from the laboratory.

The results needed to verify the material model used in the simulations are extracted through simple numerical schemes which will be presented shortly. The initial elastic stiffness were first calculated and compared to the ones obtain in the lab test. To calculate it for each of the simulations the following algorithm were applied as

Algorithm 2 Calculation of simulated elastic stiffness

Set counter to i=2
Set $\Delta k = 0$ and $k_{i-1} = \dfrac{f_1}{d_1}$
Set a criterium for the elastic stiffnes variation $\varepsilon \sim 0.1 - 5$
  while $|\Delta k| < \varepsilon$
    $\Delta d = d_i - d_{i-1}$
    $\Delta f = f_i - f_{i-1}$
    $k_i = \dfrac{\Delta f}{\Delta d}$
    $\Delta k = k_i - k_{i-1}$
    $i = i + 1$
  end
$K = \dfrac{f_i}{d_i}$

where f is the contact force between the pendulum and the specimen and d is the CMOD, K is the elastic stiffness for the system.

The maximum force is calculated knowing that the maximum is given by

$$\frac{df}{dd} = 0 \tag{D.1}$$

Using the same the same argumentation as in equation 5.10 we get

$$f_i \leq f_{i-1} \text{ for } dd \neq 0 \tag{D.2}$$

to avoid local maximum a check for all values of f is performed and the largest value is therefore extracted. The corresponding plastic displacements are shown in table D.1

To control the maximum force the analytical plastic force capacity is calculated assuming a fully plastic utilization, and a rectangular cross section at the critical section. The expression then reads

$$F_p = \frac{\sigma_0 (W - a_{notch})^2 B}{L} \tag{D.3}$$

where L is the span between the anvils and the values for W, a_0 and B are given in table 4.10 and σ_0 is the yield force.

Table D.1: *Calculated elastic stiffness from numerical simulations*

$\sigma-$phase	Test id	Sim K	Lab K	Sim Max F	Lab Max F	F_p	Sim v_p	Lab v_p
vol.%	#	$\left[\frac{kN}{mm}\right]$	$\left[\frac{kN}{mm}\right]$	$[kN]$	$[kN]$	$[kN]$	$[mm]$	$[mm]$
0	1-2	449.2	32	31.89	4.48	2.95	1.40	1.95
	1-3	145.8	41	7.01	4.34	3.06	1.38	2.11
1-5	5-1	148.1	46	7.41	4.87	3.41	0.83	1.61
	5-2	661.1	50.5	30.70	5.15	3.05	0.62	1.35
	5-3	Inf	42	28.34	4.26	2.83	0.00	1.34
10	10-1	95.3	31.5	3.81	1.85	1.73	0.70	0.16
	10-2	529.0	32	17.73	1.92	1.70	0.46	0.11
	10-3	467.3	42	16.73	2.29	1.60	0.44	0.09

It is safe to say, that these results are incorrect. The reason for this is to some extent the authors miscalculations in addition to the effective height, which was very hard to predict. The figures in the next pages show the force-displacement curve for the different test specimens with the expected heights.

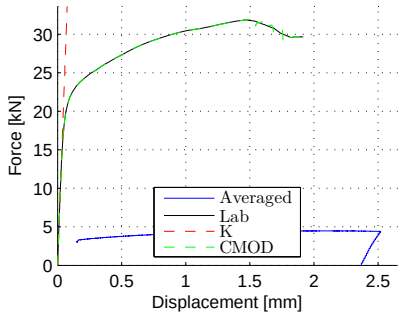

(a) Test id 0-2

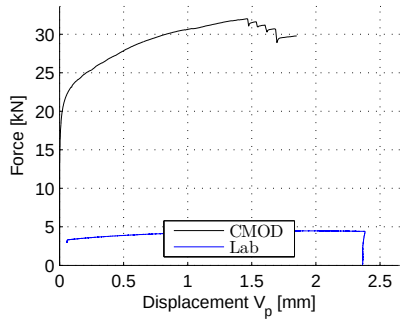

(b) Test id 0-2

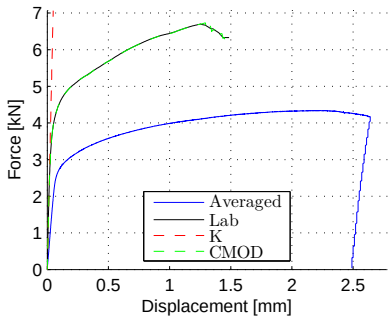

(c) Test id 0-3

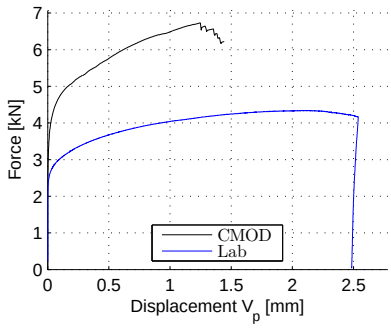

(d) Test id 0-3

Figure D.1: *Results from analytical test, CTOD fracture toughness test,* ~ 0 *vol.%* σ*-phase*

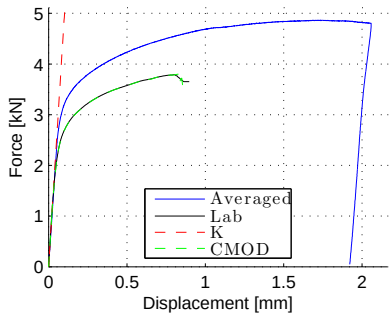

(a) Test id 5-1

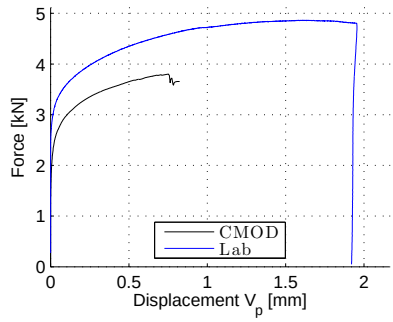

(b) Test id 5-1

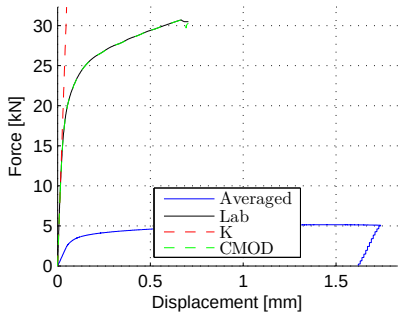

(c) Test id 5-2

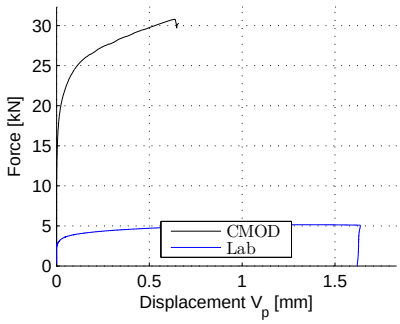

(d) Test id 5-2

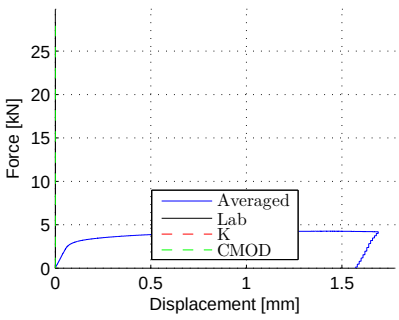

(e) Test id 5-3

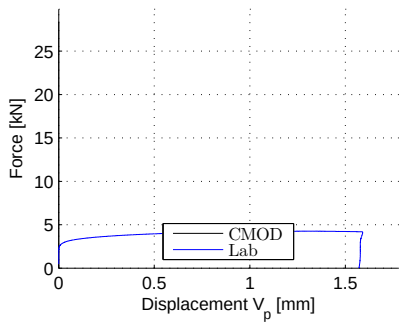

(f) Test id 5-3

Figure D.2: *Results from analytical test, CTOD fracture toughness test, $1-5$ vol.% σ-phase*

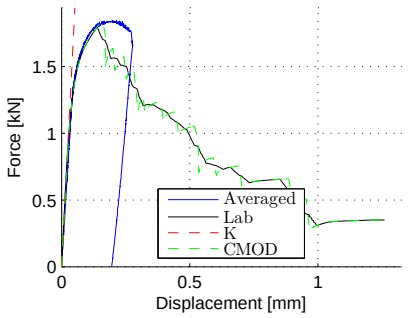

(a) Test id 10-1

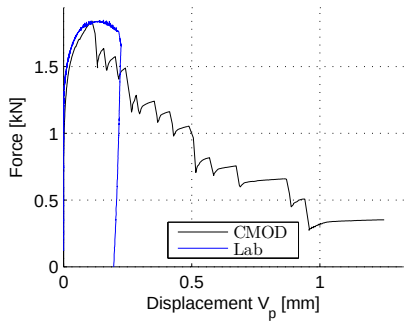

(b) Test id 10-1

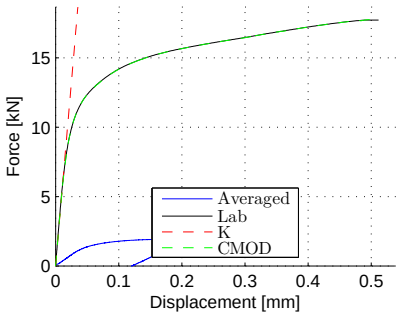

(c) Test id 10-2

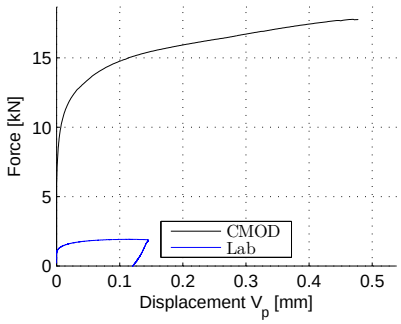

(d) Test id 10-2

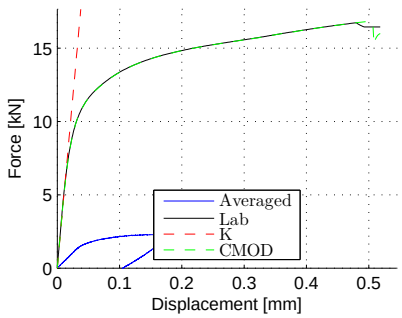

(e) Test id 10-3

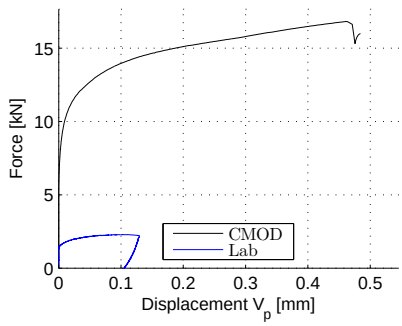

(f) Test id 10-3

Figure D.3: *Results from analytical test, CTOD fracture toughness test,* ~ 10 *vol.%* σ*-phase*

E. Additional Data Files

The structure of the appended cd is listed below. Only the most important files are included, such as .k-files, ASCII-files and results from the simulations. In addition the most important matlab .m-files are included.

The folder structure of the appended data file:

- CTOD
- full-scale
- matlab-scripts
- tensile-tests